Measurement of the Single Top Quark Production Cross Section in 1.96-TeV Proton-Antiproton Collisions

Koji NAKAMURA

February 2009

UTPP-81

Measurement of the Single Top Quark Production Cross Section in 1.96-TeV Proton-Antiproton Collisions

Koji NAKAMURA
(Doctoral Program in Physics)

Submitted to the Graduate School of Pure and Applied Sciences in Partial Fulfillment of the Requirements for the Degree of Doctor of Philosophy in Science

at the

University of Tsukuba

Measurement of the Single Top Quark Production Cross Section in 1.96-TeV Proton-Antiproton Collisions

Koji NAKAMURA

(Doctoral Program in Physics)

Submitted to the Graduate School of

Pure and Applied Sciences

in Partial Fulfillment of the Requirements

for the Degree of Doctor of Philosophy in

Science

at the

University of Tsukuba

Abstract

Top quarks are predominantly produced in pairs via the strong interaction in $\bar{p}p$ collisions at $\sqrt{s} = 1.96$ TeV . The top quark has a weak isospin 1/2, composing a weak isospin doublet with the bottom quark. This characteristic predicts not only top quark pair production via strong interaction but also single production together with a bottom quark via weak interaction. However, finding single top quark production is challenging since it is rarely produced ($\sigma_{\mathrm{singletop}}$=2.9 pb) against background processes with the same final state like W+jets and $t\bar{t}$. A measurement of electroweak single top production probes the W-t-b vertex, which provides a direct determination of the Cabbibo-Kobayashi-Maskawa (CKM) matrix element $|V_{tb}|$. The sample offers a source of almost 100% polarized top quarks. This thesis describes an optimized search for s-channel single top quark production and a measurement of the single top production cross section using 2.7 fb^{-1} of data accumulated with the CDF detector. We are using events with one high-p_T lepton, large missing E_T and two identified b-quark jets where one jet is identified using a secondary vertex tagger, called SecVtx, and the other jet is identified using SecVtx or a jet probability tagger, called JetProb. In this analysis we have developed a kinematics fitter and a likelihood-based separator between signal and background. As a result, we found that the probability (p-value) that the candidate events originate from a background fluctuation in the absence of single top s-channel production is 0.003, which is equivalent to 2.7 σ deviations in Gaussian statistics, and this excess corresponds to the single top s-channel cross section of $2.38^{+1.01}_{-0.84}$ pb. An observed value of $|V_{tb}|$ is $1.43^{+0.38}_{-0.26}(\text{experimental}) \pm 0.11(\text{theory})$. We also set the 95 % CL. upper limit of $\sigma_s = 4.15$ pb for the s-channel production cross section.

Acknowledgments

There are many people who have directly contributed to this dissertation, and many more who contributed indirectly by helping me or influencing me in one way or another. Thanking everyone would be the proper and impossible thing to do, but some people have more than just deserved thanks, they shaped me as a scientist and a person.

First of all, my adviser, Shinhong Kim, to whom I am grateful for giving many advices to me. He introduce me to CDF group when I started study for CDF. I discussed with him when the research comes to a standstill. He also make corrections on this thesis. I express my deepest appreciation to Tom Junk for extremely useful discussion for all period of my stay in U.S. This thesis could not be posted without Bernd Stelzer, who teaching me to seek the meaning of all things about my analysis from begin of my stay in U.S. So I have to thank to him. I also would like to thank Craig Group who gave me many advices especially to my latest result in this thesis. I have to extend my appreciation to all the people in the Single top Group at CDF, especially, Peter Dong, Florencia Canelli, Catalin Ciobanu, Sarah Budd, Ji-Eun Jung, Jan Lück, Dominic Hirschbühl, Wolfgang Wagner, Jeannine Wagner-Kuhr, Bruno Casal Laraña. I express my gratitude to the additional legions of great physicists at CDF who gave helpful advices to me sometimes in the meeting and sometimes in the corridor with person-to-person discussion.

I am very grateful to the legions of excellent physicists and engineers in Fermilab's Accelerator Division who keep the accelerators running smoothly, and to the additional legions of excellent physicists at CDF who are responsible for the design, construction, and operation of the detector, as well as the offline processing, reconstruction algorithms, particle identification and all the other essential studies without which this analysis would not be possible.

I have to thank all the staffs in University of Tsukuba, Fumihiko Ukegawa, Kazuhiko Hara, Takasumi Maruyama, Yuji Takeuchi, Tomonobu Tomura, Hideki Miyake and Masakazu Kurata. They directly contributed to my study for this thesis many times. I'd like to thank to all the Japanese people working in Fermilab who replies to the informal discussion, especially to the staffs, Kenichi Hatakeyama, Koji Sato, Kohei Yorita, Yuji Enari and Masato Aoki, and to the additional legions of PhD students, Junji Naganoma, Tatsuya Masubuchi, Taichi Kubo, Ai Nagano, Naoki Kimura, Takayuki Wakisaka, Yoshikazu Nagai and Atsunari Hamaguchi. In addition, extend my heartfelt appreciation to all of my friends who shared with me sad and happy days in Fermilab and Japan. I also would like to thank to Carol Picciolo, Kyoko Kunori and Kazuko Kumashiro who supported me with a lot of kindness, taking care of my trips and other secretary works.

Finally, I thank my parents for bringing me up the way I am, for always believing in me and for always encouraging me to do what I feel is right and study what I think is interesting.

Contents

List of Figures

List of Tables

Chapter 1

Introduction

What does the world consist of? – The Standard Model of elementary particle physics provides a part of answer for this question. This Model describes the elementary components of matter as well as the force between them. The substructure of matter is only visible in scattering experiments. In high energy physics, these experiments are done at particle accelerators. The world highest-energetic collider, the Tevatron, is hosted by Fermi National Accelerator Laboratory (FNAL), also called Fermilab, located in the vicinity of Chicago. The proton-antiproton collisions at a center-of-mass energy of $\sqrt{s}$ =1.96 TeV are recorded by two multipurpose detectors, CDF and DØ . Fermilab experiments are described in Chapter 2.

1.1 The Standard Model

The Standard Model of elementary particle physics is a theory that describes the fundamental constituents of the universe and their interactions. In this theory, all matter is composed of spin-$\frac{1}{2}$ fermions, known as "quarks" and "leptons". These fermions interact via a few fundamental forces, electromagnetic, weak and strong [1], mediated by spin-1 bosons.

Fermions

Quarks and leptons are arranged into three generations; the particles in each generation have similar relationships, but are of differing masses. There are six "flavors" of quarks, which can be classified into two general types, "up"-type and "down"-type after the prototypes in the first generation. The quarks have electromagnetic charge, weak isospin, and color charge, so are affected by all the forces. Due to the nature of the strong force, quarks exist only in bound states called "hadrons" and are not detected as free. There are also six leptons, three electrically charged leptons of which the electron is prototype, and three neutrinos. The neutrinos participate only in weak interactions while the charged leptons interact electromagnetically as

[1] Gravity is extremely weak in comparison to the other forces and is not included in the Standard Model.

Table 1.1: The fundamental particle content of the Standard Model. The mass values are taken from the Particle Data Group [1]. We denotes Q and S for charge and spin of particles, respectively. We do not provide uncertainties for the masses of e, μ and τ lepton, since they have precisions smaller than the significant digits shown in this table. The u-, d- and s-quark masses are estimates of so-called "current-quark masses", in a mass-independent subtraction scheme at scale $\mu \approx 2$ GeV . The c- and b-quark masses are "running" masses in the mass-independent subtraction scheme. For the b-quark we quote the 1S mass. t-quark mass is based on the direct measurement using the data from Tevatron Run I and Run II [6]. The neutrino masses are measured based on fitting the shape of the β decay spectrum.

	Fermion Generation 1	2	3
Quarks	u 1.5-3.3 MeV/c^2	c $1.27^{+0.07}_{-0.11}$ GeV/c^2 Q=$+\frac{2}{3}$, S=$\frac{1}{2}$	t 172.4$\pm$1.2 GeV/c^2
Quarks	d 3.5-6.0 MeV/c^2	s 104^{+26}_{-34} MeV/c^2 Q=$-\frac{1}{3}$, S=$\frac{1}{2}$	b $4.20^{+0.17}_{-0.07}$ GeV/c^2
Leptons	e 0.511 MeV/c^2	μ 106 MeV/c^2 Q=-1, S=$\frac{1}{2}$	τ 1.78 GeV/c^2
Leptons	ν_e $<$ 2 eV/c^2	ν_μ $<$ 0.19 MeV/c^2 Q=0, S=$\frac{1}{2}$	ν_τ $<$ 18.2 MeV/c^2

well. The quarks and leptons, along with some of their basic properties, are listed in Table 1.1. For each particle, there is a corresponding antiparticle with identical mass but opposite charge.

Gauge Bosons

The Standard Model is a gauge field theory that is invariant under a set of transformations that form the group

$$G = SU(3) \times SU(2) \times U(1). \tag{1.1}$$

The particles of the Standard Model have internal invariance under transformations in each of the subgroups of G, with associated gauge bosons for each transformation. Electroweak theory, described by $SU(2) \times U(1)$, unifies the electromagnetic force, which is mediated by the massless photon, and the weak force, mediated by the massive charged $W^{\pm}$ bosons and the neutral Z boson. The masses of the W and Z bosons arise through the Higgs mechanism, which spontaneously breaks the symmetry of the electroweak Lagrangian. Also arising out of this mechanism is the Higgs boson, the sole remaining Standard Model particle to be observed. Strong interactions are described by QCD, $SU(3)$ component. Eight massless gluons mediate

Table 1.2: List of Standard Model gauge bosons, with the force to mediate, electrical charge, spin and mass. The mass values shown here are taken from the Particle Data Group [1].

Particle, symbol	Force	Electrical charge	Spin	Mass (GeV/c^2)
Gluon, g	Strong	0	1	0
Photon, γ	Electromagnetic	0	1	0
W boson, $W^{\pm}$	Weak (charged)	± 1	1	80.398$\pm$0.025
Z boson, Z	Weak (neutral)	0	1	91.1876$\pm$0.0021

the strong force and themselves carry the corresponding charge (color). The basic properties of gauge bosons are summarized in Table 1.2.

The Higgs Mechanism

Masses in the Standard Model arise through interactions with a scalar field, Higgs field, that permeates the vacuum. The Higgs field couples to the bosons and fermions without spoiling the gauge-invariance or renormalizability of the Standard Model. The Higgs field can be thought of as a viscous fluid. Any particle traveling through experiences drag force due to this fluid, is which creates the mass. The interaction with the Higgs field mixes the $SU(2)$ and $U(1)$ gauge bosons and endows them with mass, in a process known as "spontaneous symmetry breaking". The masses of the $W^{\pm}$ and Z bosons result from their interaction with the Higgs field, and can be written as $M_W = \frac{1}{2}vg$ and $M_Z = \frac{1}{2}v\sqrt{g^2 + g'^2}$ where g and g' variables characterize the coupling strength of the weak and electromagnetic fields, respectively. v is the vacuum expectation value of the Higgs field when Higgs is represented as $SU(2)$ doublet of complex scalar fields. The photon remains massless, which is consequence of the conservation of electric charge.

Excitation of Higgs field from its vacuum expectation value shows up in the form of Higgs boson, H. The Higgs boson couples to mass, meaning that it prefers to decay to the heaviest possible channels available to it. The current expected value of the Higgs mass is 84^{+36}_{-26} GeV/c^2 ($<$ 175 GeV/c^2 at 95% Confidence Level, C.L.) from the Standard Model fitting to various experimental data [1]. Direct searches at LEP experiments and Tevatron experiments have excluded the Standard Model Higgs below 114.4 GeV/c^2 [2] and at a point of 170 GeV/c^2 [3] at the 95% C.L.

CKM Matrix

The Standard Model, which has been extremely successful in explaining and predicting many aspects of particle interactions, is not quite complete. The current formulation of the Standard Model includes three sets, or generations, of fundamental particles called fermions. There is, however, no intrinsic reason that there must be only three generations, though a fourth has not yet been observed. Only one Standard Model process, the charged weak interaction, is capable of transforming a single fermion to another fermion directory via massive boson, namely the electrically charged $W^{\pm}$ boson. The probability of this occurring among the quark is parameterized by a mixing matrix called the Cabbibo-Kobayashi-Maskawa (CKM) matrix.

Most elements of the CKM matrix have been precisely measured by past and present particle accelerator experiments. However, the element $|V_{tb}|$, which represents the probability that a top quark will change to bottom quark through electroweak interactions, has become experimentally probable recently. Limits on other elements indicate that its value must be very close to one if there are only three generations of fermions. Because the total probability must be unity, any direct measurement of $|V_{tb}|$ that is significantly less than one would indicate the existence of a fourth generation [19].

Measuring $|V_{tb}|$ requires an investigation of the top quark, the most massive known fundamental particle. The only facility currently capable of generating the energy needed to produce top quarks is the Tevatron. However, top quarks are predominantly produced in pairs by the strong interaction. Measuring $|V_{tb}|$ requires examining a less common process, "single top production", in which only one top quark is produced. The cross section of this interaction is proportional to $|V_{tb}|^2$; thus, a measurement of the cross section for electroweak single top quark production allows a measurement of $|V_{tb}|$.

1.2 The Top Quark

The top quark discovered in proton-antiproton collisions with a center-of-mass energy of 1.8 TeV (Tevatron Run I) [5] in 1995 [2] by the CDF and DØ collaborations is the heaviest known elementary particle. Having a mass of ~170 GeV/c^2 , the top quark is approximately 40 times the mass of the next heaviest bottom quark. The Yukawa coupling between the Higgs boson and top quark is ~ 1, giving rise to the question of whether the top quark plays a role in the electroweak symmetry breaking mechanism. The heavy mass of the top quark offers a unique window to search for physics beyond the Standard Model.

Top Quark Production and Decay

At the Tevatron, top quarks are produced predominantly in pairs via the strong interaction. To calculate the production cross section for $p\bar{p} \rightarrow t\bar{t}$, it is necessary to take into consideration the structure of the incoming protons. Because protons are not elementary particles, but are made of quarks and gluons, the initial state of the actual interaction is complicated. However, if the momenta of the incoming particles are high enough ($\gg \Lambda_{\mathrm{QCD}} \approx 200$ MeV), it is possible to calculate the cross section using perturbative QCD, treating the interaction as one between only two elementary particles.

[2] CDF Collaboration presented the first direct evidence for the top quark in 1994 [4].

In the $p\bar{p}$ collisions at the Tevatron, $t\bar{t}$ pairs are produced through quark pair ($q\bar{q}$) annihilation or gluon-gluon (gg) fusion. At the Tevatron energy-scale, production through $q\bar{q}$ annihilation accounts for about 85% of $t\bar{t}$ pairs produced while remaining 15% are a result of gg fusion. This is because the energy needed to produce the massive top quarks requires the interacting partons to carry a significant fraction of the proton's (antiproton's) momentum, as described later, the u and d quarks carrying most of the proton's momentum.

In the Standard Model, the top quark decays into a b quark and a W boson nearly 100% of the time via weak interaction. W boson can decay either leptonically to a charged lepton and a neutrino or hadronically to a pair of quarks. Top-pair events are categorized by the decay of the W bosons; they may be "all-hadronic", "lepton-plus-jets", or "dilepton" events depending on whether neither, one, or both of the Ws decays leptonically, respectively. At leading order the W has a leptonic branching fraction 1/9 for each channel and a hadronic branching fraction of 6/9; thus the all-hadronic channel has the largest branching fraction while having the largest background. It makes studying the top quark in this channel very challenging. The dilepton channel, on the other hand, is very clean, meaning contribution from background are small, however, this channel suffers from a low branching fraction. The lepton-plus-jets channel has a relatively high branching fraction of about 30%. Though the backgrounds are considerably higher than in the dilepton channel, they are still manageable.

1.3 Parton Distribution Function and Production Cross Section

Unfortunately, the initial momenta of the particles, called "parton", cannot be determined on an event-by-event basis. Each parton carries a fraction (x) of the proton, or antiproton, momentum according to a statistical distribution that depends on its type, gluon or quark flavor, and on the energy scale; this distribution is known as a parton distribution function (PDF). Figure 1.1 shows the proton PDFs, provided by CTEQ group [9] with HERA and the Tevatron data included. The valence quarks, u and d, are most likely to carry a large fraction of the proton momentum, though gluon can carry a significant fraction as well. To theoretically evaluate the cross section, one must sum over all possible interactions, weighted by their probability according to the PDFs. Thus, the cross section of process $p\bar{p} \to X$ is given by:

$$\sigma = \sum_{i,j} \int dx_i dx_j f_i(x_i, \mu^2) f_j(x_j, \mu^2) \hat{\sigma}(p_i p_j \to X), \tag{1.2}$$

where the sum is over all possible initial parton states, $p_i p_j$. $f_i(x_i, \mu^2)$ is the PDF of a parton of type i at a given momentum fraction, x_i, and an interaction energy scale, μ. The cross section for the individual parton-parton interaction is represented by $\hat{\sigma}(p_i p_j \to X)$.

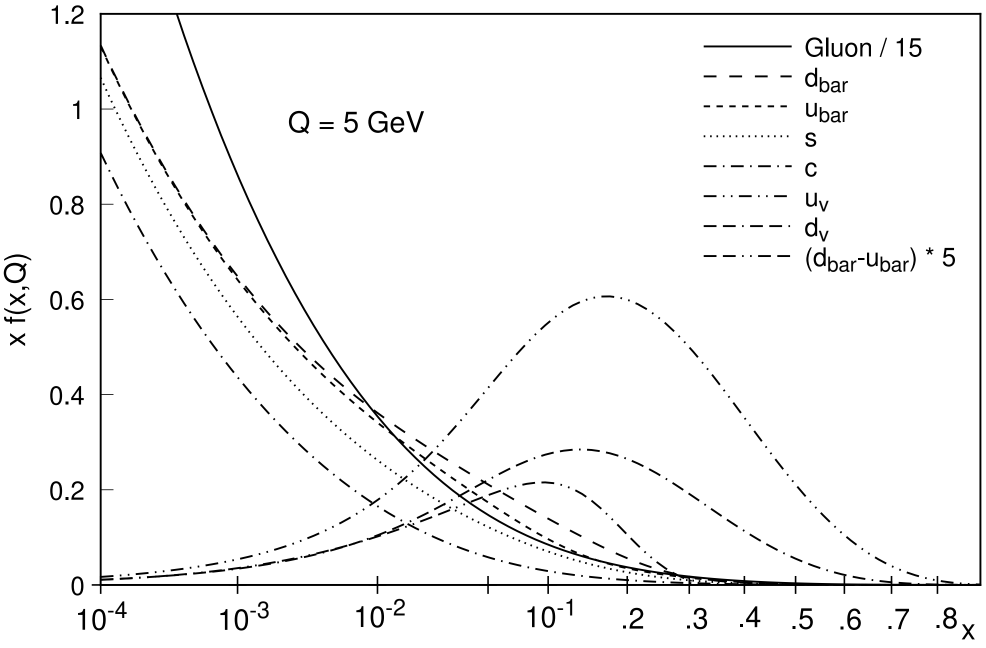

Figure 1.1: Parton distributions as a function of the fractional momentum x at a momentum transfer of $Q = 5$ GeV from CTEQ version 5 parameterization. The gluon distribution is scaled down by a factor of 15, and the $\bar{d} - \bar{u}$ distribution is scaled up by a factor of 5 [10].

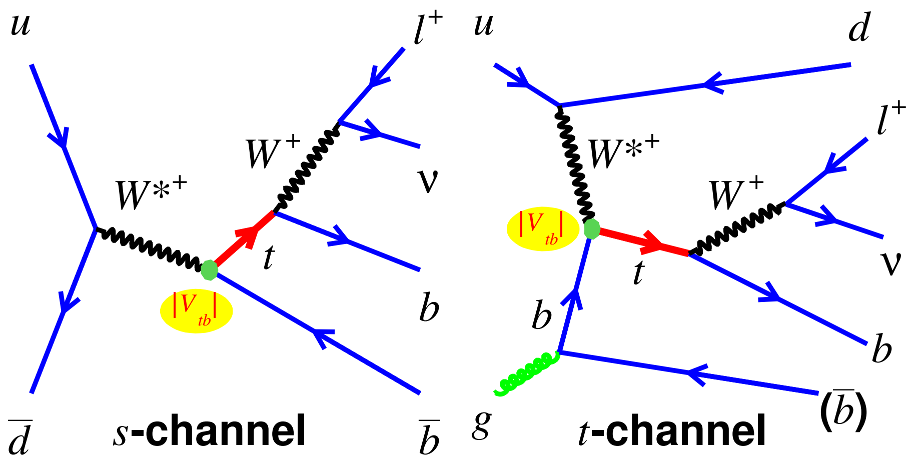

Figure 1.2: Typical processes of single top quark production at Tevatron. Left figure shows s-channel feyman diagram and right figure shows t-channel feyman diagram.

1.4 Single Top Production

Since the strong force has a stronger coupling than the other forces, the production of top quark pairs is dominant. However, top quarks can also be produced through electroweak interactions. The typical processes of single top quark production at the Tevatron are illustrated in Figure 1.2. The t-channel mode, illustrated right, involves the exchange of a space-like W boson between a light quark and a bottom quark inside the incident hadrons, resulting in two jets(b-quark jet may be contained inside the beam pipe) and a single top quark. Its production cross section is 1.98 pb [20] at Tevatron. The s-channel mode involves production of an off-shell, time-like W boson, which then decays into a top and bottom quark. It has a relatively small cross section, 0.88 pb [20] at Tevatron. There exists a tW mode of single top quark production involving an initial state b quark emitting a on-shell W boson, resulting in a tW final state. This process has extremely small cross section at the Tevatron, but is considerable at the LHC where more partonic energy is available. Each mode has rather distinct event kinematics, and thus is potentially observable separately from each other.

However, studying single top quark production involves many experimental challenges. Single top production occurs at about one third the rate of top pair production, which is already a rare process. At the same time, the background processes which look similar to single top production occur more than ten times frequently. Simple experimental techniques are not sufficiently sensitive to measure a single top cross section with such an enormous "background"; more advanced event likelihood function techniques are used to separate the single top signal from the background, and evaluate the cross section.

Measurement of the single top production cross section allows the measurement of several

Standard Model parameters. The most important of these is the CKM matrix element $|V_{tb}|$, which is the probability amplitude that top quark couples to a bottom quark in a charged weak interaction, and can only be directly measured in single top production. Other measurements of $|V_{tb}|$ have been made by studying the rates of top quark decay [7]. These measurements assume three families, because if a fourth family of quarks heavier than top existed, the top quark would be unable to decay to these particles. In the case of single top production, however, the cross section is directly proportional to the square of $|V_{tb}|$. Measuring the single top production cross section gives a measurement of $|V_{tb}|$ that makes no assumption about the number of fermion families. The measured $|V_{tb}|$ is calculated as follows:

$$|V_{tb}^{\text{measured}}|^2 = \frac{\sigma_{\text{measured}}}{\sigma_{\text{SM}}} \times |V_{tb}^{\text{SM}}|^2, \tag{1.3}$$

where σ_{measured} and σ_{SM} are the measured and theoretical single top quark production cross section, respectively. $|V_{tb}^{\text{SM}}|$, which is the theoretical value of $|V_{tb}|$, is mostly unity. We use 2.86±0.44 pb as the theoretical cross section value, σ_{SM} [**?**].

In addition, the Standard Model predicts that the top quark resulting from this interaction will be almost entirely polarized, since the W boson only interacts with left-handed particles [11]. This polarization allows a probe of the spin projection of the quark and the chirality of the W boson.

Discovering single top production is also an important milestone in the search for the Higgs boson. The signature of WH production, which is the most sensitive mode for a low-mass Higgs at the Tevatron, has the same final state as single top production. Searches for the Higgs boson face similar challenges to single top searches, so they will most likely employ similar techniques. A single top production measurement is thus a proving ground for the sophisticated analysis methods needed to observe the Higgs boson.

Two dominant processes, s- and t-channels, illustrated in Figure 1.2 can be measured separately. Leptonically decay s-channel process has a final state of lepton, neutrino and two b quark jets. The t-channel process has a final state of lepton, neutrino, a light quark jet and a b quark jet [3]. These two processes could be separated, although b quark jet identification is very important.

The two modes of single top quark production are sensitive to quite different manifestations of physics beyond the Standard Model. Beyond the Standard Model signals can be classified as to whether they involve the effects of a new particle (either fundamental or composite) that couples to the top quark, or the effect of a modification of the SM coupling between the top and other known particles. The correlation of the s- and t- channel cross sections in the plane of $\sigma_s - \sigma_t$, shown in Figure 8.6, has to be studied in order to attempt to understand if a new physics effect is present, and how one should interpret it if it is observed. Examples of additional non-

[3] Since a $\bar{b}$ quark of t-channel process shown in Figure 1.2 is typically generated to very close to the beam direction, our detector cannot detect this particle.

standard model particles include extra quark with fourth generation scenario (such as a b' quark that couple to W boson and top), extra gauge boson (such as a W' vector boson that couples to top and bottom), extra scalar boson (such as a $H^{\pm}$ boson or charged top-quark-pion [12] that couples to top and bottom). An example of modified top quark interactions is the electroweak chiral Lagrangian (EWCL) [13] with the flavor-changing neutral current (FCNC). In addition, top-color [14] and top-flavor [15] models, which rely on additional fermions to participate in a seesaw mechanism to generate the top quark mass and have additional gauge bosons, also modify s- and t- channel cross section ratio.

DØ collaboration has reported evidence for single top quark production using 0.9 fb^{-1} of data [16] while measuring a cross section of $\sigma_{s+t} = 4.7 \pm 1.3$ pb. CDF collaboration has also reported single top quark production cross section in 2.2 fb^{-1} of data [17] while observing a signal consistent with the standard model prediction, but inconsistent with te background-only model by 3.7 standard deviation. This signal corresponds to the cross section of $\sigma_{s+t} = 2.2^{+0.7}_{-0.6}$(stat+syst) pb, extract the CKM matrix element value $|V_{tb}| = 0.88^{+0.13}_{-0.12}$ (experiment) ± 0.07 (theory), and set the limit $|V_{tb}| > 0.66$ at the 95% C.L.

Since the current single top analyses [17] by CDF are optimized to t-channel production, s-channel optimized search is important to be sensitive to any indications of beyond the Standard Model phenomena. A cross section larger than predicted in the s-channel mode of production could indicate the presence of other processes discussed above that have the same final state. In this analysis, we focus on s-channel processes of single top quark production.

This thesis presents a measurement of single top quark production, involving s-channel and t-channel processes, and a new search for the s-channel production process in proton-antiproton collisions at the Tevatron with an integrated luminosity of 2.7 fb^{-1}. Chapter 2 describes the experimental setup, Tevatron and Collider Detector at Fermilab. In Chapter 3, event reconstruction is discussed. Chapter 4 describes the modeling of signal and background processes. Chapter 5 presents the requirements used to select candidate events for this analysis. Chapter 6 discusses the estimate of the rate of each process. The analysis method is introduced in Chapter 7, and Chapter 8 applies it to the data to measure the single top production cross section and $|V_{tb}|$. Chapter gives the conclusion and discusses potential future improvements of the analysis.

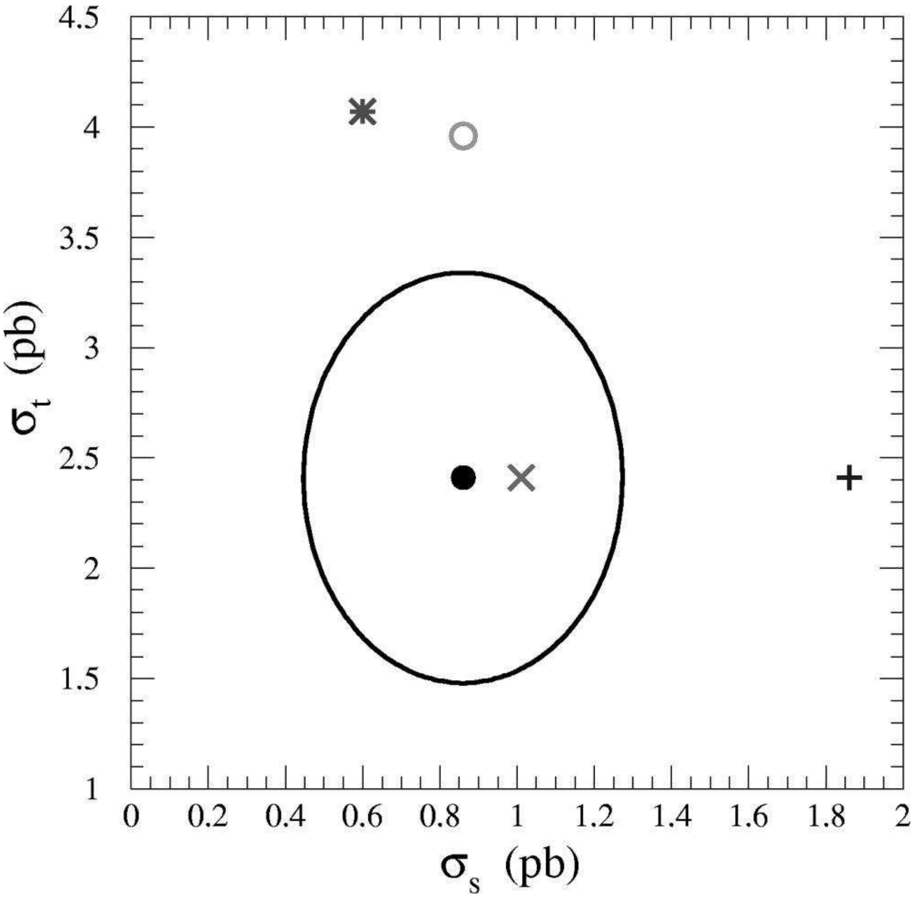

Figure 1.3: The location of the Tevatron SM point (the solid circle)in $\sigma_s - \sigma_t$ plane, and the 3σ theoretical deviation curve. The t-channel cross section is not identical with [20], since this figure shows the cross section calculated in leading-order. Also shown are the points for the top-quark-flavor model as the $\times$, the FCNC Z-t-c vertex as the open circle, a model with a charged top-quark pion as the cross, and a four quark generation scenario as the asterisk. All models assumes typical parameter points [18].

Chapter 2

Experimental Setup

The Fermi National Accelerator Laboratory (FNAL), or Fermilab, has been the home of several great discoveries in particles physics - the bottom quark was discovered at Fermilab in 1977, the top quark in 1994-1995 and the τ neutrino in 2000. Fermilab is home to the Tevatron and the two large collaborations devoted to studying proton-antiproton collisions, the Collider Detector at Fermilab (CDF) and DØ collaborations. There are also two neutrino experiments, MiniBooNE and Minos. In this chapter we will focus on the Tevatron and the CDF II detector [21]. These are huge and complicated machines that cannot be fully described in a few pages. This chapter is meant to be an overview that highlights the important components for this analysis.

2.1 The Tevatron

The Tevatron at Fermilab is the last and highest energy stage of the large accelerator complex. This accelerator complex at Fermilab was first established in 1969. The physics program began in 1972 with proton beam energies of 200 GeV for fixed target experiments. After installing super conducting magnets, the first $p\bar{p}$ collisions at 1.8 TeV started in 1986. Since then, several extensive upgrades have been undertaken to improve the overall performance. Radio-frequency(RF) buckets are used to accelerate the particles and define the bunches. While operating in a collider mode, the Tevatron collides 36 bunches each of protons and antiprotons every 396 ns with beam energy of 980 GeV , currently the highest in the world. Once the beams are injected and accelerated, collision are made to occur at two points along the ring, inside the CDF and DØ detectors. The schematic of the Fermilab accelerator complex is shown in Figure 2.1.

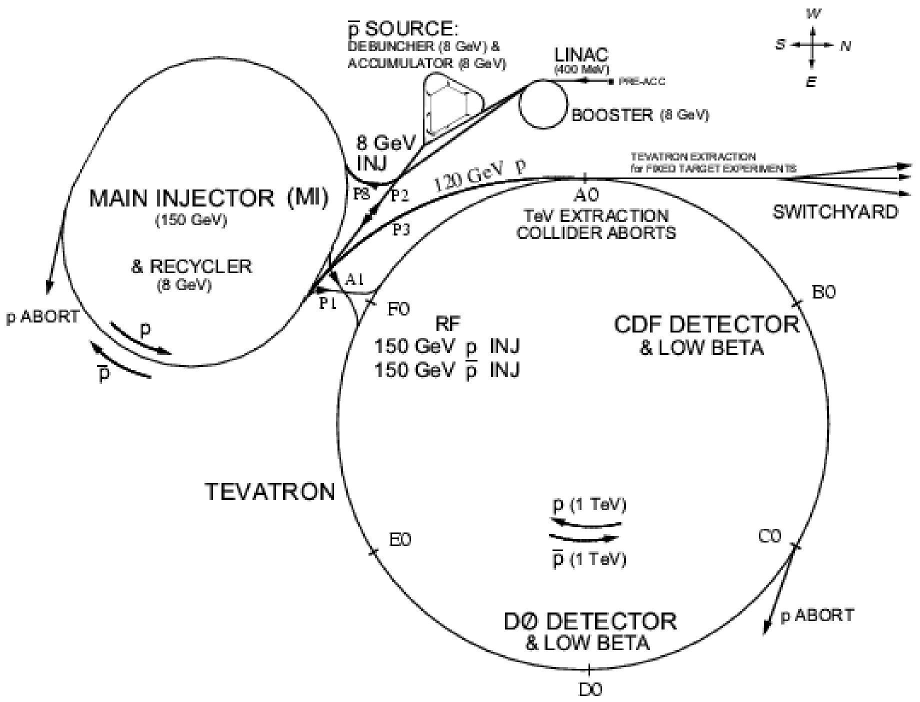

Figure 2.1: Schematic of the Fermilab accelerator complex.

2.2 Proton Antiproton Production

The first stage in the acceleration of protons is the commercial Cockcroft-Walton accelerator, which boosts H^- ions produced by ionization of gaseous hydrogen to 750 keV . The ions are then injected into a 150 m long linear accelerator ("Linac") which increases their energy to 400 MeV . The Linac is made up of two types of RF stations, which are electromagnetically resonant cavities with natural resonant frequencies lying within the radio frequencies of the electromagnetic spectrum. A carbon foil is used to strip the two electrons from H^- before the resulting protons are injected into the "Booster". The Booster is a circular synchrotron with 18 RF cavities distributed about a ring with a 75 m radius. The 201 MHz frequencies of the bunches from Linac do not match the 37.8 MHz frequencies of the RF cavities in the Booster. After all the bunches have been injected, and flattened in the booster, the protons eventually come into phase with the cavities, and a new 37.8 MHz bunch structure is formed and accelerated to 8 GeV . The protons are transfered to the "Main Injector" which brings their energies to 150 GeV . The Main Injector is a circular synchrotron with 18 accelerating RF cavities and a circumference of almost 2 miles (completed in 1999), approximately half the circumference of the Tevatron. The final step of the process is the transfer to the Tevatron, a synchrotron which employs superconducting Nb-Ti alloy filaments embedded in copper as magnet coils. The magnetic field of 5.7 T keeps the protons on an approximately circular orbit while they reach the final energy of 980 GeV .

Once the proton bunches circulating in the Main Injector reach an energy of 120 GeV , some are slammed into a rotating 7 cm thick nickel or copper target to produce antiprotons through the reaction

$$p + \begin{pmatrix} n \\ p \end{pmatrix} \rightarrow p + p + \begin{pmatrix} n \\ p \end{pmatrix} + \bar{p}. \tag{2.1}$$

Before colliding, the proton bunches are rotated by 90° in phase space, so that they have a large spread in energy but a small lag in arrival time at the target. A spatially broad shower of particles is produced and then focused into a beam via cylindrical lithium lens. This beam, which has a bunch structure similar to the incident proton beam, is passed through a pulsed dipole magnet. The magnetic field separates the negatively charge antiprotons with about 8 GeV of kinematic energy. About 20 antiprotons are produced for every 10^6 protons on target and then stored into the "Debuncher". The Debuncher is a triangular-shaped synchrotron with mean radius of 90 m. The beam is stochastically cooled by picking up signal from antiproton circulating in one side of the ring. After cooling, the antiprotons are then transferred to the "Accumulator", which is another triangular-shaped synchrotron with a mean radius of 75 m. The Accumulator is a storage ring for the antiprotons; there they are stored at 8 GeV and cooled until needed for acceleration in the Main Injector, where they are accelerated to 150 GeV . Finally, the antiprotons are also transferred to the Tevatron, where 36 previously injected bunches of protons are already circulating in opposite direction. Since 2004, an additional Recycler Ring has been added in the same tunnel as the Main Injector and provides additional storage of antiprotons. By limiting the stack size, the Debuncher allows an optimization of antiprotons accumulation rate, while this rate is the largest limiting factor for the Tevatron luminosity.

2.3 The Collision and Luminosity

In order to create collisions, 36 bunches of protons are injected into Tevatron first. Twelve bunches each separated by 21 RF (396 ns) are grouped together into three trains of bunches. The trains have a larger separation of 140 RF buckets and the gaps provide enough space to insert the next 36 bunches of antiprotons without disturbing the protons.

The antiproton bunch pattern is a mirror image of the proton pattern and circulates along the Tevatron in the opposite direction within the same magnet and vacuum systems. The energy of the machine is increased in about 10 seconds from 150 to 980 GeV .

Special quadrupole magnets (low-β squeezers) located at the CDF and DØ detectors along the beam pipe squeeze the beam in order to maximize luminosity inside the detectors. A roughly Gaussian distribution of the interaction region along the beam axis is achieved with $\sigma \approx 30$ cm.

The transverse shape of the interaction region has an almost circular spatial distribution with a diameter of 30 μm.

The Tevatron performance can be expressed primarily in terms of two parameters, the center-of-mass energy, $\sqrt{s}$, and the instantaneous luminosity, $\mathcal{L}$. $\sqrt{s}$ defines the accessible kinematical phase space for the production of particles in the final states and $\mathcal{L}$ relates the production rate. The production rate R of a given process and its cross section σ is expressed by

$$R[\text{events/s}] = \mathcal{L} \times \sigma. \tag{2.2}$$

With ideal head-on $p\bar{p}$ collision, the instantaneous luminosity is given by:

$$\mathcal{L} = \frac{fBN_pN_{\bar{p}}}{2\pi(\sigma_p^2 + \sigma_{\bar{p}}^2)}F(\sigma_l/\beta^*), \tag{2.3}$$

where f is the revolution frequency, B is the number of bunches in each beam, N_p ($N_{\bar{p}}$) is the number of protons (antiprotons) in each bunch, σ_p ($\sigma_{\bar{p}}$) is the rms of proton (antiproton) beam size at the interaction point, and F is a form factor which depends on the ratio of longitudinal rms length σ_l to the beta function at the interaction point, β^*.

Due to beam-beam interactions and collisions, the instantaneous luminosity decreases exponentially over time. The beam is usually dumped intentionally after 15-20 hours of recording collisions and replaced with a new store.

2.4 The CDF II Detector

The Collider Detector at Fermilab, known as CDF, is a multipurpose particle detector built at the Tevatron B0 interaction point. It is approximately 15 m long and 10 m high maintaining approximate axial and forward-backward symmetries.

The particles that are produced at the interaction traverse through various detector subsystems. The first one they encounter is the tracking system, then calorimetry and finally the muon subdetectors. These are the basic components that provide the data that serves as the foundation of our measurement. Cherenkov Luminosity Counters (CLC) [28] located very close to the beampipe in the plug are installed to measure instantaneous luminosity. Various other components exist which are essential to some physics analysis, for instance the Time-of-Flight detector (TOF) and Central PRe-shower counter (CPR). They are not used in this particular analysis and are described elsewhere. The schematic overview of the CDF detector is shown in Figure 2.2

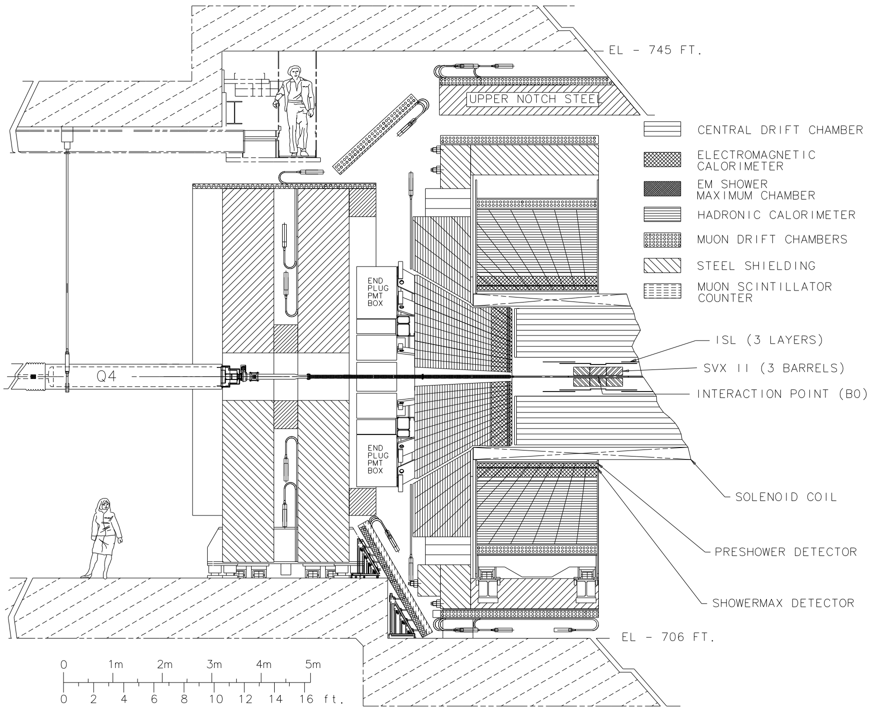

Figure 2.2: CDF II detector.

CDF coordinate system

The CDF detector coordinate system is as follows: z axis is along the beam line; $+z$ is proton travel direction (east) while $-z$ is antiproton one (west) with the interaction point at $z = 0$. x axis is horizontal direction ($+x$ = north,$-x$ = south), y axis is up-down direction ($+y$ = up,$-y$ = down).

r and θ are the radial distance and the polar angle from the beam line; $\theta = 0°$ and $\theta = 90°$ are straight up and $\theta = 180°$ in the $-z$ direction, respectively. Usually instead of θ, we use *pseudo-rapidity*, defined in the following way:

$$\eta = -\ln\left(\tan\frac{\theta}{2}\right) \tag{2.4}$$

Particles perpendicular to the beam line have $\eta = 0$. η is preferred over θ in hadron collider experiments because the difference in η's is Lorentz invariant. In hadron collider, the z-component of the colliding partons are not exactly 0, so the produced particles are subject to boost along z-direction. ϕ is the azimuthal angle around the beam line; $\phi = 0°$ corresponds to positive x direction, $\phi = 90°$ to up and $\phi = 180°$ to negative x direction.

CDF Tracking Volume

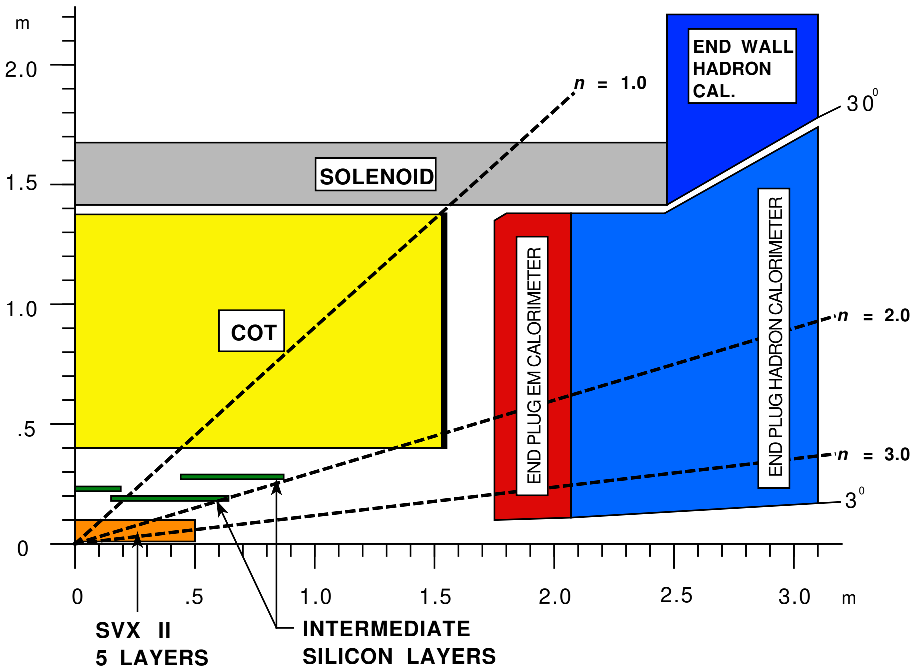

Figure 2.3: The CDF tracking system.

Tracking

The CDF tracking system consists of the Central Outer Tracker (COT) [22] and silicon detector subsystem that is divided into Silicon VerteX detector (SVX) [23], Intermediate Silicon Layers (ISL) and Layer 00 (L00).

The entire tracking volume resides inside a superconducting solenoid magnet [24] with the radius of 1.5 m and the length of 4.8 m. It creates a uniform magnetic field of 1.4 T along the direction of the z-axis. The trajectory of a charged particle in magnetic field is a helix. From the parameters of the helix the particle momentum can be determined, as the magnitude of the magnetic field is known.

The schematic view of the CDF tracking system in the (r-z) plane is shown in Figure 2.3. The region of the detector with $|\eta| \leq 1.0$ is referred as "central".

As can be seen from Figure 2.3, a charged particle that is produced in the central interval has to travel through the entire COT tracking volume and thus has a better transverse momentum measurement than a particle with $|\eta| > 1.0$. The region $1.0 < |\eta| \leq 3.6$ is called "plug" or "forward".

The first subdetector that a particle created in a collision traverses is the Silicon detector. The main part, SVX, consists of three cylindrical barrels placed end-to-end in z; each is 29 cm long with five layers of double sided micro-strip silicon wafers. It occupies the radial space between 2.1 and 17.3 cm. The technology used allows the measurement of electron-hole pairs induced by a charged particle traversing the silicon wafer, providing the "hit" position with the precision of 12 μm. The double-sided silicon microstrips that are used in SVX and arranged so that one side of a wafer has axial strips, while the other side hosts either 90° stereo strips or small angle 1.2° stereo strips. Such an arrangement makes is possible to combine the (r-ϕ) and (r-z) measurements into the three-dimensional position measurement.

Both the ISL and L00 are the extensions to the silicon tracking subsystem. The L00 consists of a layer of single-sided radiation-hard silicon microstrips mounted directly onto the beampipe at radii of 1.35 and 1.62 cm. It provides the position measurement closest to the interaction point. The ISL consists of single or double layers of double-sided silicon placed at radii of 22 (central), 20 and 28 cm (forward/backward). It is aimed at extending the tracking coverage to the region of $1.0 \leq |\eta| \leq 2.0$ as well as to provide help with resolving any ambiguities in matching COT tracks with SVT tracks in a dense-track environment.

The individual "hits" both from the COT and the silicon detectors are linked together with pattern-recognition software into a "track", the entity that describes the trajectory of the charged particle. The measure of the performance of the tracking system can be illustrated by the ability to determine the parameters of helix trajectory. The resolution in the impact parameter that is achieved by the tracking system is about 40μm, and the z_0 resolution is about 70μm, where z_0 is the z coordinate of the closest approach of the track to the z-axis.

The Silicon detector subsystem has 722,432 readout channels. The hit data is collected, assembled and packed for transmission by radiation hard integrated circuits. The data is transported via an optical fiber link to the external data-processing units.

Precise position measurements with the Silicon Vertex detector are used to extrapolate the tracks all the way to the collision region. It is crucial for the determination of the vertex position and provides a measurement that can distinguish a particle which is coming from a primary interaction from a particle which is produced at a secondary displaced vertex and thus is a decay product of some long lived particle.

After a charged particle exits the Silicon detector it passes through the Central Outer Tracker. The COT occupies the region with $|z| <$155 cm and 44$< r <$132 cm. It is a cylindrical multi-wire open-cell drift chamber filled with an Argon-Ethane gas mixture, which was chosen as it provides a uniform drift velocity. The gas mixture used has the maximum drift time of about 180 ns in the drift field of 1.9 kV/cm. This design constraint, stems from the need to avoid event pileup; consequently the maximum drift time is required to be less than 396 ns.

The COT consists of 30,240 sense wires grouped into eight super layers. The superlayers alternate between axial and stereo, with the latter having the wires strung at $\pm 2°$ with respect to the axial direction. Each charged particle that escapes the COT traverses 96 layers of sense wires that ideally can provide the same number of position measurements. The single hit resolution of the COT is about 140 μm. The track reconstruction software converts the individual hits into the fitted particle trajectories, the helix parameters of which allow the measurements of charged particle momenta. It results in the transverse momentum resolution of $\frac{\Delta p_T}{p_T} \approx 0.15\% p_T(\mathrm{GeV/c})^{-1}$.

Whenever possible the hit information from both the COT and Silicon detector is combined to produce the best track fit possible. For the particles with very hight momenta the track parameters are harder to determine precisely as the curvature of the helix is quite small. Fortunately for some of the particles, in particular electrons, an additional precision measurement of their energies is possible via the Calorimetry subsystem.

Calorimetry

Charged particles with energies greater than 350 MeV may leave the tracking volume and propagate beyond the solenoid magnet that surrounds it. Neutral particles, both photons and neutral hadrons, leave the tracking volume undetected. Even if they were seen by a tracking system no information about their momenta would be available for a quite obvious reason – their trajectories do not bend in magnetic field. In many of cases the measurement of their momenta and energy is essential for the understanding of observed events. The calorimetry subsystem serves the measurement of both charged and neutral particles, based on the fact that particles that have reasonable high electromagnetic or hadronic interaction cross-sections propagate through matter, transferring their energy to the medium until eventually all of it is absorbed. Active media produce measurable response to such energy depositions by emitting light in amounts dependent on the amount of energy lost by the particles.

The CDF calorimetry system consists of alternating layers of scintillator and absorber material. As particles interact with absorber they produce cascade of particles or "showers" that penetrate the scintillator. The light from the latter is guided into the photomultipliers. Their response is in turn digitized and with the help of relevant calibrations converted into the measurement of the deposited energy.

All the calorimeters are divided into segments or "towers" in such a way that the division boundaries between them point at the interaction point. The entire calorimetry system consists of two regions, central and forward; the later is also known as the "plug".

The central calorimeters cover the region of 2π in ϕ and as far as $|\eta| < 1.0$ in pseudorapidity. They are segmented into the "towers" of $0.11 \times 15°$ in $\eta \times \phi$. The electromagnetic (CEM [25]) part consists of alternating layers of lead absorber and polystyrene scintillator, while the hadronic part (CHA) uses thicker steel plates as the absorber. The CEM is 18 X_0 radiation lengths thick, while the CHA is 4.7 λ_I interaction lengths thick. The energy resolution of the CEM is evaluated to be:

$$\frac{\sigma_E}{E} = \frac{13.5\%}{\sqrt{E_T}} \oplus 2\% \tag{2.5}$$

The $\oplus$ notation means that the constant part is added in quadrature. The CHA resolution for

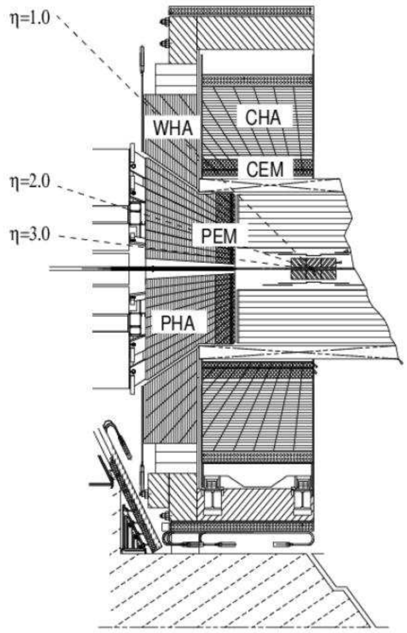

Figure 2.4: The CDF Calorimetry system.

charged pion is evaluated to be:

$$\frac{\sigma_E}{E} = \frac{50 \sim 100\%}{\sqrt{E_T}} \oplus 3\% \tag{2.6}$$

The shower-maximum (CES) and pre-shower (CPR) detectors are also a part of the calorimetry system. The CES is a gas multiwire proportional chamber with cathode strips that provide measurements of the z position and anode wires that allow a measurement of the ϕ of the energy deposition. The chamber is embedded into the CEM at about 5.9 X_0 where the maximum of electromagnetic energy deposition occurs. The position resolution in both directions is around 2 mm. The CPR consists of proportional chambers placed between the solenoid and the calorimeter. These two subsystems, CES and CPR, provide both position measurement that helps in matching energy depositions to tracks and shower profile measurement – information used in particle identification to distinguish between $e^{\pm}/\gamma$ and π^0.

The plug calorimeters [26] cover the pseudorapidity range 1.1$<|\eta|<$3.4; the general segmentation pattern is observed. The electromagnetic section (PEM) uses calcium-tin-lead alloy as an absorber and is 23 X_0 radiation lengths thick. The hadronic part (PHA) uses iron and is 6.8 λ_I interaction lengths thick. The energy resolution of the PEM is evaluated to be:

$$\frac{\sigma_E}{E} = \frac{14.4\%}{\sqrt{E_T}} \oplus 0.7\% \tag{2.7}$$

while the energy resolution of the hadronic part for charged pions:

$$\frac{\sigma_E}{E} = \frac{74\%}{\sqrt{E_T}} \oplus 4\% \tag{2.8}$$

The plug shower-maximum (PES) detector consists of strips of scintillator located at about 6 X_0 inside the PEM, providing position measurements with resolution of around 1 mm.

It should be noted that the segmentation of the calorimeters is rather large and thus it is quite possible that the energy measured by a particular tower has contribution to by multiple particles. Occasionally this poses a problem as the energies of the individual particles can not be determined. In other situations, most notably when a "jet" of particles that results from hadronization of quark or gluon coming directly from hard scattering hits the calorimeter, the measurabletotal energy of all component particles is exactly the information that is needed.

Muon Detection

Muon is 200 times heavier than electron, so it loses substantially less energy due to electromagnetic interactions as it travels through the calorimeter material. This allows the muons th pierce through the calorimetry subsystem after the exit the tracking volume. The CDF muon subsystem consists of several chambers that are located outside of the calorimeters and includes Central MUon detector (CMU) [27], Central Muon uPgrade (CMP), Central Muon eXtension (CMX) and Barrel MUon detector (BMU). The overview of the muon systems are shown in Figure 2.5 Due to space and design constraints the muon coverage is incomplete. We describe the muon coverage in detail in Section 3.3.4.

The CMU detector is built directly outside the CHA calorimeter. It covers the central region up to a pseudorapidity of $|\eta|$ <0.6. The CMU contains four radial layers of drift chambers to reconstruct the track of a muon as it passes through them.

One downside of the CMU detector is its lack of additional shielding, which makes it easier for other particles to fake a muon signal. The CMP addresses this problem by adding 60 cm thick steel (the return yoke for the solenoid magnet) to absorb other particles, improving the over all trigger efficiency when combined with the CMU. The CMP is constructed as a box rather than cylinder.

The CMX subdetector extends the coverage of the muon chambers to a pseudorapidity of 0.6< $|\eta|$ <1.0. In order to fit in the existing collision hall, the CMX was designed into pieces to provide full angular coverage: the arches, which fit in on the sides; the keystone, which sits on top of the detector; and the miniskirt, which goes beneath the detector. These three pieces provide full angular coverage. Scintillator plates are used to reject tracks that are not consistent with a muon arriving from the interaction point.

The BMU detector extends the pseudorapidity coverage to 1.0< $|\eta|$ <1.5. Drift chambers and scintillators are attached to the large cylindrical pieces of steel that are mounted around

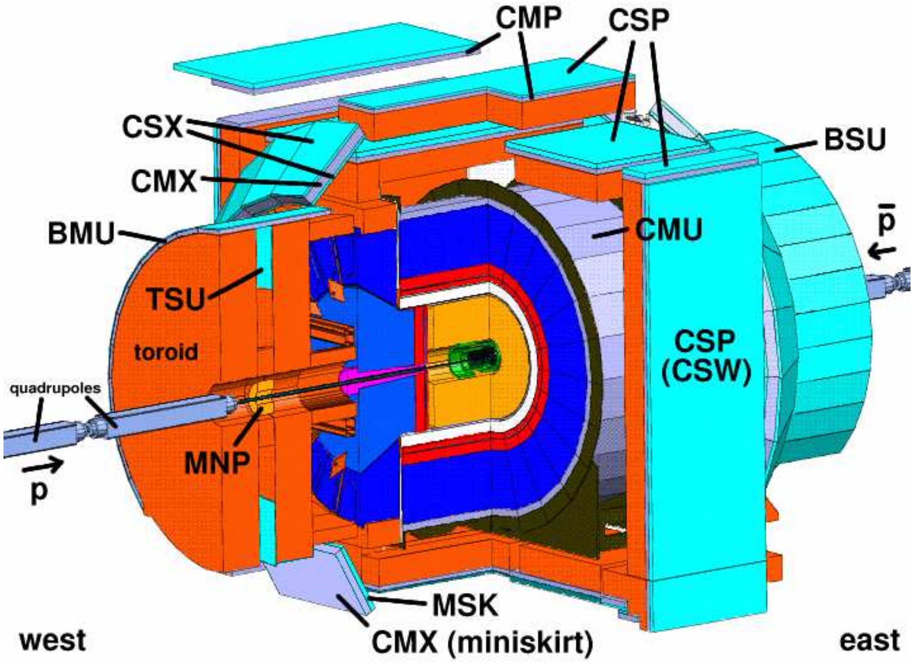

Figure 2.5: The CDF Muon system.

the endcap toroids. The steel pieces shield the electronics from beam radiation in the collision hall.

Cherenkov Luminosity Counter (CLC)

Measurement of acquired luminosity is an essential part of determining the sensitivity of the measurement and estimating the number of background events. CDF has luminosity counters CLC mounted very close to the beam line in the plug, at a pseudorapidity of $3.7< |\eta| <4.7$. The CLC is filled with Isobutane and designed to detect the burst of Cherenkov radiation that results from charged particles flying through it. The light is collected and sent to a PMT to be read out. There are three layers in the CLC, with 16 counters in each layer on each side.

2.5 Data Acquisition System

Every time bunches of protons and antiprotons collide, the data acquisition system sends a trigger to the subdetectors in the system, telling them to start reading out the data. However, with collisions occurring every 396 ns, it is impossible for every event to be recorded to disk. It is unnecessary as well; of all the events, very few are of interest to physicists. Selecting only those events of interest is the job of a fast "trigger" system [29]. This allows CDF to keep all the events we need and still operate with practically acceptable dead-time conditions.

level 1

The lowest level of trigger at CDF must make a decision within 5 μs after each collision. For collisions occurring at a rate of 1.7 MHz, the Level 1 trigger system reduces the acceptance rate to about 40 kHz. Because of the stringent time requirement, it is implemented in hardware. The Level 1 trigger can make its decision based on clusters of energy in the calorimeters (from jets or photons), muons and electrons (tracks matched to muon stubs or calorimeter clusters) or undetected energy inferred from conservation law. A system called the eXtremely Fast Tracker (XFT) [30] reconstructs tracks in the COT. A dedicated processor makes rapid decisions based on these quantities.

level 2

The next level of trigger looks into the events that passed Level 1 applying refined selection, making a decision within comparatively long 30 μs. The extra time allows it to perform more careful clustering in the calorimeter, including information from the CES and silicon. Because of the large number of readout channels, the silicon readout chips hold each event on an on-board circular buffer. They do not send the information to the data acquisition system until the event passes the Level 1 trigger.

Silicon information is processed by Silicon Vertex Tracker (SVT) [31], a system that rapidly analyzes the silicon data to look for a displaced vertex. The calculations of the different systems (calorimeter, COT, and silicon) are sent to a single computer that analyzes the data and decides whether to accept the event. The Level 2 system is asynchronous, it does not require an event to be finished within a fixed time. It reduces the rate of accepted events to about 400 Hz.

level 3

The highest level of trigger at CDF is implemented in software on a farm of several hundred computers. Each event that passes Level 2 is sent to the event builder, which assembles the disparate information into a data format readable by Level 3. Level3 fully reconstructs the event and analyzes hight-level quantities to make the final acceptance decision. Events that pass Level 3 are ready to be written to disk. Level 3 reduces the event rate to about 100 Hz.

prescales

The trigger system includes many different triggers which are used for different analyses and calibration studies. Because some triggers fire at a very high rate, it is necessary to attach a "prescale" to them to keep the overall rate acceptable. This involves rejecting a fixed fraction of the evens; for example, a trigger with a prescale of 10 keeps every tenth event which would otherwise pass.

The rate of trigger increases with the instantaneous luminosity of the collisions. Thus, as the luminosity declines, more bandwidth is available in the trigger system. It is useful to use "dynamic prescaling", which changes the prescale on the triggers as the instantaneous luminosity changes. Triggers with dynamic prescales require careful bookkeeping to properly account for the luminosity they record.

Consumer Server/Logger (CSL)

The event accepted by the trigger needs to be recorded. This is managed by the CSL [32], which categorizes events by the triggers they fired and writes them to hard disk, also providing a fraction to be used for online monitoring. The data on these disks are then copied to tape storage, ready to be processed with offline reconstruction program.

Online Monitor (Consumer)

The data are transfered from Level 3 to a CSL process which send the data to computer center where they are written to tape and forwards copies of a subset of these events to the online monitoring programs [33]. The total bandwidth available to the consumers is limited to 10 MByte/s. The Consumer Framework is written in C++ and makes heavy use of the ROOT [34] package. The Consumer Framework consist of 10 monitoring programs, display servers, display clients, an error reciever and state monitor. The online monitoring programs are permanently running in the CDF control room since April 2001. The 10 processes are distributed over 6 Linux PCs. The PCs serve 10 screens where the display clients are showing the results to check the data quality.

Chapter 3

Event Reconstruction

In the previous chapter, we discussed the experimental apparatus needed to produce and measure single top quark production events. In particular, a three tiered trigger system is required to select the events of interest. The trigger system uses a combination of hardware and software techniques to reconstruct physics objects "online". In this chapter we describe the "offline" reconstruction of physics objects by sophisticated software algorithms. We discuss tracking, calorimeter clustering, lepton identification, bottom-quark-jet identification, and luminosity calculation.

3.1 Tracking

Tracks are reconstructed using hits in the COT and silicon detectors. Two algorithms are run in parallel to reconstruct tracks: Segment Linking (SL) and Histogram Linking (HL). The SL algorithm forms track segments in each of the superlayers individually and tries to link them together, starting from the outermost superlayers. By contrast, the HL algorithm begins with a segment and the beam position which defines a nominal curvature radius. The distance between hits and the nominal road are binned in a histogram. The most populated bin indicates a potential track. Duplicate tracks from SL and HL algorithms are removed, and preference is given to the SL algorithm. Track candidates are fit to a helix, and basic quality requirements are applied. If a hit associated with a track has a residual larger than 600 microns, then the hit is dropped and the track refit again.

The final tracks used in physics analyses are determined by a wide range of algorithms. Typically tracks are formed by taking candidate COT tracks and extrapolating them into the silicon detector. Silicon hits that are within a road are added to the track. To recover forward tracks that do not traverse much of the COT, an algorithm which begins inside and extrapolates out is also performed. COT tracks with no silicon are classified as COT-only.

In general, if the silicon detector is used, these tracks must have ≥ 3 axial silicon hits. If the COT is used, ≥ 2 axial and ≥ 2 stereo superlayers must be used with ≥ 5 hits in each super-layer. Further criteria are typically imposed depending on the type of algorithm used.

The tracking algorithm has 98-99% efficiency for tracks with p_T >1 GeV/c . COT-only tracks have a transverse momentum resolution, $\sigma_{p_T}/p_T \approx 0.15\% \times p_T$. When combined with hits from the SVX and ISL, the transverse momentum resolution is $\sigma_{p_T}/p_T \approx 0.07\% \times p_T$.

3.2 Calorimeter Object

In this section, we discuss the reconstruction of calorimeter objects, specifically jet and missing transverse energy.

3.2.1 Jets

Jets are broad streams of particles resulting from quark or gluon hadronization. For this analysis, we use the jet clustering algorithm to identify jets by a fixed-cone clustering technique. The algorithm is seeded by a local maximum in the total tower energy (with at least 1 GeV of deposited energy) and considers the energy deposits in all towers in a fixed $\Delta R \leq 0.4$ cone. The algorithm recalculates the E_T-weighted center of the cluster, and reiterates over the procedure until the jet energy and its center is stable. Jets which share more than 50% of their energy are merged together.

The energy of the jet must be corrected for a variety of effects. The jet energy correction is applied according to the following relation:

$$E_T^{\mathrm{corr}} = (E_T^{\mathrm{raw}} \times f_{\mathrm{rel}} \times f_\eta \times f_{\mathrm{scale}} - E_T^{\mathrm{MB}}) \times f_{\mathrm{abs}} - E_T^{\mathrm{UE}} + E_T^{\mathrm{OC}}, \tag{3.1}$$

where correction factors are described and determined as follows:

- PMT response : The initial level of correction accounts for tower-to-tower variation and non-linearities in the PMT response to charge depositions.

- η dependence : The second level of correction adjusts for the η dependence of the detector response, which results from gaps in coverage and varying responses from the different calorimeters. This correction is determined by reconstructing "di-jet" events, which have exactly two jets in the final state. On average, the total energy of each jet should be balanced by the other, allowing the total calorimeter response to be normalized to the 0.2 $< |\eta| <$ 0.6 region.

- non-linearity correction: The third level of correction used for this analysis adjusts the jet energies to account for gaps in instrumentation and non-linearities in the total calorimeter response. This correction is extracted from Monte Carlo.

- Minimum-bias correction: The fourth level corrects for multiple interactions per beam crossing which could deposit additional energy in the calorimeters. The overall contribution is subtracted off on average, by examining minimum-bias events and parameterizing the correction as a function of number of reconstructed vertices. The systematic uncertainty of this correction is 15%. The sources of uncertainties are the differences observed with different event topologies and the luminosity dependence.

- Absolute value correction: The fifth level correction attempts to estimate the absolute energy of the parton responsible for the jet. The correction addresses the energy that escapes the cone and extra particles from the underlying event which are merged into the cone.

- Underlying event (spectator partons): The underlying event is defined as the energy associated with the spectator partons in a hard collision event. This energy needs to be subtracted from the particle-level jet energy. The underlying energy was measured from minimum bias data requiring events with only one vertex. The uncertainty of the underlying event correction is 30%.

- Out-of-Cone correction: It corrects the particle-level energy for leakage of radiation outside the clustering cone used for jet definition, bringing the “jet energy” back to the “parent parton energy”. We measure the energy flow difference between cones of size 0.4 and 1.3. Since the Monte Carlo must describe the jet shape of the data, the systematics is taken as the difference between data and Monte Carlo for different topologies.

The jet energy, corrected up to fifth level, is used for the event selection described in Chapter 5. In the other part of this analysis, we use the jet energy after all corrections applied.

3.2.2 Missing Transverse Energy

Missing transverse energy, $\not\!\!E_T$, is a signature for neutrinos and other exotic particles that do not interact with detectors. The raw value of $\overrightarrow{\not\!\!E}_T$ is calculated by summing energy deposits in the calorimeter towers, each projected on a unit vector from the beam axis to the tower:

$$\overrightarrow{\not\!\!E}_T^{\mathrm{raw}} = -\sum_i E_i \cdot \sin\theta_i \hat{n}_i, \tag{3.2}$$

where E_i is the energy of the i-th tower, $\hat{n}_i$ is the radial direction unit vector from beam axis to the tower and θ_i is polar angle pointing from z_0, z-coordinate of the event vertex, to the i-th tower. This sum extends to $\eta_{\mathrm{detector}} < 3.6$.

The value of $\overrightarrow{\not\!\!E}_T^{\mathrm{raw}}$ should be further corrected for escaping muons and jet energy mismeasurement. Muons do not deposit substantial energy in the calorimeter, but may carry out significant amount of the energy. The sum of transverse momenta of escaping muons $\sum \overrightarrow{P}_{T,\mu}$ measured in the COT has to be added to the $\overrightarrow{\not\!\!E}_T^{\text{raw}}$ with a negative sign and the energy deposited by muons in calorimeters $\sum \overrightarrow{E}_{T,\mu}$ has to be subtracted from that sum, as it has been already counted in the $\overrightarrow{\not\!\!E}_T^{\text{raw}}$.

The raw values of jet energies contributing to $\overrightarrow{\not\!\!E}_T^{\text{raw}}$ and these values have to be replaced in the sum by corrected ones (Eq. 3.1). The corrected value of $\overrightarrow{\not\!\!E}_T^{\text{corr}}$ is therefore given by the following relation:

$$\overrightarrow{\not\!\!E}_T^{\text{corr}} = \overrightarrow{\not\!\!E}_T^{\text{raw}} - (\sum \overrightarrow{P}_{T,\mu} - \sum \overrightarrow{E}_{T,\mu}) - (\sum_{\text{jets}} \overrightarrow{E}_{T,\text{jet}}^{\text{corr}} - \sum_{\text{jets}} \overrightarrow{E}_{T,\text{jet}}^{\text{raw}}) \tag{3.3}$$

where $\overrightarrow{E}_{T,\text{jet}}^{\text{corr}}$ is corrected up to sixth level, no out-of-cone correction, to avoid over correction. Uncertainties in $\overrightarrow{\not\!\!E}_T^{\text{corr}}$ are dominated by uncertainties in jet energies. Mismeasurements of $\overrightarrow{\not\!\!E}_T$ result from jets traversing through poorly instrumented regions of detectors, e.g. cracks, dead zones and beam halo effects. They may also result from cosmic rays, muon misidentification and mismeasurements in muon track momenta.

The resolution of $\not\!\!E_T$ generally depends on the total energy deposited in the event. It is parametrized in terms of the total scalar transverse energy $\sum E_T$, which is defined as

$$\sum E_T \equiv \sum_{\text{towers}} E_i \sin\theta_i \tag{3.4}$$

The $\not\!\!E_T$ resolution in the data is measured in minimum bias events, dominated by inelastic $p\bar{p}$ collisions. In minimum bias events the x and y components of $\overrightarrow{\not\!\!E}_T$ are distributed as Gaussian around zero with $\sigma_x = \sigma_y = \sigma$. The $\overrightarrow{\not\!\!E}_T$ resolution, $\sqrt{\langle \not\!\!E_T^2]\rangle}$ is then given by $\sqrt{2}\sigma$. It is expected to scale as a square root of the total transverse energy in the event $\sum E_T$ and from minimum bias studies is determined to be $\sqrt{\langle \not\!\!E_T^2 \rangle} \sim 0.64\sqrt{\langle \sum E_T \rangle}$ where energy is expressed in GeV .

3.3 Lepton Identification

In this section we discuss the identification of electrons and muons which form the basis of the "lepton+jets" dataset. The leptons are required to be consistent with those produced from W decay: high p_T and isolated.

3.3.1 Central Electrons

Central, high E_T electrons are identified by matching tracks to electromagnetic calorimeter clusters. Central electrons are selected with the following criteria:

- Fiducial to the CES and CEM: The CES and CEM (in conjunction with the trackers) are the primary means by which central electrons are distinguished from other physics objects.

- E_T >20 GeV : E_T is calculated by measuring the total EM energy deposition in a electromagnetic cluster (corrected for non-linearities and tower-to-tower variations) and multiplying by the sine of the polar angle of the associated track: $E_T = E \sin\theta$. The cluster used for this variable is a two-tower cluster, where the towers are chosen to be the closest two η-adjacent towers to the track. Since electrons emit bremsstrahlung photons easily, the energy, rather than the momentum, is typically used to characterize electrons.

- p_T >10 GeV/c : The track associated to the EM cluster is required to have transverse momentum greater than 10 GeV/c . If silicon hits are not present, the track parameters are calculated assuming that it originated from the beam line.

- ≥ 3 Axial COT SLs with ≥ 5 hits per SL and ≥ 2 Stereo COT SLs with ≥ 5 hits per SL: This ensures that the COT track is well measured.

- Track $|z_0| < 60$ cm.

- Not a conversion: Electrons that result from conversion of a photon into e^+e^- pairs are differentiated from W or Z electrons on the basis of more stringent electron selection requirements. A geometric technique is used to identify conversion electrons. The event is searched for additional oppositely-charged track to the candidate electron with $|\Delta\cos\theta| < 0.04$ and $|s| < 0.2$ cm. s is defined as the perpendicular distance between two tracks when they are parallel. If a third track forms a conversion pair with either the primary electron candidate or the conversion partner, then the event is no longer vetoed. This requirement is implemented to allow for "trident" electrons, where an electron emits a bremsstrahlung photon which is promptly converts.

- Calorimeter isolation < 0.1: The isolation used here is defined as the ratio of the total hadronic and electromagnetic energy in a cone of $\Delta R \leq 0.4$ excluding the candidate electron cluster.

- $E_{\mathrm{Had}}/E_{\mathrm{EM}} \leq 0.055{+}0.00045{\times}E(\mathrm{GeV}\ )$: This requires that the shower is mostly electromagnetic to suppress hadronic objects. The second term accounts for some leakage from the CEM when the electron is especially energetic. For this variable, a three-tower calorimeter cluster is used.

- $L_{\mathrm{shr}} \leq 0.2$: L_{shr} characterizes the lateral sharing of the electromagnetic shower among calorimeter towers. Although the Moliére radius[1] is small (~ 2 cm) for the CEM, the total content of an electromagnetic shower can spread between different CEM towers adjacent in η, particularly when the electron track is not perfectly aligned with respect to the

[1] The Moliére radius is a characteristic constant of material describing the transverse radius of an electromagnetic shower, approximately equal to 0.027 $X_0(Z + 1.2)$, where X_0 is the radiation length and Z is the atomic number of the material.

projective geometry. The value of L_{shr} is the likelihood for the sum over towers of the difference between the expected and measured energy deposits divided by the root-mean-squared uncertainty. L_{shr} uses a three-tower cluster.

- $E_{\mathrm{EM}}/P \leq 2$ unless $p_T \geq 50$ GeV/c : The total electromagnetic energy of the cluster must be consistent with the momentum of the track. Both detector resolutions, hence the ratio, are affected by bremsstrahlung can affect the ratio. Very high momentum electrons have this requirement released.

- $|\Delta_{\mathrm{strip}}| \leq 3$ cm and -3.0 $\leq Q\Delta_{\mathrm{wire}} \leq$ 1.5 cm: The distance between the track extrapolation and the center of electromagnetic cluster measured with the CES must be small. The distance is calculated in the plane of the respective detector (strip or wire).

- $\chi^2_{\mathrm{strip}} \leq 10$: The transverse profile of the electromagnetic cluster in the CES strip chamber must be consistent with an electron. The measured shape is compared to that of a beam test of 10 GeV electrons. The χ^2_{strip} value is scaled to account for variations of the profile as a function of energy and momentum.

The efficiency of these cuts is approximately 80 %, using a sample of electrons from Z decay. The ratio of the efficiency in data and Monte Carlo – *i.e.* the data-MC efficiency scale factor (SF) – is approximately 0.98. These values vary slightly with time due to varying instantaneous luminosity and detector effects.

3.3.2 Plug Electrons

There is no trigger directly made on clusters in the plug calorimeter. This is because the plug has higher background from "beam splash", particles from collision remnants which tend to have large pseudorapidity. In addition, the trigger cannot use tracking information because most of tracks that point toward the plug do not pass through enough layers of the COT to perform fast tracking. Instead, this trigger relies on the presence of large missing transverse energy from W decay in the final state to trigger events. The lack of a tracking requirement for this trigger makes it less pure, thus requiring additional selection cuts to purify the sample. Plug electrons are selected with the following criteria:

- Fiducial to the PHX and $1.2 \leq |\eta| \leq 2.8$: The PHX is candidate electron is found in the plug calorimeter fiducial region.

- E_T >20 GeV : E_T is calculated by measuring the total EM energy deposition in a electromagnetic cluster and multiplying by the sine of the polar angle of the associated track: $E_T = E \sin\theta$.

- $E_{\mathrm{Had}}/E_{\mathrm{EM}} \leq 0.05$: This requires that the shower is mostly electromagnetic and suppresses hadronic objects.

- PEM 3×3 Fit Tower > 0: Once the track has been extrapolated to the plane of the PEM shower max, the "TowerKey" is determined for the tower the track traverses. A vector of "TowerKeys" is constructed from the seed tower of the PEM electromagnetic cluster, and all its neighbors are constructed. This is generally a 3×3 tower region with the seed tower at the center. The algorithm for associating tracks in the PEM then requires that the tower traversed by the track be one of the 3×3 towers in the vector of TowerKeys.

- $\chi^2_{3\times3} \leq 10$: the electromagnetic cluster is required to have a valid $\chi^2_{3\times3}$ for comparison with the PES cluster location.

- PES $U_{5\times9} \geq 0.65$ and $V_{5\times9} \geq 0.65$: The quantities $U_{5\times9}$ and $V_{5\times9}$ are essentially isolation variables for the shower maximum detector independently applied to both u and v layers. The PES clustering is performed by ordering PES strips in decreasing energy with the highest-energy strips used as seeds. Then a fixed-width nine-strip cluster is formed from each seed. This done separately for 1D u- and v-layer clusters. The quantities $U_{5\times9}$ and $V_{5\times9}$ represent the ratio of energy sum in the central 5 strips of a PES cluster to the total energy of the PES cluster (in all 9 strips).

- Calorimeter isolation < 0.1: This variable is defined identically to the CEM electrons. The isolation used here is defined as the ratio of the total hadronic and electromagnetic energy in a cone of $\Delta R \leq 0.4$ excluding the electron cluster itself.

- $|\Delta R_{PEM}| < 3$ cm: The χ^2-fit also determines the position for the center of the shower. $|\Delta R_{PEM}|$ is the distance between the $\chi^2_{3\times3}$ best fit position and the intersection of the centroids in the u- and v- layers of PES clusters. ΔR matching requirement is also enforced between the PES coordinates and the extrapolated PHX track.

- $N^{\mathrm{Si_{hits}}} \geq 3$: To reduce higher background from beam splash, number of silicon hits $N^{\mathrm{Si_{hits}}}$ is required at least 3 hits.

- Track $|z_0| < 60$ cm.

Two samples are used to estimate the efficiency of this trigger. To measure the efficiency of the calorimeter energy requirement, a sample of Z bosons that decay to electrons is used, with one electron triggered in the central electron trigger and the other detected in the plug calorimeter. Requiring that these electrons comes from a Z boson makes this sample very pure. The average efficiency of this trigger is 88.6±0.6%.

3.3.3 Triggered Muons

The central muon trigger detects muons that reach the central muon chambers. There must be hits in both the CMU and the CMP to pass trigger (CMUP trigger). Since the CMU has a large punch-through rate, the CMP is added to suppress fake muons. The CMX subsystem requires a muon stub matched to a COT track, because it only has one set of detectors (instead of two, like the CMUP trigger) and no steel between it and the calorimeter. The CMX trigger is not as pure as the CMUP trigger. Central high p_T muons are identified by matching tracks to muon stubs. Additionally, the associated calorimeter deposition must be consistent with a minimum ionizing particle (M.I.P). Muons are selected with the following criteria:

- Fiducial to the CMU/CMP or CMX.
- $p_T > 20$ GeV/c .
- $E_{\rm EM} < 2$ GeV for $P < 100$ GeV/c and $E_{\rm EM} < 2{+}0.0115 \times (P$ - 100) GeV otherwise: The electromagnetic content of towers associated with the muon track must be small. The requirement is loosened when the muon is very high p_T to accommodate the relativistic rise of energy deposition. P is the momentum in unit of GeV/c .
- $E_{\rm Had} < 6$ GeV for $P < 100$ GeV/c and $E_{\rm Had} < 6$ GeV $+\ 0.028{\times}(P{-}100)$ GeV/c : Similarly, the hadronic content must also be small. Again, the P above is the momentum in units of GeV/c .
- Calorimeter Isolation < 0.1: The isolation defined here is the total E_T in a cone of $\Delta R \leq 0.4$ around the muon candidate divided by the transverse momentum.
- ≥ 3 Axial COT SLs with ≥ 5 hits per SL and ≥ 2 Stereo COT SLs with ≥ 5 hits per SL: This ensures that the COT track is well measured. This is the same requirement used for electrons.
- Track $|z_0| < 60$ cm.
- $|d_0| < 0.02$ (0.2) cm when the tracks use (do not use) silicon information. The impact parameter is relative to the beam line. This requirement suppresses cosmic ray muons.
- $|\Delta_x| < 7$ cm (CMU), 5 cm (CMP), 6 cm (CMX): the distance between the extrapolated track position and muon stub in the chambers must be small. Multiple scatterings and the intrinsic resolution of the chambers account for the difference.
- $\rho_{\rm COT} > 140$ cm (CMX): the exit radius of the track from the COT for CMX muons must be greater than 140 cm. This ensures that the track is well measured and in fiducial.
- Track fit $\chi^2 < 2.3$ (2.75): The χ^2 of the track fit with the COT must be good in order to suppress decays-in-flight ($e.g. K \rightarrow \mu\nu, \pi \rightarrow \mu\nu$) which contribute very high p_T fake muons. Two different values for the requirement are used in different time periods, but both are $\sim 99\%$ efficient. The χ^2 must be less than 2.3 for the first 300 pb^{-1}, and 2.75 for the rest.

Table 3.1: Event selection requirements for the missing transverse energy and jet trigger.

Event variable	Selection requirement
Level 1	
Missing E_T	> 15 GeV
Tower E threshold	> 1 GeV
Level 2	
Seed E	> 3 GeV
Tower E threshold	> 1 GeV
E_T	> 10 GeV
N_{jets}	> 2
Level 3	
Missing E_T	> 35 GeV

The muon identification efficiency, measured in a sample of $Z \rightarrow \mu^+\mu^-$, is approximately 90% and 92% for CMUP and CMX muons, respectively. The data-MC muon identification efficiency scale factor is approximately 0.98 and 1.00 for CMUP and CMX muons, respectively. These values vary slightly ($\sim 1\%$) with time. The CMX efficiency also changes slightly depending on which of arches, miniskirt, and keystone is used. The precise values and uncertainties of the efficiency and SFs for electrons and muons will be revisited in Chapter 5.1.

3.3.4 Untriggered Muons

Muon candidates tend to have fewer fake events than electrons, because they are detected for from the interaction point, have more material in front to absorb hadronic backgrounds, and require M.I.P. signal in the calorimeter. In fact, there are many muons that are not be triggered efficiently but can be recovered offline with additional selection cuts. We recovered such muons from the trigger that does not use muons. Without a track for the CMUP/CMX trigger, the easiest way to identify events is to look for their other significant features: jets and missing transverse energy. We used a trigger requiring two jets and 35 GeV of missing transverse energy. The selection requirements are summarized in Table 3.1. Events recorded by this trigger are often referred to as "extended muons" or "untriggered muons".

- Missing E_T: The missing transverse energy of the event. The requirement is lower for Level 1 because other higher-level trigger use the same Level 1 trigger.
- Tower E threshold: The energy needed in a tower to be included in the missing transverse energy calculation (Level 1) or the clustering calculation (Level 2).
- Seed E: The energy of the highest-energy tower in a calorimeter cluster.
- E_T: The transverse energy of a cluster in the calorimeter.

- N_{jets}: The number of calorimeter clusters passing all cuts.

As instantaneous luminosity at the Tevatron increased, it was necessary to modify this trigger to require that one of the jets be central, requiring $|\eta| < 1.1$. This, combined with a dynamic prescale, lowered the rate sufficiently to keep implemented in the CDF trigger.

In order to make this trigger fully efficient, additional kinematic cuts are required. Two jets with corrected transverse energy greater than 25 GeV , are required; one of the jets must be in the central region, with a $|\eta| < 0.9$; and the distance between the jets in the η-ϕ plane must be more than 1.0.

3.4 Bottom-quark Jet Identification

The majority of background events contain only light quark or gluon jets in their final states. Determining if a jet is one that originated from a bottom quark, called a b-jet, is very useful for removing backgrounds. This procedure, called "b-tagging", takes advantage of the fact that B hadrons can only decay through weak interactions and thus have a relatively long lifetime. Combined with the fact that these jets often have large transverse momentum and thus a large Lorentz boost, B hadrons travel several mm transversely before they decay.

Displaced decays are a key part of recognizing jets from bottom quarks. Here the silicon detector demonstrates its usefulness, as it has a precision to detect tracks coming from a "secondary vertex", slightly displaced from a primary vertex.

In this section we describe the performance of b-tagging algorithms, SecVtx and JetProb which are used in this analysis.

3.4.1 SecVtx Algorithm

The tagging algorithm, called "SecVtx", relies on the displacement of secondary vertices relative to the primary event vertex to identify b hadron decays [35].

In order to select displaced tracks coming from decays of long-lived hadron, precise knowledge of the collision point is necessary. To find an event-by-event primary vertex, we first identify which of the vertices is nearest to the identified high-momentum electron or muon. For other data sets without high-momentum leptons, we use the vertex which has the highest total scalar sum of transverse momentum of associated tracks. The position of the primary vertex is then determined by fitting all the tracks within a $\pm$1cm window in z around this vertex. The procedure starts by fitting a vertex using all tracks within the z window and with impact parameter significance (relative to the beam line) $|d_0/\sigma_{d_0}|$ <3, where σ_{d_0} includes the uncertainty on both the track and the beam line positions. The transverse profile of the beam line at the z of the candidate vertex is here used as a constraint in the fit. A pruning stage removes tracks which contribute $\chi^2 > 10$ to the fit (or the track with the largest χ^2 contribution if the total fit reduced chi-squared per degree of freedom $\chi^2/\mathrm{ndf} > 5$). After the initial pruning, the fit is repeated using only the remaining tracks until a vertex with no track over the χ^2 cut is found. If no tracks, survives the primary vertex position estimate. In the event sample used for the analysis the uncertainty in the fitted transverse position ranged in 10-32 μm depending upon the number of reconstructed tracks and the topology of the event.

Secondary vertex tagging is operated on a per-jet basis, where only tracks within the jet cone are considered for each jet in the event. A set of cuts involving the transverse momentum, the number of silicon hits attached to the tracks, the quality of those hits, and the χ^2/ndf of the final track fit are applied to reject poorly reconstructed tracks. Only jets with at least two of good tracks can produce a displaced track; a jet is defined as "taggable" if it has two or more good tracks. Displaced tracks in the jet are selected based on the significance of their impact parameters with respect to the primary vertex and are used as input to the SecVtx algorithm. SecVtx uses a two-pass approach to find secondary vertices. In the first pass, using tracks with $p_T > 0.5$ GeV/c and $|d_0/\sigma_{d_0}| > 2.5$, it attempts to reconstruct a secondary vertex which includes at least three tracks (at least one of the tracks must have $p_T > 1$ GeV/c). If the first pass is unsuccessful, it performs a second pass which makes tighter track requirements ($p_T > 1$ GeV/c and $|d_0/\sigma_{d_0}| > 3$) and attempts to reconstruct a two-track vertex (one track must have $p_T >$ 1.5 GeV/c).

Once a secondary vertex is found in a jet, the two-dimensional decay length of the secondary vertex L_{2D} is calculated as the projection onto the jet axis, in the r-ϕ view only, of the vector pointing from th primary vertex to the secondary vertex. The sign of L_{2D} is defined relative to the jet direction, specifically by the absolute difference $|\phi|$ between the jet axis and the secondary vertex vector (positive for $< 90°$, negative for $> 90°$). Secondary vertices corresponding to the decay of b and c hadrons are expected to have large positive L_{2D} while the secondary vertices from random mismeasured tracks are expected to be less displaced from the primary vertex. To reduce background from the false secondary vertices ("mistag"), a good secondary vertex is required to have $L_{2D}/\sigma_{L_{2D}} > 3$ (positive tag) or $L_{2D}/\sigma_{L_{2D}} < -3$ (negative tag), where $\sigma_{L_{2D}}$, the total estimated uncertainty on L_{2D} including the error on the primary vertex, is estimated vertex-by-vertex but is typically 190 μm. The negative tags are useful for calculating the false positive tag rate. A tagged jet is defined to a jet containing a good secondary vertex (the SecVtx algorithm will find at most one good vertex per jet).

While the efficiency of b-tagging is only about 40%, due to limited tracking resolution, the efficiency of tagging light quark or gluon jet is less than 1%, so the sample in b-jet content is pure.

3.4.2 Jet-probability Algorithm

The algorithm, called "JetProb", compares track impact parameters with measured resolution function in order to calculate for each jet a probability that there are no long lived particles in the jet cone. This probability is uniformly distributed between 0 and 1 for light quark or gluon jets, but is very small for jets containing displaced vertices from heavy flavor decays. We briefly describe the transformation from the track impact parameters to the Jet-probability measure.

The track impact parameter significance S is defined as the value of impact parameter d divided by its uncertainty σ_d. Tracks used in the calculation of Jet-probability are required to satisfy the quality criteria, $|d| \leq 0.15$ cm, $p_T \geq 1.5$ GeV/c and the number of SVX hits $\geq$2. The sign of the impact parameter significance is defined to be positive if the point of closest approach to the primary vertex lies in the same hemisphere as the jet direction, and negative otherwise. Signed impact parameter significance distribution fitted with four Gaussian functions $\mathcal{R}(S)$ derived using jet trigger data is used to determine the probability $P(S_0)$ that the impact parameter significance S_0 of a given track is due to the detector resolution:

$$P(S_0) = \frac{\int_{-\infty}^{-|S_0|} \mathcal{R}(S)dS}{\int_{-\infty}^{0} \mathcal{R}(S)dS}. \tag{3.5}$$

The probability that a jet is consistent with a zero lifetime hypothesis is defined as:

$$\prod \sum_{k=0}^{N-1} \frac{(-\ln \prod)^k}{k!} \tag{3.6}$$

where $\prod$ is the product of the individual probabilities $P(S_0)$ of the N_{SVX} tracks in a jet which satisfy the criteria. Jet-probability is defined using tracks with positive impact parameter and requiring $N \geq 2$. We also define a negative Jet-probability in which we select only tracks with negative impact parameter in the calculation. This is used as a control sample and a check of our method.

The positive jet-probability distribution for heavy flavor hadrons show a large excess at probabilities smaller than 0.05 over a flat distribution. JetProb tag required the Jet-probability value is smaller than 0.05.

Ideally JetProb smaller than 0.05 should contain a 5% mistag rate since the jet-probability distribution for light quarks and gluons is quite flat.

While the efficiency of JetProb tag is about 50%, the efficiency of tagging light quark or gluon jet is about 5%.

3.4.3 b-Tagging Efficiency

Unfortunately, the detector simulation based on GEANT [36] is not able to simulate all details of b-tagging – simulated Monte Carlo events typically have more tagged b-jets than the actual data. However this overestimated efficiency seems to have no kinematic dependence; it affects the rate of tagging but not the kinematic distribution of tagged events. This means that it can be compensated for with a scale factor on the tagging efficiency.

This scale factor is estimated in two different ways, one using electrons and one using muons. The electron method uses a sample of two jets, each with transverse energy larger than 15 GeV . One of them (the "away jet") is required to be tagged by the secondary vertex tagger; the other one (the electron jet) is required to contain an electron with transverse energy of at least 9 GeV . The high-momentum electron in the electron jet makes it likely that it comes from a semi-leptonic decay of the b quark. Requiring the away jet to be tagged increases the purity of the sample, since b quarks often come in pairs and double-tagged events are very rarely faked. The tagging rate of the electron jet allows an estimate of the tagging efficiency.

The electron jets can be compensated for mis-tagged light quark by looking for electron conversions in such jets; extrapolating this to the away jets gives an estimate of their heavy flavor fraction. The efficiency is then $\frac{N_+ - \alpha N_-}{N f_{\mathrm{hf}}}$, where N_+ and N_- are the number of positive and negative tags, respectively, in the electron jets; N is the total number of events; f_{hf} is the heavy flavor fraction in the away jets; and α is a mistag asymmetry factor. The ratio of this quantity in data and Monte Carlo is the scale factor.

The muon method works on the same basic principle as the electron method, requiring an 8 GeV/c muon inside one jet and requiring the other jet to be tagged. The heavy flavor fraction is determined by performing a fit to the transverse momentum distribution, using templates derived from Monte Carlo samples. This method gives a consistent result with electron method. The two are combined, resulting in the overall scale factor of 95±4% and 79±7% for the SecVtx and JetProb tagger, respectively.

The same scale factor is assumed for the tagging rate of charm quarks, which are tagged less frequently than bottom quarks but more than light quarks. Because this sample is not studied easily with the data, the systematic uncertainty on the scale factor is set twice as large.

3.4.4 Mistag

An important part of b-tagging is the accidental tagging of jets that do not contain true bottom quarks, called "mistags". Even though the fraction of mistag is very low, there are far more events with light jets than with b-jets, causing a substantial contamination in the tagged sample. Unfortunately, the detector simulation does not properly model th rate of this contribution, and unlike the true tags, the mistag rate modeling has a strong dependence on kinematic variables.

To properly understand mistag requires a "mistag matrix", which is a parameterization of the mistag rate as a function of several variables: transverse energy, the number of tracks in the jet, the sum of the transverse energies of all jets in the event, pseudorapidity, the number of reconstructed vertices in the event, and the z position of the primary vertex. Each variable is divided into four to eleven bins and used to construct a matrix of the rate of negative tags as a function of these six variables. The numbers in the matrix are calculated using a sample of generic jets.

The negative tag rate, however, is not the true rate of mistags. Some negative tags results from true b-jets whose tracks were badly reconstructed. The mistag matrix gives the negative tag probability measured in inclusive jet data, which is

$$R^{\text{negTag}} = \frac{N_{\text{light}}^{\text{negTag}} + N_{\text{heavy}}^{\text{negTag}}}{N_{\text{light}}^{\text{total}} + N_{\text{heavy}}^{\text{total}}} \tag{3.7}$$

The desired mistag rate is $\frac{N_{\text{light}}^{\text{Tag}}}{N_{\text{light}}^{\text{Total}}}$. Therefore, correction terms are needed. These are called "asymmetry" terms because they account for the difference between positive and negative tags. They are parameterized by two correction factors $\alpha = \frac{N_{\text{light}}^{\text{Tag}}}{N_{\text{light}}^{\text{negTag}} + N_{\text{heavy}}^{\text{negTag}}}$ and $\beta = \frac{N_{\text{light}}^{\text{total}} + N_{\text{heavy}}^{\text{total}}}{N_{\text{light}}^{\text{total}}}$. Physically, α corrects for the presence of negative-tagged b-jets, while β corrects for the presence of b-jets in the generic jet sample used to derive the matrix.

The parameter α is derived from a likelihood fit to the data of the invariant mass of the tracks resulting from the displaced vertex. This variable shows good separation between b, c, and light jets. Templates are generated for each type of jet and then fit to the measured distribution. To remove some difficulties with low statistics, the distribution used in the fit is the tag excess, the positive tag distribution minus negative tags. After this fit, all negative tag templates are scaled to match the observed rate, resulting in a negative tag scale factor, which is assumed to be the same for all jet flavors. After this scale factor is applied, the fit is performed again using both negative and positive tags, and this fit is used to calculate the parameter α. This parameter is also found to have a dependence on the jet's transverse energy, so it is calculated in four different regions of transverse energy.

The parameter β is derived from the same fit in the positive tag region, adjusted by the tagging efficiency and the Monte Carlo scale factor. The Monte Carlo scale factor is applied to the b and c samples equally.

An identical process is applied to the templates made in a variable called "pseudo-cτ", defined as $L_{xy}\frac{m}{p_T}$, where all terms refer to properties of the secondary vertex. This is similar to the proper decay length, but it only looks in two dimensions (hence the prefix "pseudo-"). The difference between the result obtained from this variable and the invariant mass variable is taken as a systematic uncertainty.

3.5 Luminosity Calibration

The integrated luminosity of a given data period must be accurately measured to make a precise prediction of how many events of a given process are expected. The CLC luminosity monitor can be used to estimate the integrated luminosity, which can be calculated by the equation $R_{p\bar{p}} = \mu_{\text{CLC}} \cdot f_{\text{BC}} = \sigma_{\text{inelastic}} \cdot \epsilon_{\text{CLC}} \cdot L$, where R is the collision rate, μ_{CLC} is the number of collisions per bunch crossings observed by the CLC, f_{BC} is the bunch crossing rate, $\sigma_{\text{inelastic}}$ is the inelastic proton-antiproton cross section, ϵ_{CLC} is the CLC acceptance, and L is the luminosity.

The key term μ_{CLC} is determined from the number of bunch crossing in which the CLC sees no particles:

$$\mu_{\text{CLC}} = -\ln\left(\frac{N_{\text{zeroBC}}}{N_{\text{totalBC}}}\right). \tag{3.8}$$

The estimate for the cross section is based on previous measurements from CDF [38] and the acceptance in calculated based on data and simulation studies. Uncertainties in these two quantities dominate the total uncertainty of 6% on the luminosity.

Chapter 4

Signal and Background Modeling

Each process that makes up the signal and background must be carefully modeled in the Monte Carlo simulation to describe the data as well as possible. Large samples of simulated data are created for each of signal and background processes.

4.1 s-Channel Single Top

Single top Monte Carlo sample is generated by MadEvent [39]. This generator preserves information of polarization of the top quark. Next-to-leading-order corrections change the cross section for s-channel but do not change much of its underlying kinematic distributions, so s-channel events are generated at leading order and scaled to the next-to-leading order cross section. Parton-showering, which produces jets from a parton, is modeled by the PYTHIA [41] showering routine.

4.2 t-Channel Single top

The same studies show that t-channel events change some of their kinematic distributions substantially with next-to-leading-order corrections. This is because the leading-order diagram has a b quark in the initial state (called a 2→2 process, since there are two particles in the final state) whereas one next-to-leading-order diagram starts with a gluon that splits to pair of b quarks (called a 2→3 process, since there are three particles in the final state). These two contributions predict markedly different distributions of transverse momentum of the lower momentum b quark.

To solve this problem, the t-channel sample is simulated by generating Monte Carlo events for both 2→2 and 2→3 processes using MadEvent. At generator level (before any showering or hadronization), the transverse momentum distributions of the lower-momentum b quark of these two samples are compared to a full next-to-leading-order distribution generated by the program ZTOP [40]. Adjusting their relative contribution reveals a point at which the two distributions intersect at 20 GeV . The t-channel sample is constructed by taking Monte Carlo events from the two samples in the fitted ratio, only using 2→2 events below 20 GeV and using 2→3 events above 20 GeV . This gives a continuous distribution in the transverse momentum that matches the theoretically predicted distribution. Parton-showering, which produces a jet from a parton, is modeled by the PYTHIA showering routine.

4.3 Top Pair Production and Diboson

The top pair production background and WW, WZ and ZZ processes are generated by PYTHIA [41] and normalized to the next-to-leading-order cross sections. These samples are modeled well in PYTHIA.

4.4 W+jets

The largest background to deal with comes from W+jets production. Even at tree level (with no loops or renormalization calculation added), this background is described by huge amount of possible Feynman diagrams which describe the color and kinematic characteristics of the radiated gluons. ALPGEN [42] is used to generate these events because it properly calculates all tree level matrix elements with full color and spin correlation information. The generated events are passed to the PYTHIA showering routine.

Parton-jet Matching

The PYTHIA showering algorithm gives rise to a difficulty when used with ALPGEN because there is an overlap in their generation of events. ALPGEN generates events at the matrix element level including initial- and final-state radiations, while PYTHIA approximates the effects of radiation by parton showering. PYTHIA performs showering of the parton ALPGEN generated, but without knowing whether the partion has radiated or not. ALPGEN might produce a diagram with a W boson and two radiated gluons, or it could produce a diagram with a W boson and one radiated gluon, while PYTHIA adds another gluon through parton showering. Because both of these cases can occur to the same parton, these events will appear with too large a rate.

The solution to this is a method usually referred to as "MLM matching" (for its inventor, Michelangelo L. Mangano). In this method, after parton showering, the final-state particles are grouped into jets by a jet-cone clustering algorithm, which groups all particles within a certain region of η-ϕ space. Each jet is then matched to a parton – a jet and a parton are associated if the parton lies within the cone of the jet. Only one parton can be matched to each jet. An event is rejected if it cannot match every parton to a jet. To get the counting right, the number of jets is required to be the same as the number of partons. Exclusive samples are generated with different numbers of jets, then added together after matching is performed. This removes double-counting in the showering .

Heavy flavor overlap removal

There is another issue of double-counting when using PYTHIA with ALPGEN, and it involves quarks with non-trivial masses usually referred to as "heavy flavor": charm and bottom quarks. It is important to separate events with these quarks because their kinematic behavior is different from the lighter quarks. However, they can arise in two different ways: they can be created at the matrix-element level in a $W+b\bar{b}$ event, or they can arise from gluon splitting in the parton shower from a W+light flavor event. Because there is no difference between these two cases (they have the same Feynman diagram), combining ALPGEN and PYTHIA will overestimate the heavy flavor rate by counting the same events in both W +bb and W+light flavor samples.

One consequence of this matching is that it is not possible to distinguish between an event with a W+light jet that radiates a gluon that decays into bottom quarks and a $W+b\bar{b}$ event that radiates a gluon that decays in to light quarks, because they represent the same Feynman diagram. However, separating the light quarks from the bottom quarks is useful, since $W+b\bar{b}$ is a much more significant background process than W+light jets. Since it is not possible to split the sample based on the underlying process from which the events came, the W+bottom sample is defined as any W+jets event in which one jet falls within 0.4 in η-ϕ space of a bottom quark. Any remaining event which has a charm quark that falls this distance from a jet is classified as a W+charm event, and all remaining events are classified as W+light flavor.

Mistags

Modeling the contribution of W+light jet events that are nonetheless b-tagged, called "mistag" sample, is difficult. Indeed, the Monte Carlo simulation does a good modeling of predicting general W+jet kinematic shapes, but does not model some events well which are more kinematically disposed leeding to mistagging. Therefore, the W+light flavor Monte Carlo sample is not tried to tag directly; rather, the tagging requirement is relaxed to require only one tagged jet, and each event is weighted by the product of the mistag probabilities of its taggable jets. This results in a kinematic distribution that closely models the kinematic shapes of the mistag sample.

Because events with one and two tagged jets are treated separately, it is necessary to have a different mistag models in each region. The single-tagged model is constructed as described above; the double-tagged sample uses only events with two taggable jets, both weighted by their mistag probability.

4.5 Z+jets

The Z+jets process has the same difficulties as W+jets and is generated by ALPGEN in the same way. Its contribution to this analysis is small, because one of the leptoninc decay products of the Z boson must remain undetected and generate sufficient missing transverse energy. We did not separat the quark flavors as done for the W+jet sample, since the extra discrimination is not needed.

4.6 QCD Multijets

The most difficult events to model come from QCD multijet events, called "non$W$" since there is no W bosons in the final-state. The extremely large cross section of QCD multijet events means that even kinemtatically unlikely configurations can contribute as a significant background. In particular, the conspiracy of improbable events needed to fake the necessary signature – a three-jet event in which one jet manages to pass all lepton cuts and, simultaneously, the energies are so badly measured that a large missing transverse energy is reported – still occurs frequently to contaminate the sample significantly. Because of the extremely small probability of these events to pass, and because they come from various QCD processes, all of them being difficult to calculate or model, it is impossible to simulate these events with Monte Carlo simulation.

Because these events can not be simulated, the models are derived from the data samples. This is complicated as well, because different lepton types may have vastly different rates and shapes of QCD multijet events, and each needs to be examined separately. This analysis uses two different models for QCD multijet events and one model is used for the QCD multijet modeling uncertainty estimation. All of them are based on the principle that QCD multijet events must contain a jet that is falsely identified as a lepton. Thus, by looking at jets with relaxed electron cuts it is possible to create a model of this background.

Anti-electron

Since the modeling of QCD multijet events can not be estimated from a Monte Carlo simulation, the same trigger data sample is used for the central and plug electrons. The strategy, called "anti-electron", identifies electron cuts which depend on the kinematic properties of the event, such as transverse momentum, and others which rely only on detector effects, such as the fraction of energy deposited in the hadronic calorimeter. Five such "non-kinematic" cuts are identified: $E_{\rm had}/E_{\rm EM}$, $\chi^2_{\rm strip}$, $L_{\rm shr}$, $Q \times \Delta_{\rm wire}$, and $|\Delta_{\rm strip}|$ for central electrons, $E_{\rm had}/E_{\rm EM}$, PES $U_{5\times9}$, $V_{5\times9}$, PEM 3×3 Fit Tower and $\chi^2_{3\times3}$ for plug electrons, as described in 3.3.1 and 3.3.2, respectively. These variables are designed primarily to reject fake electrons but do not greatly affect the kinematic properties of the event. Thus a QCD multijet model is constructed using events which fail at least two of the non-kinematic cuts but pass all kinematic cuts. Such fake electrons are chosen as the candidate, and the rest of the event selection cuts are applied.

Because these events are similar to the electrons with some selection cuts inverted, they are given the unfortunate misnomer anti-electrons. Their advantage is their good match with kinematic variables, especially missing transverse energy. In addition, since plug electron, PHX, trigger requires large missing transverse energy, trigger turn-on described in 5.1 has to be applied if different trigger is used.

In this analysis anti-electron QCD modeling is used for the CEM, PHX, CMUP and CMX trigger data but untriggered muons.

Non-isolated events

While the anti-electrons do a good modeling of the QCD multijet contribution to the missing transverse energy spectrum for triggered muons, they do a poor modeling of the untriggered muon sample, since these muons are kinematically distorted by their trigger. For this sample a better model is obtained by using "non-isolated" events, events which pass all selection criteria except the requirement of lepton isolation. This is based on the rationale that non-isolated events are typically leptons contained in jets, and jets that contain energetic leptons are more likely to pass lepton identification cuts. This sample has the advantage of a large size; it is not used for the other triggers because it does not properly model key kinematic distributions, such as missing transverse energy. However in the untriggered muon sample it does a good modeling, probably because of the trigger requirements of jet separation and high missing transverse energy.

Jet-electron

Another strategy for studying this sample uses a sample of generic jets, triggered through a generic jet trigger which simply looks for clusters of energy in the calorimeter. Since We are interested in QCD multijet events where a jet is falsely identified as an electron, this sample is examined for jets that look similar to the electrons. Specifically, they must be energetic, having a transverse energy of at least 20 GeV ; they must have a high fraction of energy deposited in the electromagnetic calorimeter, between 80% and 95%; and they must have fewer than four tracks, since a true electron has only single track.

This jet is then assumed to be an electron and all the other event selection cuts are applied. Because jets have multiple tracks and the charge of individual tracks can not always be determined, the charge of jet is assigned randomly. Because they come from generic jets faking electrons, these events are referred as "jet-electron". They do not fit all kinematic variables well. So jet-electron modeling is used as a cross check for the anti-electron modeling, and the difference between jet-electron and anti-electron is assigned as the systematic uncertainty in the shape.

Chapter 5

Event Selection

5.1 Trigger

The first step of the analysis is to choose a trigger to examine. The CDF data is written out along a variety of "trigger paths", and choosing the right triggers is a for this analysis to maximize the sensitivity to the sigmal. Because the signal has one charged lepton in the final state, it is sensible to trigger on leptons. In this analysis, we use two kinds of electron triggers, one for electrons detected in the central calorimeter and the other in the plug calorimeter; two kinds of muon triggers, one for the CMU and CMP detectors and the other for the CMX detector; and a missing transverse energy trigger to increase the acceptance of muons. Each trigger is a composite of the three levels trigger system (see Section 2.5).

The triggers, while very efficient, will not trigger that it ought to. Thus, we must estimate each trigger efficiency to properly predict the rate of each physics process. The basic approach to this is to examine a sample obtained through a different trigger, apply the trigger selection cuts, and see how often such events are actually accepted. The method for deriving this efficiency is presented in Section 3.3. Trigger efficiency is summarized in Table 5.1.

Because some triggers have prescales for some periods, and some have not been active for as long as others, the collected luminosity is different for each trigger. The luminosity is summarized in Table 5.1.

Trigger Turn-on function

Because offline missing transverse energy calculation includes energy from the muon and mis-measurement of jet energy, it can be different from the calculation used in the trigger. Thus, the Monte Carlo simulation needs to be adjusted accounting a turn-on function of the missing transverse energy for the trigger requiring corrected missing transverse energy with PHX and

Table 5.1: Trigger efficiency and integrated luminosity recorded for each trigger.

Trigger	Efficiency(%)	Integrated luminosity(pb^{-1})
CEM trigger	96.5±0.4	2676±160
PHX trigger	94.6±0.3	2676±160
CMUP trigger	91.5±0.5	2676±160
CMX trigger	95.3±0.7	2622±157
$\not\!\!E_T$ +jets trigger	100	2541±152

extended muon.

For the PHX, using W sample triggered with only calorimeter energy requirement, this function is modeled as $\epsilon(x) = \frac{1}{1+e^{-\beta(x-\alpha)}}$. Because additional corrections are applied to plug energy measurements in offline processing which are not included in the Level 2 and 3 trigger calculation, the turn-on curve needs additional corrections. The corrections are given in the same way as the missing transverse energy curve and the parameters are derived to match the electron energy in this sample. The resulting formula is following:

$$\sum_{\text{period}i} f_i \cdot \frac{1}{1+e^{-\beta_1^i(\not\!\!E_T^{\text{raw}}-\alpha_1^i)}} \cdot \frac{1}{1+e^{-\beta_2^i(E_T^{\text{ele}}-\alpha_2^i)}} \cdot \frac{1}{1+e^{-\beta_3^i(E_T^{\text{ele}}-\alpha_3^i)}} \tag{5.1}$$

where f_i is the luminosity fraction of period i. α_l^i and β_l^i are turn-on parameters for the Level l trigger. Level 2 trigger parameters depend on the η_{lep} region.

The trigger turn-on for the extended muon, jets and missing transverse energy trigger, is similar to that for the PHX electron trigger. The turn-on is measured in events trigged by the CMUP muon trigger, comparing the number of events which passed a cut on offline missing transverse energy with the number of events that actually passed this trigger.

5.2 Lepton selection

Once event is selected by a trigger, it must be reprocessed in offline. The offline selection identifies a high p_T lepton in the event. It is not necessary for these events to pass high p_T lepton selection described in Section 3.3, since the basic lepton selection cuts made by the trigger still leave a large number of fake leptons. Some triggers have no lepton requirement at all. Good lepton identification is vital to purify the sample by removing fake leptons, making it easier to understand and estimate the background against the single top signal. The scale factor accounting for lepton identification efficiency disagreement between the data and Monte Carlo simulation is multiplied to the acceptance of Monte Carlo background simulation. The scale factors are summarized in Table 5.2.

Table 5.2: Scale factors, the number of data divided by that estimated by Monte Carlo simulation, for different lepton selections.

lepton type	**Scale factor**
Central electrons (CEM)	0.978±0.005
Plug electrons (PHX)	0.933±0.008
Central muons (CMUP)	0.926±0.007
Central muon extended (CMX)	0.991±0.007
Untriggered muons	0.950±0.005

Table 5.3: The jet multiplicity distribution in parcent in the s- and t-channel single top quark production.

sample	**0 jet**	**1 jet**	**2 jet**	**3 jet**	**4 jet**	**≥5 jet**
s-channel	1	14	46	29	8	2
t-channel	1	18	47	26	6	1

5.3 Jet Multiplicity Selection

As the second offline selection, jets are identified by the jet reconstruction algorithm described in Section 3.2.1. The distribution of jet multiplicity in single top production events before any selection cuts is show in Table 5.3. This analysis examines events with two or three jets. Events with only one jet have a very large background from W+jets processes that make them less useful for this analysis.

5.4 Missing Transverse Energy

To remove a large amount of QCD multijet background processes, a large missing transverse energy described in Section 3.2.2 is required. The efficiency of this requirement is 83% that without including the trigger turn-on fraction.

5.5 Event Veto

Several additional selections are required to remove specific backgrounds. Each of these vetoes removes a large portion of a specific background to improve the purity of the final sample. This analysis removes events with a primary vertex too far from the center of the detector. Additional vetoes take care of events from cosmic rays, photon conversions, Z bosons, processes with two leptons, and QCD multijet processes.

Primary Vertex Requirement

For all leptons, the z coordinate of the reconstructed vertex of the track must be less than 60 cm from center of the detector. This requires the tracks to come from a hard scattering process and not elastic scattering or cosmic rays. This affects the luminosity calculation because some true hard scattering events occur outside this region. Measurements with data, using trigger on events with hits in the CLC, show that the luminosity should be scaled by 96.4$\pm$0.4%.

Cosmic Ray Veto

Muons coming from decays of cosmic-ray pions in the upper atmosphere pass through the detector frequently. Because these are true muons, passing the muon identification requirements, they need to be identified and removed. This requires a series of additional cuts. Because most cosmic-ray muons pass through the detector from the top to the bottom, they often show up as back-to-back tracks. The impact parameters d_0 of the tracks are essentially identical because they come from the same particle. This is most easily seen in the polar coordinate (ρ,β), where $\rho = \sqrt{d_{0_1}^2 + d_{0_2}^2}$ and $\tan\beta = \frac{d_{0_1}}{d_{0_2}}$. The cosmic ray tracks have impact parameters that are very similar but have a large angle between them. This analysis rejects events with $|\rho| > 0.2$ cm, $|\beta - \frac{3\pi}{4}| > 0.2$, and $|\beta - \frac{7\pi}{4}| > 0.2$.

Because the timing of a cosmic ray track with respect to bunch crossing is different from that of a track from a hard scattering event and often only one track reconstructed because the other fails the timing requirement for a COT track. Such track can be recovered by a dedicated algorithm which fits the COT hits and timing information under four different assumptions: the particle associated with the top or the bottom track can be traveling either inward or outward. If the best fit is to the case of the top track heading inward and the bottom heading outward (the signature of a downward-going cosmic ray muon), and if the fit χ^2 is less than 300, the event is removed.

Cosmic rays also unlikely pass near a reconstructed vertex. If the weighted mean of z position of the vertices in an event is more than 4 cm from the average z_0 position of the tracks, the event is removed.

The TOF timing system can also distinguish cosmic rays by comparing the times of flight of the two tracks. Since the distance between top TOF hit and bottom TOF hit is about 3 m, it takes 10 ns at the speed of light. So if the bottom track's time of arrival is more than 5 ns after the top track, the event is identified as a cosmic ray and removed.

The hadronic calorimeter TDC timing system is also used to identify cosmic-ray events, though its resolution is not as good as the TOF's. If the difference in time between the top and bottom clusters is more than 20 ns, the event is removed. This cut is tightened to 10 ns if two muon stubs are detected and the difference in polar angle between them is more than 3 radians.

These cuts cause a reduction in true hard-scattering events of about 1.5% in the muon sample, and leave behind at most 3% cosmic background contamination in the inclusive W sample, most of which is easily removed by other selection cuts. This veto is only applied to the data because cosmic ray events are not included in the Monte Carlo simulation.

Photon Conversion

Electrons that result from conversion of a photon into e^+e^- pairs, which is described in Section 3.3.1, are removed.

Z Boson Veto

Z bosons form a significant background in the conditions where a Z boson decays to two leptons, with one lepton escaped from being detected, and mismeasured jets result in sufficient missing transverse energy to pass the missing transverse energy requirement. The Z boson veto looks for additional loosely identified lepton (including a high-momentum track with no other tracks nearby) with the opposite charge to the identified tight lepton. If the invariant mass of the two falls in the Z boson mass (76-106 GeV/c^2), the event is rejected. This leaves a few persent of residual contamination from Z+jets events.

Dilepton Veto

One major background is top pair production in which both final-state W bosons decay to leptons. If one of the leptons is ignored, the signature is the same as a single top event. This background can be greatly reduced by removing any events with more than one lepton. This veto looks for any leptons, including loose leptons, in an event, and rejects the event if there is more than one lepton.

Because leptonically decaying top pair events have two true leptons in their final state, they require a special scale factor to account for the difference between data and simulation in the rate of misidentifying one lepton. This can be calculated by measuring the rates of identification of all possible pairs of leptons and calculating a combined dilepton veto scale factor, which is 1.08±0.02. This is applied only to the top pair production Monte Carlo simulation events with two leptonic decays.

5.6 PHX QCD Multijet Veto

The events triggered by PHX electron have huge amount of QCD multijet events. In addition, the distribution of the angle between the direction of lepton momentum and the direction of missing transverse momentum, which is modeled by the anti-electron QCD multijet, is not perfect, especially in the region of low W transverse mass, M_{WT}. Further mismodeling is seen for the high lepton η events, typically $|\eta| \geq 1.6$. Thus we apply the additional selection of $M_{WT} \geq 20$ GeV/c^2 and $|\eta| < 1.6$ for the PHX electron trigger events to remove QCD multijet.

5.7 *b*-Tagging

As described in Section 3.4, *b*-tagging is a very useful requirement to reduce backgrounds which have light quark or gluon jets. At least one SecVtx *b*-tagged jet is required for *t*-channel single top production events, since about 94% of the *t*-channel single top signal have one *b* quark jet. Because most of *s*-channel single top signal have two *b* quark jets, at least two *b*-tags is required for *s*-channel single top search. Two SecVtx *b*-tag efficiency, however, is too small, so the events with at least one JetProb *b*-tagged jet and exact one SecVtx *b*-tagged jet are additionally used for the *s*-channel optimized analysis.

Chapter 6

Background Estimation

Estimating the background contributions after applying the event selection to the single top candidate sample is an elaborate process. NLO calculations exist for the diboson and $t\bar{t}$ production cross section, thereby making the estimation of their contributions is a relatively straightforward process. The main background contributions are from $W + b\bar{b}$, $W + c\bar{c}$ and $W + c$+jets, as well as mis-tagged $W+$ light quark jets. We determine the W+jets normalization from the data and estimate the fraction of the background events with heavy-flavor jets using ALPGEN Monte Carlo sample [42].

In this chapter, the method to estimate the composition of background processes in lepton plus b-tagged jets data sample is described. At the first step of this method we assume the composition of the sample – meaning we assume we know of all the process contributions to data. From this assumption we calculate the normalization of processes sequentially, based on the normalization of each type of process to the previous one. Because the Monte Carlo simulation is not a perfect model for some samples, this method relies heavily on data.

6.1 Signal expectation and MC Based Background Estimation

Several top and electroweak processes contribute to the lepton plus jets sample. They are the single top, the top pair production and WW, WZ, ZZ, Z+jets processes. They exist in this sample because each process can produce a real lepton and neutrino, as well as a number of jets. The yields in these sample but Z+jets are estimated using the theoretical cross sections [43], the luminosity of the sample, trigger efficiency, and an overall selection efficiency derived from Monte Carlo simulation of the processes corrected for the differences between data and Monte Carlo simulation. Z+jets cross section measurement [44] is used the cross section for the Z+jets background. The theoretical cross sections for these processes are shown in Table 6.1.

The calculated yield in these sample is given by

$$N_{\text{sample}}^{\text{predict}} = \sigma_{\text{sample}}^{\text{theory}} \cdot \epsilon_{\text{BR}} \cdot \epsilon_{\text{evt}} \cdot \mathcal{L}_{\text{int}} \tag{6.1}$$

Table 6.1: Theoretical cross sections for the signal and MC-Based Backgrounds. Z+jets is the measured cross section at CDF.

WW	12.4 ± 0.25 pb
WZ	3.96 ± 0.06 pb
ZZ	1.58 ± 0.05 pb
$Z + LF$	780 ± 84 pb
$Z + bb$	2.87 ± 0.31 pb
$Z + cc$	4.78 ± 0.51 pb
$t\bar{t}$	6.7 ± 0.8 pb
s channel	0.88 ± 0.11 pb
t channel	1.98 ± 0.25 pb

where $\sigma^{\mathrm{theory}}_{\mathrm{sample}}$ is the theoretical cross section listed in Table 6.1. ϵ_{BR} is the branching ratio 0.324 that W decays into leptons: $W \to e/\mu/\tau + \nu$. $\mathcal{L}_{\mathrm{int}}$ is the integrated luminosity shown in Table 5.1. The event detection efficiency ϵ_{evt} can be decomposed into five factors:

$$\epsilon_{\mathrm{evt}} = \epsilon_{\mathrm{acc}} \cdot \epsilon_{\mathrm{trig}} \cdot \frac{\epsilon^{\mathrm{data}}_{\mathrm{z0}}}{\epsilon^{\mathrm{MC}}_{\mathrm{z0}}} \cdot \frac{\epsilon^{\mathrm{data}}_{\mathrm{lepid}}}{\epsilon^{\mathrm{MC}}_{\mathrm{lepid}}} \cdot \frac{\epsilon^{\mathrm{data}}_{\mathrm{tag}}}{\epsilon^{\mathrm{MC}}_{\mathrm{tag}}} \tag{6.2}$$

where ϵ_{acc} is the acceptance with all selection cuts applied, as described in Chapter 5, $\frac{\epsilon^{\mathrm{data}}_{\mathrm{z0}}}{\epsilon^{\mathrm{MC}}_{\mathrm{z0}}}$ is the z_0 selection scale factor described in Section 5.5, $\frac{\epsilon^{\mathrm{data}}_{\mathrm{lepid}}}{\epsilon^{\mathrm{MC}}_{\mathrm{lepid}}}$ is the scale factor of the lepton identification efficiency listed in Table 5.2, $\frac{\epsilon^{\mathrm{data}}_{\mathrm{tag}}}{\epsilon^{\mathrm{MC}}_{\mathrm{tag}}}$ is the scale factor for the b-tagging detailed in Section 5.7.

6.2 QCD Multijet and W+jets Background Estimation

To determine the fraction of QCD multijet, called "non-W fraction", in both the pretag sample, to which b-tagging is not applied, and the b-tagged sample, we fit the $\not\!\!E_T$ distribution of data to a sum of the QCD multijet template, other background templates and the MC signal template.

$\not\!\!E_T$ Fit in the Pretag Sample

The pretag non-W fraction is essential to this method, since it provides the starting point for the "heavy flavor fraction" and "mistag rate estimate". To perform the fit in the pretag sample, we take the $\not\!\!E_T$ distribution. As the QCD multijet template, we use the template described in Section 4.6. As the other background templates, we use the full background prediction except for QCD multijet with proper normalization for the Monte Carlo based background. Here, the normalization of W+jets background sample is not used.

The $\not\!\!E_T$ distribution for the isolated pretag data events is fitted to a sum of the QCD multijet and W+jets templates using a binned likelihood fitter. Once the fraction is calculated, the normalization factor is simply given by:

$$N_{\mathrm{QCD}}^{\mathrm{pretag}} = F_{\mathrm{QCD}}^{\mathrm{pretag}} \cdot N_{\mathrm{pretag}} \tag{6.3}$$

where $N_{\mathrm{QCD}}^{\mathrm{pretag}}$ is the number of pretag QCD multijet events, $F_{\mathrm{QCD}}^{\mathrm{pretag}}$ is the non-W fraction and N_{pretag} is the number of pretag data.

The number of pretag W+jets events is estimated :

$$N_{W+\mathrm{Jets}}^{\mathrm{pretag}} = N_{\mathrm{pretag}} \cdot (1 - F_{\mathrm{QCD}}^{\mathrm{pretag}}) - N_{\mathrm{MC}}^{\mathrm{pretag}} \tag{6.4}$$

where $N_{\mathrm{MC}}^{\mathrm{pretag}}$ is the number of Monte Carlo based background events obtained from theoretical cross sections shown in Table 6.1.

$\not\!\!E_T$ Fit in the Tagged Sample

The number of QCD multijet events in the b-tagged sample was found to be equal to the number of predicted QCD multijet pretag events multiplied by the positive tagging rates described in Section 3.4.1. We measure the non-W fraction directly in the tagged sample. As the other background templates, we use our full background prediction with proper normalizations excluding the QCD multijet background.

At first we estimate W+heavy flavor jet background and W+light flavor jet (mistag) background. The number of W+jets events after applying b-tagging is estimated as follows:

$$N_{W+\mathrm{HF}}^{\mathrm{tag}} = \{N_{\mathrm{pretag}} \cdot (1 - F_{\mathrm{QCD}}^{\mathrm{pretag}}) - N_{\mathrm{MC}}^{\mathrm{pretag}}\} \cdot F_{\mathrm{HF}} \cdot K_{\mathrm{HF}} \cdot \epsilon_{\mathrm{tag}} \tag{6.5}$$

We determine the W+jets normalization factor from the data using Eq. 6.4 and then estimate the fraction of the candidate events with heavy-flavor jets, F_{HF}, using ALPGEN Monte Carlo simulation. K_{HF} is a correction factor of the Monte Carlo estimation using real data which was obtained as follows: The heavy-flavor fraction, K_{HF}, were calibrated in the b-tagged W+1jet sample using data distributions which are sensitive to distinguish light-flavor from heavy-flavor jets, e.g. the invariant mass of the secondary-vertex tracks and, more sophisticated, the output of the Neural Network jet-flavor separator. Based on these studies, the heavy flavor content was corrected by a factor of K_{HF}=1.44±0.4. ϵ_{tag} is the b-tagging efficiency.

The largest background in our b-tagged lepton plus jets sample is a set of processes containing no b quarks at all, called "W+light flavor jets" where a real W boson provides a lepton and a neutrino, and light quarks or gluons producing two or more high energy jets. A secondary vertex is reconstructed wrong when poorly reconstructed tracks crossing each other near the $p\bar{p}$ collision point. A secondary vertex that does not originate from heavy flavor quarks is called "mistags".

To estimate the mistag background we use the mistag matrix described in Section 3.4.4. The number of W+jets events in W+light flavor jets is estimated as follows:

$$N_{W+\mathrm{LF}}^{\mathrm{tag}} = \{N_{\mathrm{pretag}} \cdot (1 - F_{\mathrm{QCD}}^{\mathrm{pretag}}) - N_{\mathrm{MC}}^{\mathrm{pretag}} - N_{W+\mathrm{HF}}^{\mathrm{pretag}}\} \cdot \frac{N_{-}}{N_{\mathrm{pretag}}} \tag{6.6}$$

The predicted amount of all background events estimated with Monte Carlo simulation is subtracted from the total pretag sample to estimate the W+light flavor fraction. The predicted number of mistagged W+light flavor events is the number of mistag events in the pretag sample, N_{-} multiplied by the $W+$ light flavor fraction.

The $\not\!\!E_T$ distribution of b-tagged jet events are fitted to a sum of the QCD multijet templates and other fixed background templates using a binned likelihood fitter. Once the fraction F_{QCD} is calculated, the number of QCD multijet events after b-tagging is given by:

$$N_{\mathrm{QCD}}^{\mathrm{tag}} = F_{\mathrm{QCD}}^{\mathrm{tag}} \cdot N_{\mathrm{tag}} \tag{6.7}$$

6.3 Event Yield Prediction

Table 6.2 shows the final signal and background estimate shown separately for two and three jet samples. The uncertainties on the estimates include the systematic uncertainty on the mistag matrix, the heavy flavor k-factor, the QCD multijet estimate, the b-tagging scale factor, the lepton identification efficiency scale factor, the primary vertex position scale factor, and the trigger efficiency. In the case of Monte Carlo based estimates, they also include the uncertainty on the luminosity and the theoretical cross sections.

Table 6.2: The expected and observed number of events for 2.7 fb^{-1} of CDF data. The number of observed events is consistent with the signal plus background prediction.

CDF Run II Preliminary, L=2.7 fb^{-1}

Process	2jets	3jets
single top s-channel	19.0 ± 3.3	7.0 ± 1.2
single top t-channel	4.3 ± 0.8	5.7 ± 1.0
WW	1.6 ± 0.2	1.4 ± 0.2
WZ	7.0 ± 0.9	2.3 ± 0.3
ZZ	0.2 ± 0.0	0.1 ± 0.0
$t\bar{t}$	56.0 ± 9.7	174.6 ± 30.2
Z+jets	3.4 ± 0.7	2.6 ± 0.5
Z+bottom	2.7 ± 0.5	1.9 ± 0.3
Z+charm	0.3 ± 0.1	0.3 ± 0.1
W+bottom	119.0 ± 37.7	46.5 ± 14.6
W+charm	30.4 ± 9.5	15.0 ± 4.7
Mistags	30.7 ± 8.5	25.2 ± 6.0
QCD multijet	19.2 ± 15.3	19.3 ± 15.4
Total Prediction	294.0 ± 52.2	301.9 ± 41.1
Events observed	279.0	300.0

Chapter 7

Optimized Search for s-Channel Single Top Production

The expected single top signal rate is substantially smaller than the systematic uncertainty of the estimated background rate, as shown in Table 6.2. This means that it is impossible to obtain a significant result by simply counting the events. A more sophisticated approach is needed. The likelihood discriminant is used to improve the signal-to-background ratio in this analysis. In this chapter, the likelihood discriminant method is described.

7.1 Kinematic Solver

The top quark mass is a significant variable to discriminate between signal and background, since a top quark has very large mass, about 172 GeV/c^2 .

There are, however, two ambiguities in calculating the reconstructed $M_{l\nu b}$, which corresponds to the top quark mass. One comes from the uncertainty on assigning a b-jet correctly to the b-jet from top quark decay. The other is the neutrino energy. The transverse energy of the neutrino can be measured indirectly as the missing transverse energy, but neutrino momentum z-component $p_z(\nu)$ can not be measured. The purpose of the kinematics fitter is to evaluate the neutrino momentum and find the right b-jet assignment.

Neutrino Momentum z-Component

Neutrino momentum z-component can be calculated by solving the quadratic equation using a W mass constraint and the missing transverse energy. Since we have two solutions in general, we construct two types of likelihood-based kinematics fitters for the two solutions case and the other case. We minimize the negative log likelihood value by varying three parameters, p_z^ν, $\not{E}_x$ and $\not{E}_y$, using MINUIT [46] program.

We used the following likelihood :

Two solutions case

$$\mathcal{L}_{(p_z^\nu, \not{E}_x, \not{E}_y)} = \mathcal{L}_{p_z^\nu Q} \times \mathcal{L}_{M_{W^*}} \times \mathcal{L}_W \times \mathcal{L}_{\not{E}_x} \times \mathcal{L}_{\not{E}_y} \tag{7.1}$$

No (or one) solution case

$$\mathcal{L}_{(p_z^\nu, \not{E}_x, \not{E}_y)} = \mathcal{L}_W \times \mathcal{L}_{\not{E}_x} \times \mathcal{L}_{\not{E}_y} \times \mathcal{L}_{sol} \tag{7.2}$$

where,

$$\mathcal{L}_{p_z^\nu Q} = \frac{P^{corr}_{p_z^\nu Q}}{P^{wrong}_{p_z^\nu Q}}, \quad \mathcal{L}_{M_{W^*}} = \frac{P^{corr}_{M_{W^*}}}{P^{wrong}_{M_{W^*}}}, \quad \mathcal{L}_W = \frac{1}{\Delta M_W^2 + \Gamma_W^2}, \quad -2\log \mathcal{L}_{sol} = Im(P_z^\nu)^2$$

$$\mathcal{L}_{\not{E}_x} = \alpha \cdot e^{-\frac{(\Delta \not{E}_x)^2}{2\sigma_1^2}} + \beta \cdot e^{-\frac{(\Delta \not{E}_x)^2}{2\sigma_2^2}}, \quad \mathcal{L}_{\not{E}_y} = \alpha \cdot e^{-\frac{(\Delta \not{E}_y)^2}{2\sigma_1^2}} + \beta \cdot e^{-\frac{(\Delta \not{E}_y)^2}{2\sigma_2^2}}$$

Each suffix of likelihood corresponds to the following items:

- $p_z^\nu Q$ – the solution of neutrino momentum z component times lepton charge
- M_{W^*} – invariant mass of all final particles.
- W – W mass constraint.
- $\not{E}_x$ – neutrino energy in x-direction.
- $\not{E}_y$ – neutrino energy in y-direction.
- sol – Imaginary part of the solution.

P^{corr}_{val} is a probability density function for the correct solution which choses p_z^ν closer to the correct one at the generator level. P^{wrong}_{val} is a probability density function for the wrong solution.

Input template shapes made with s-channel signal Monte Calro sample. Figure 7.1 shows the missing E_X and E_Y distributions and the p_z^ν solution times lepton charge distribution. Since u or $\bar{u}$ quarks in the proton or anti-proton have larger momentum than d or $\bar{d}$ quarks, W^* is boosted to the u type quark direction. This phenomenon makes an asymmetry of this distribution. Figure 7.1 also shows the reconstructed $W*$ mass distribution which is an invariant mass of all final particles.

As a result, reconstructed p_z^ν shows good agreement to the generator level p_z^ν as shown in Figure 7.2.

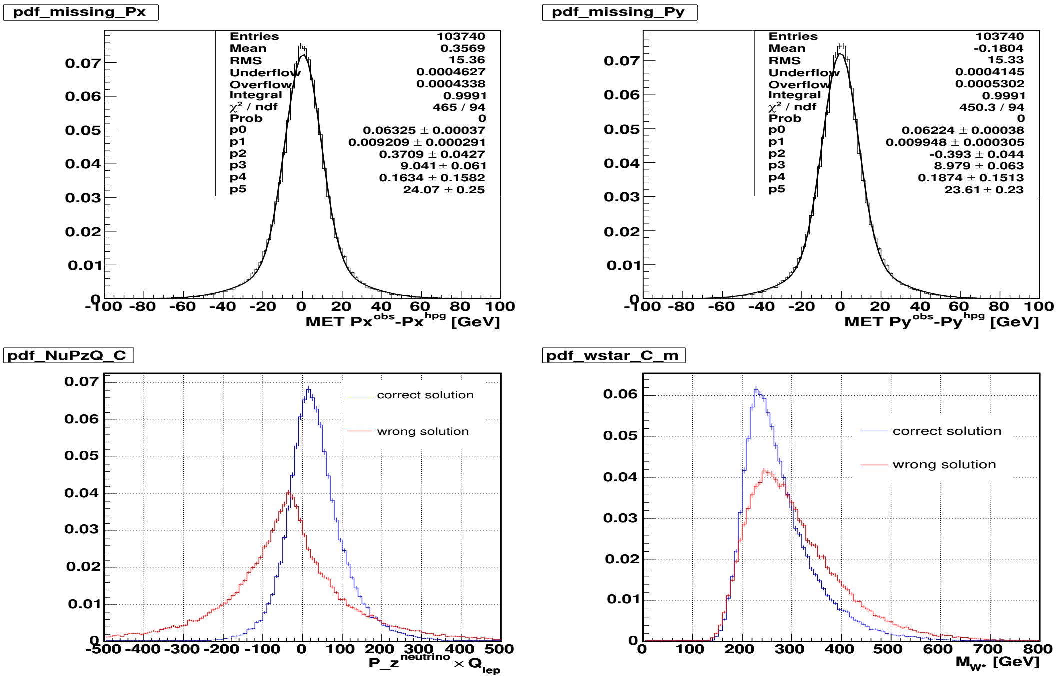

Figure 7.1: Missing E_x(top left) and E_y(top right) distributions. The solid curve shows the best fit by a double Gaussian distribution. Neutrino p_z solution times lepton charge distribution(bottom left). Reconstructed mass distribution using all final particle.(bottom right). Blue curves show the distributions for correct solutions which have p_z^{ν} closer to the correct one at the generator level red curves show for wrong solutions.

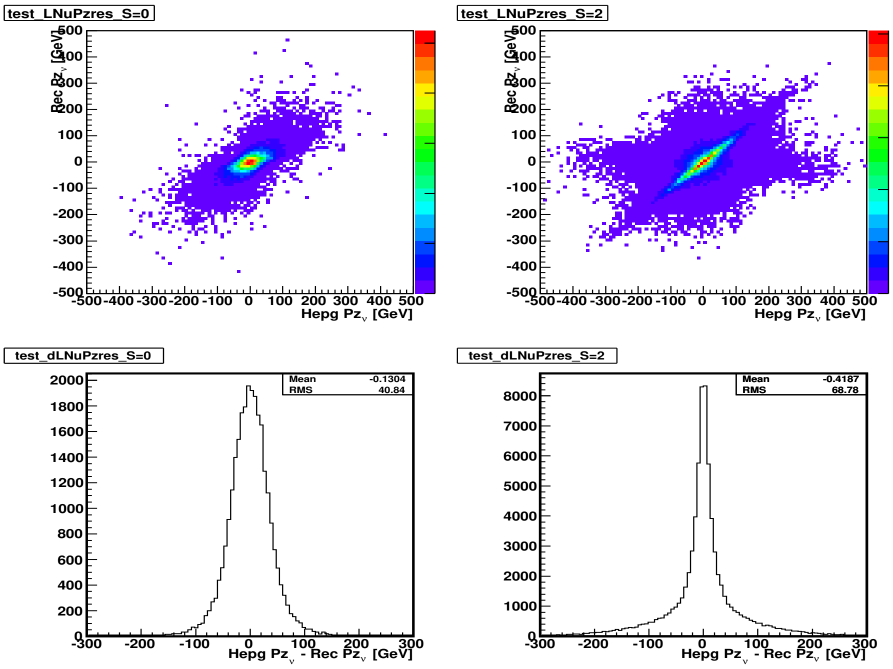

Figure 7.2: 2-dimensional plots of the p_z^ν and generator level p_z^ν. Top left plot is for 0 or 1 solution cases, and top right plot to show 2 solutions case. Bottom histograms show the pull distributions.

b-jet assignment

In calculating kinematic variables for a single top search, one important decision is the choice of b-jet from top decay. In the 2-jet bin of the t-channel, this decision is relatively easy since 97 % of events have exactly one SECVTX tight tag in the category of at least one tag. However in the 2-jet bin of the s-channel we have two real b-jets, so only the b-tag information is not sufficient to choose the b-jet from top decay.

We construct a likelihood for b-jet from top decay as follows. $p_T(b)$, M_{lb}, $\cos\theta_b \times Q_{lep}$, where $p_T(b)$ is b-jet p_T, M_{lb} is the invariant mass of lepton + b-jet and $\cos\theta_b \cdot Q_{lep}$ is a scattering angle of b-jet in initial quarks ($q\bar{q}$) rest frame and Q_{lep} is a lepton charge. We pick up a b-jet which have larger likelihood as the b-jet from top decay.

$$\mathcal{L}_{bb} = \mathcal{L}_{b_{p_T}} \times \mathcal{L}_{M_{lb}} \times \mathcal{L}_{cos\theta_b \cdot Q_{lep}} \times \mathcal{L}_{M_{top}} \tag{7.3}$$

where,

$$\mathcal{L}_{b_{p_T}} = \frac{P^{b_{top}}_{p_T}}{P^{b_{other}}_{p_T}}, \quad \mathcal{L}_{M_{lb}} = \frac{P^{b_{top}}_{M_{lb}}}{P^{b_{other}}_{M_{lb}}}, \quad \mathcal{L}_{cos\phi \cdot Q_{lep}} = \frac{P^{b_{top}}_{cos\phi \cdot Q_{lep}}}{P^{b_{other}}_{cos\phi \cdot Q_{lep}}}, \quad \mathcal{L}_{M_{top}} = \frac{1}{\Delta M^2_{M_{top}} + \sigma^2_{M_{top}}}$$

$P^{b_{top}}_{val}$ is a probability density function for the valiable picking up b-jet from top quark decay. $P^{b_{other}}_{val}$ is a probability density function picking up the other b-jet.

Input template shapes were made with the s-channel single top signal Monte Carlo sample. Figure 7.3 shows the b-jet transverse momentum distribution. The b-jet from top decay is more energetic than the other b-jet. Figure 7.3 also shows the invariant mass distribution of lepton and b-jet and the $\cos\theta_b \times Q$ distribution at initial two quarks($q\bar{q}'$) rest frame. Quarks are left-handed and anti-quarks are right-handed since s-channel process is completely weak interaction(V-A coupling). In Figure 7.4, blue arrows show the preferred helicity directions of the particles. As we understand from this figure, it is probable for $b(\bar{b})$ quark coming from W^* to be produced in the direction of $P(\bar{P})$. This makes very larger difference in the $\cos\theta_b \times Q_{lep}$ distribution between b-jet from top decay and the other b-jet. As a result, this likelihood enables us to choose the b-jet from top decay with 82 % probability.

7.2 b-Jet Energy Correction

The standard CDF jet energy corrections correct the energies of jets in a way that the mean of the corrected jet energies is set to the original parton energy for light flavor jets. The b-jets need further specific correction. So we obtained the b-jet specific correction in the s-channel single top production process as shown in Figure 7.5.

Figure 7.6 shows the reconstructed top quark mass distribution. As a result, using the

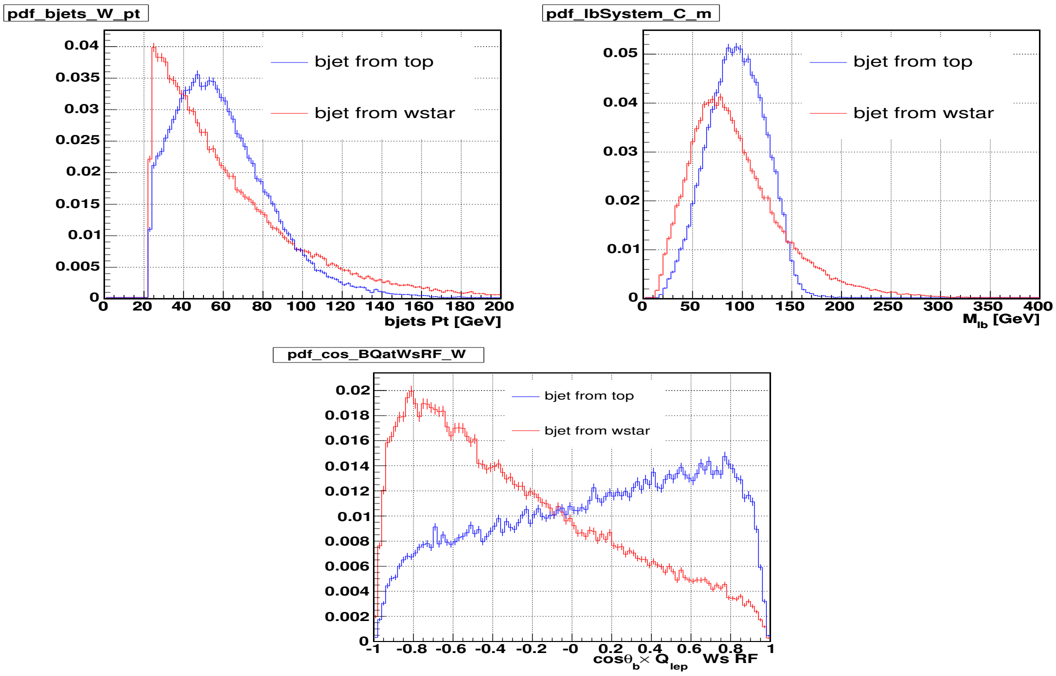

Figure 7.3: b-jet transverse momentum distribution(top left). Invaliant mass distribution of lepton and b-jet(top right). Cosine theta of b-jet times lepton charge distribution at initial two quarks($q\bar{q}'$) rest frame(bottom). Blue histgrams are made by using b-jet which is coming from top quark decay. Red histgrams are made by using the other b-jet.

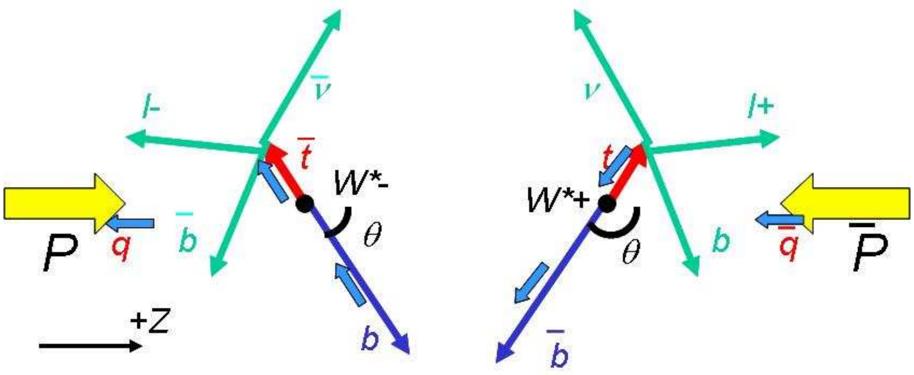

Figure 7.4: Final state behavior at the W^* rest frame

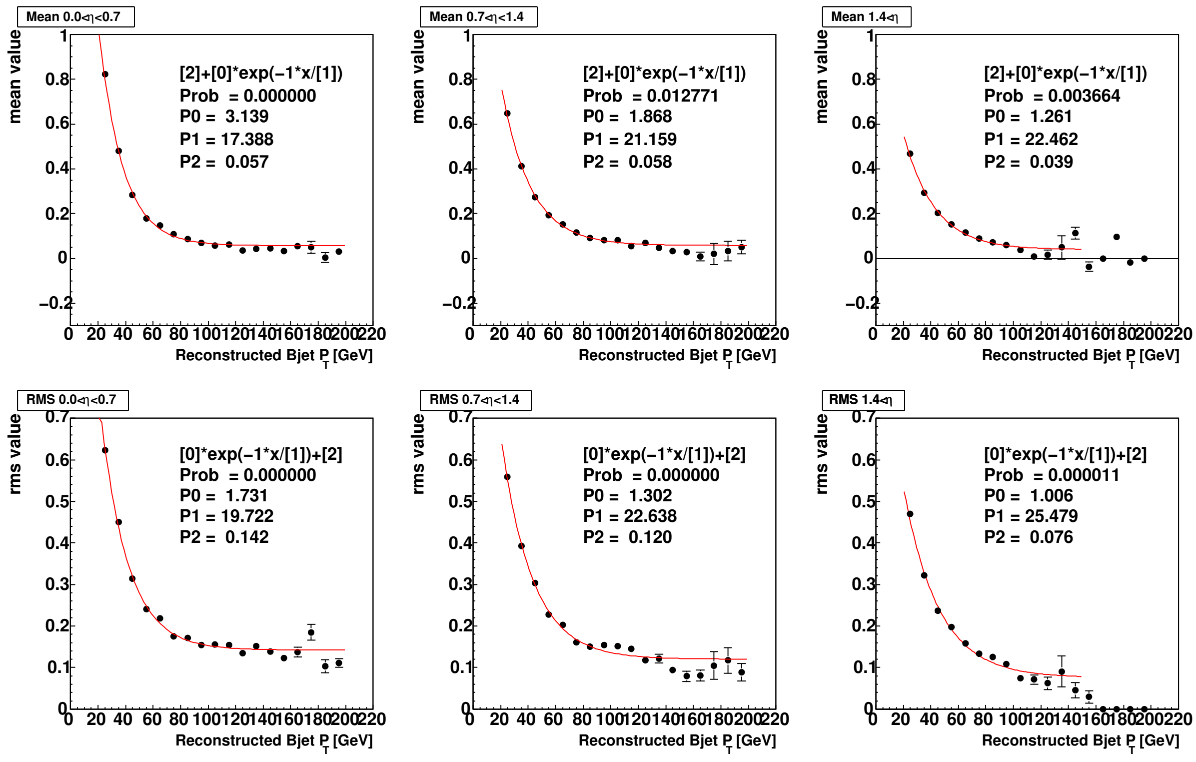

Figure 7.5: Top plots show the b-jet specific correction factor as a function of p_T. The horizontal axis shows reconstructed b-jet p_T in GeV and vertical axis shows the correction factors comparing obtained the measured energy and generator level parton energy. We divided them into three η range ($0 \leq |\eta| < 0.7$, $0.7 \leq |\eta| < 1.4$, $|\eta| \geq 1.4$). Bottom plots show the statistic uncertainties on the correction factors.

s-channel optimized kinematics fitter, the top quark mass resolution is 24.5 GeV in r.m.s.

7.3 Likelihood-Based Separator of Signal from Background

In order to discover the single top production, and to measure its rate with a highest significance, we must take advantage of as many differences between the signal and the background as possible. To this end, a variety of quantities which can be computed from the reconstructed event variables have been investigated for their ability to separate the signal from the background. As no single variable encodes any conceivable separation, a likelihood is proposed combining several variables together into one discriminant to compute the cross section limits or to discover the signal.

The Likelihood $\mathcal{L}$ is constructed first by forming the template histogram of each variable, separately for the signal and for the several backgrounds, denoted P_i^m for variable i for the background event class m and the signal. Since about 75 % of the background are W+HF and $t\bar{t}$, we used t-channel single top, W+HF and $t\bar{t}$ as the background templates. These three background

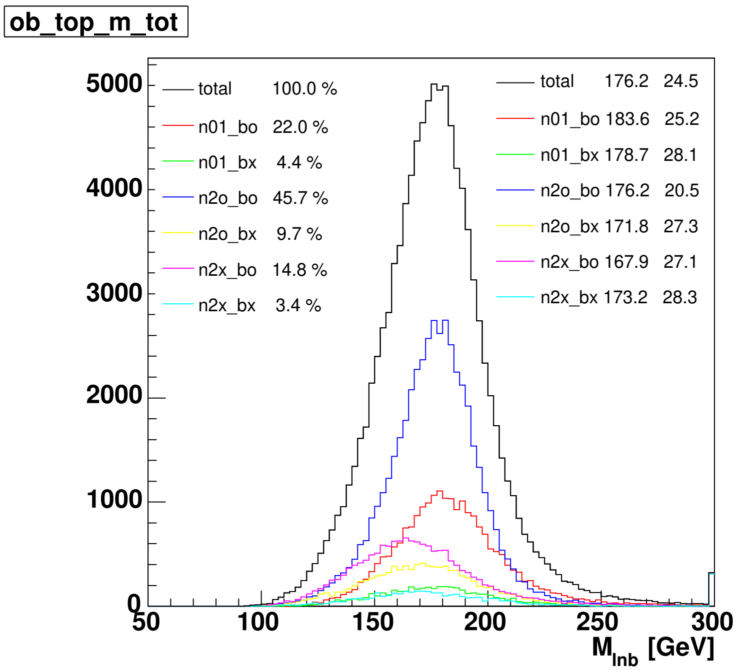

Figure 7.6: Black histogram shows reconstructed top quark mass distribution (simulation). Other colored histograms are breakdowns made using the generator level information. The meaning of the legend is following: n01 is 0 or 1 solution, n2o is 2 solutions and correct solution, n2x is 2 solutions and wrong solution, bo is successful in choosing b-jet combination, bx is failed in choosing b-jet conbination.

classes are separately used to construct the likelihood. These histogram are normalized so that area is unity. The likelihood is defined as :

$$\mathcal{L}^{signal} = \frac{\prod_{i=1}^{n_{val}} P_i^{\mathrm{signal}}}{\prod_{i=1}^{n_{val}} P_i^{\mathrm{signal}} + \sum_{m=1}^{n_{bkg}} \prod_{i=1}^{n_{val}} P_i^{m} \times \alpha^m} \tag{7.4}$$

where,

$$P_i^{\mathrm{process}} = \frac{f_i^{\mathrm{process}}}{f_i^{\mathrm{signal}} + \sum_{m=0}^{n_{bkg}} f_i^{\mathrm{m}}}, \quad \alpha^m = \frac{N_{\mathrm{eve}}^m}{\sum_{m=1}^{n_{bkg}} N_{\mathrm{eve}}^m}. \tag{7.5}$$

f is the bin content of template histograms of each variable, and N_{eve}^m is the number of expected events described in Chapter 6. The likelihood ignores the correlation between the input variables, although it is critical that the predicted distributions of $\mathcal{L}$ for the signal and the backgrounds are computed using a fully correlated set of input variables - from Monte Calro or from control data sample.

In order to obtain the optimized likelihood we examine the following 18(23) variables for 2jet-bin(3jet-bin) :

- M_{bb} : di-jet invariant mass
- p_{Tbb} : transverse momentum of $b\bar{b}$ system
- ΔR_{bb} : $\sqrt{\Delta\phi_{bb}^2 + \Delta\eta_{bb}^2}$
- $M_{l\nu b}$: invariant mass of lepton, neutorino and b-jet from top quark decay
- M_{invbjj} : hadronic decayed top quark invariant mass using b-jet, LF jet, and invisible jet [1] and M_W constraint, if 3jet-bin.
- p_T(j1) : leading jet transverse momentum
- p_T(j2) : second leading jet transverse momentum
- p_T(j3) : third leading jet transverse momentum, if 3jet-bin.
- p_T(non-b) : non-b assigned jet transverse momentum, if 3jet-bin.
- η(j1) : leading jet pseudo-rapidity
- η(j2) : second leading jet pseudo-rapidity
- η(j3) : third leading jet pseudo-rapidity, if 3jet-bin.
- η(non-b) : non-b assigned pseudo-rapidity, if 3jet-bin.

[1] As the reconstruction of a jet which is not reconstructed in the CDF detector, we define the invisible jets which has only the z direction momentum.

- Ht : transverse momentum scalar sum of lepton, neutrino and two jets

- $\not{E}_T$: Missing transverse energy

- M_{WT} : W transverse mass.

- p_T(lep) : lepton transverse momentum

- η(lep) : lepton pseudo-rapidity

- $Q \times \eta$: non-b or non-top-decay assigned jet pseudo-rapidity times lepton charge.

- $\cos\theta^*$: cosine angle between lepton and d-type initial quark direction in the top quark restframe.

- $\mathcal{M}_{\mathrm{LLR}}$: log likelihood ratio constructed by Wbb, $t-$channel and $s-$channel matrix elements [2].

- $\mathcal{L}_{\nu\mathrm{sol}} \times \mathcal{L}_{bb\mathrm{sol}}$: kinematics fitter likelihood output times the likelihood for b-jet from top decay.

The figure of merit of the discriminant is $s/\sqrt{s+b}$ with the optimum parameters having the maximum value, where s is the number of signal evnets and b is the number of background events. We found the sensitivity are maximum when the following 10(9) variables are used for 2jet-bin(3jet-bin).

2jet-bin

- M_{bb} : di-jet invariant mass

- p_{Tbb} : transverse momentum for $b\bar{b}$ system

- ΔR_{bb} : $\sqrt{\Delta\phi_{bb}^2 + \Delta\eta_{bb}^2}$

- $M_{l\nu b}$: invariant mass of lepton, neutorino and b-jet from top quark decay

- p_T(j1) : leading jet transverse momentum

- η(j2) : second leading jet pseudo-rapidity

- p_T(lep) : lepton transverse momentum

- $Q \times \eta$: non-b or non-top-decay assigned jet pseudo-rapidity times lepton charge.

- $\mathcal{M}_{\mathrm{LLR}}$: log likelihood ratio constructed by Wbb, $t-$channel and $s-$channel matrix elements.

[2] Matrix element is calculated using HELAS [**?**] library in MadGraph generator

- $\mathcal{L}_{\nu\mathrm{sol}} \times \mathcal{L}_{bb\mathrm{sol}}$: kinematics fitter likelihood output times the likelihood for b-jet from top decay.

3jet-bin

- ΔR_{bb} : $\sqrt{\Delta\phi_{bb}^2 + \Delta\eta_{bb}^2}$
- $M_{l\nu b}$: invariant mass of lepton, neutorino and b-jet from top quark decay
- M_{invbjj} : hadronic decayed top quark invariant mass by b-jet, LF jet, and invisible jet and M_W constraint, if 3jet-bin.
- p_T(non-b) : non-b assigned jet transverse momentum, if 3jet-bin.
- η(j1) : leading jet pseudo-rapidity
- η(j2) : second leading jet pseudo-rapidity
- η(lep) : lepton pseudo-rapidity
- $\cos\theta^*$: cosine angle between lepton and d-type initial quark direction in the top quark restframe.
- $\mathcal{L}_{\nu\mathrm{sol}} \times \mathcal{L}_{bb\mathrm{sol}}$: kinematics fitter likelihood output times the likelihood for b-jet from top decay.

Figure 7.7-7.34 show the kinematics shapes of input valiables compared between signal and main backgrounds. Also shown are expected and CDF RunII data shapes. The plots are shown separately for the different categories as listed below:

- Triggered lepton, W+2jet-bin, SecVtx + SecVtx tagged: Figure 7.7-7.10
- Triggered lepton, W+3jet-bin, SecVtx + SecVtx tagged: Figure 7.11-7.13
- Untriggered muon, W+2jet-bin, SecVtx + SecVtx tagged: Figure 7.14-7.17
- Untriggered muon, W+3jet-bin, SecVtx + SecVtx tagged: Figure 7.18-7.20
- Triggered lepton, W+2jet-bin, SecVtx + JetProb tagged: Figure 7.21-7.24
- Triggered lepton, W+3jet-bin, SecVtx + JetProb tagged: Figure 7.25-7.27
- Untriggered muon, W+2jet-bin, SecVtx + JetProb tagged: Figure 7.28-7.31
- Untriggered muon, W+3jet-bin, SecVtx + JetProb tagged: Figure 7.32-7.34

We show similar plots in appendix (Figure A.1-A.14) for the single SecVtx b-tagged sample events that have two taggable jets but one b-tagged jet.

Triggered lepton W+2jets SecVtx+SecVtx category:

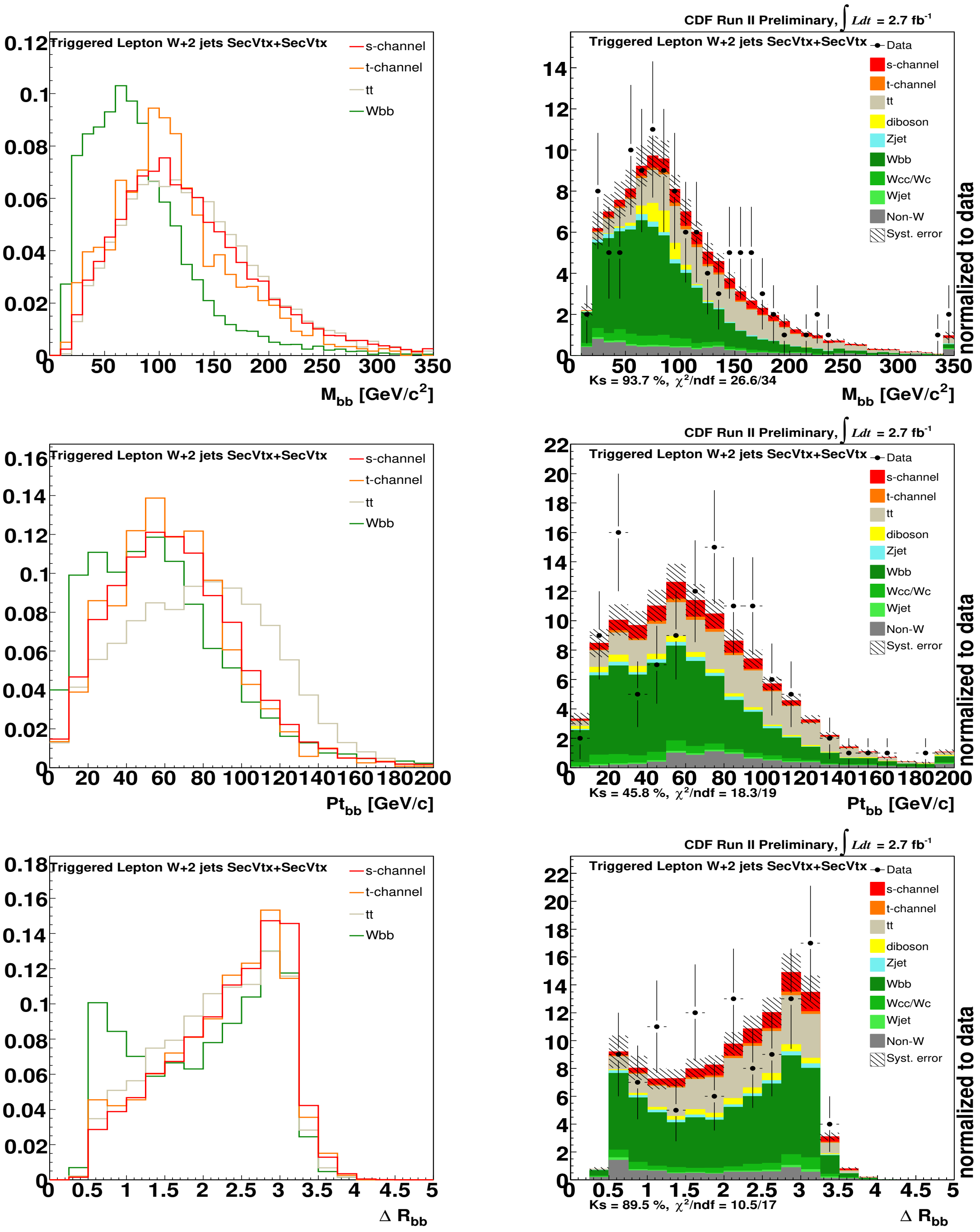

Figure 7.7: Kinematic variables shapes comparison between signal and main background(Wbb, $t\bar{t}$ and t-channel) are shown in left, and Kinematic variables shapes comparison between expected and CDF RunII data are shown in right. The variables are M_{bb}, p_{Tbb} and ΔR_{bb} from the top.

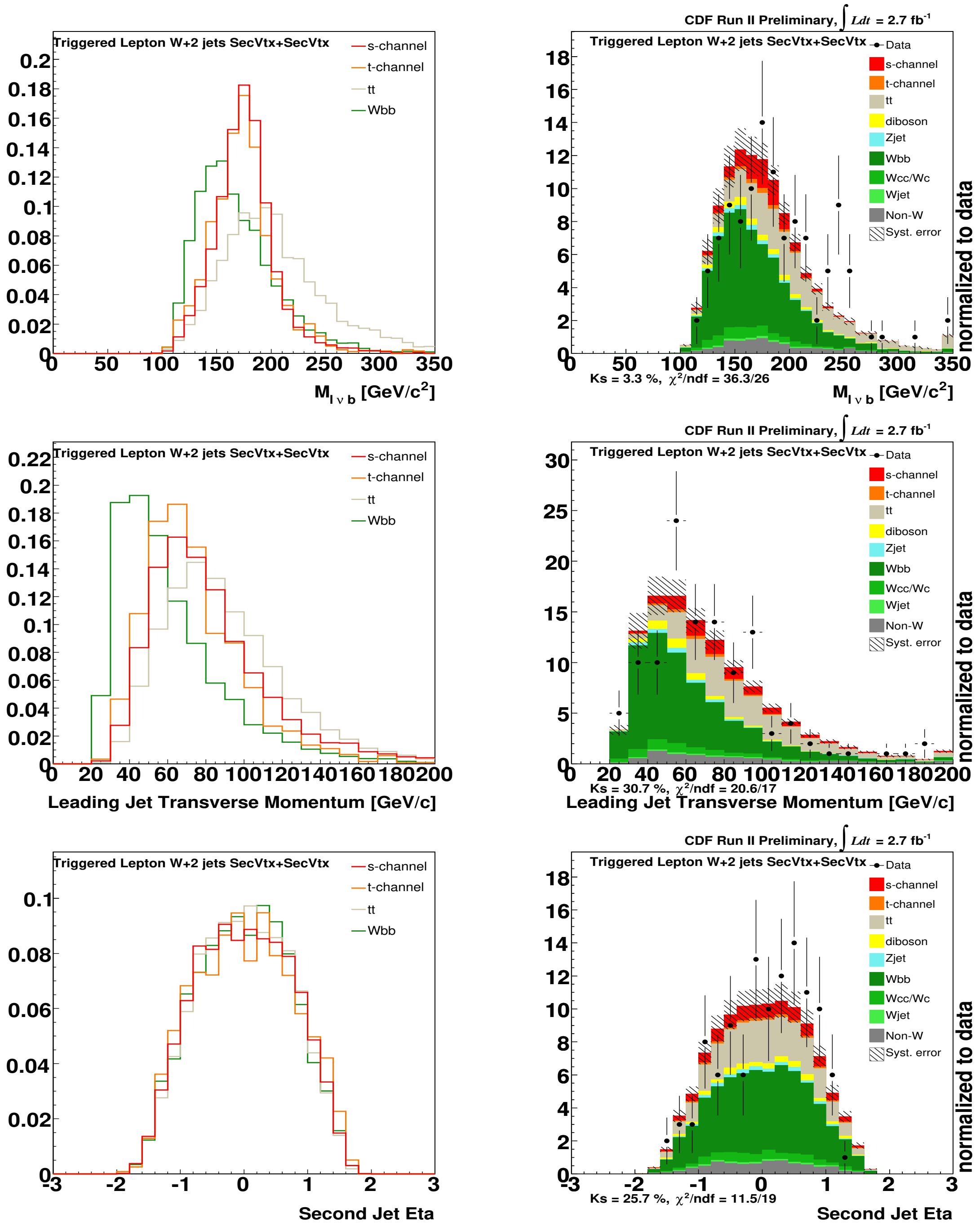

Figure 7.8: Kinematic variables shapes comparison between signal and main background(Wbb, $t\bar{t}$ and t-channel) are shown in left, and Kinematic variables shapes comparison between expected and CDF RunII data are shown in right. The variables are $M_{l\nu b}$, p_T(j1) and η(j2) from the top.

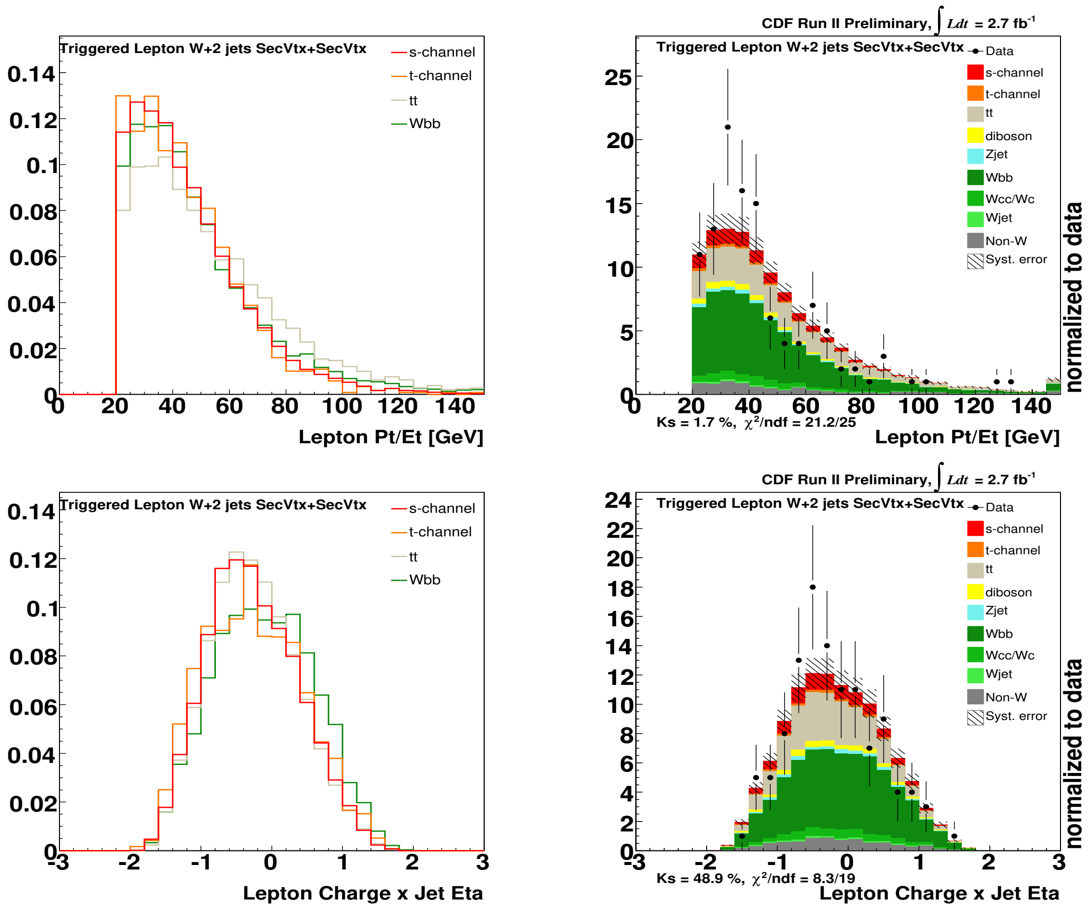

Figure 7.9: Kinematic variables shapes comparison between signal and main background(Wbb, $t\bar{t}$ and t-channel) are shown in left, and Kinematic variables shapes comparison between expected and CDF RunII data are shown in right. The variables are p_T(lep) and $Q \times \eta$ from the top.

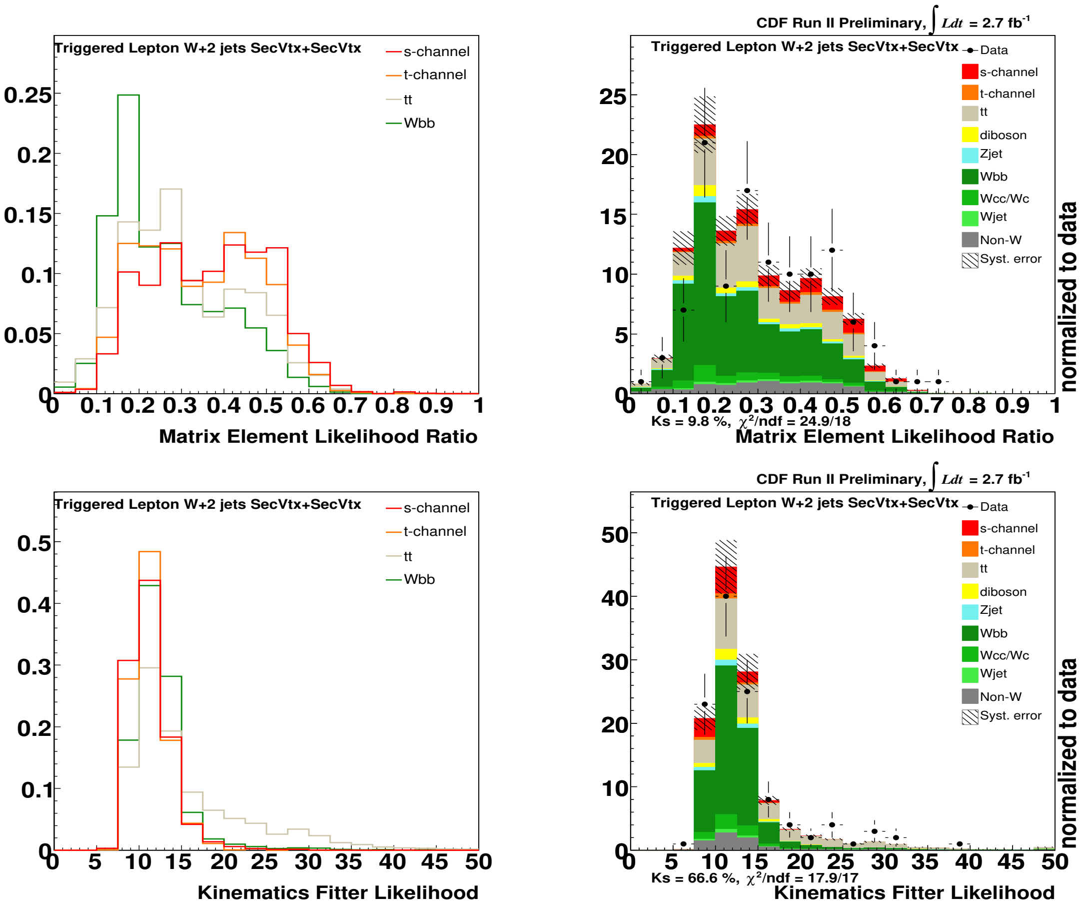

Figure 7.10: Kinematic variables shapes comparison between signal and main background(Wbb, $t\bar{t}$ and t-channel) are shown in left, and Kinematic variables shapes comparison between expected and CDF RunII data are shown in right. The variables are $\mathcal{M}_{\rm LLR}$ and $\mathcal{L}_{\nu \rm sol} \times \mathcal{L}_{bb \rm sol}$ from the top.

Triggered lepton W+3jets SecVtx+SecVtx category:

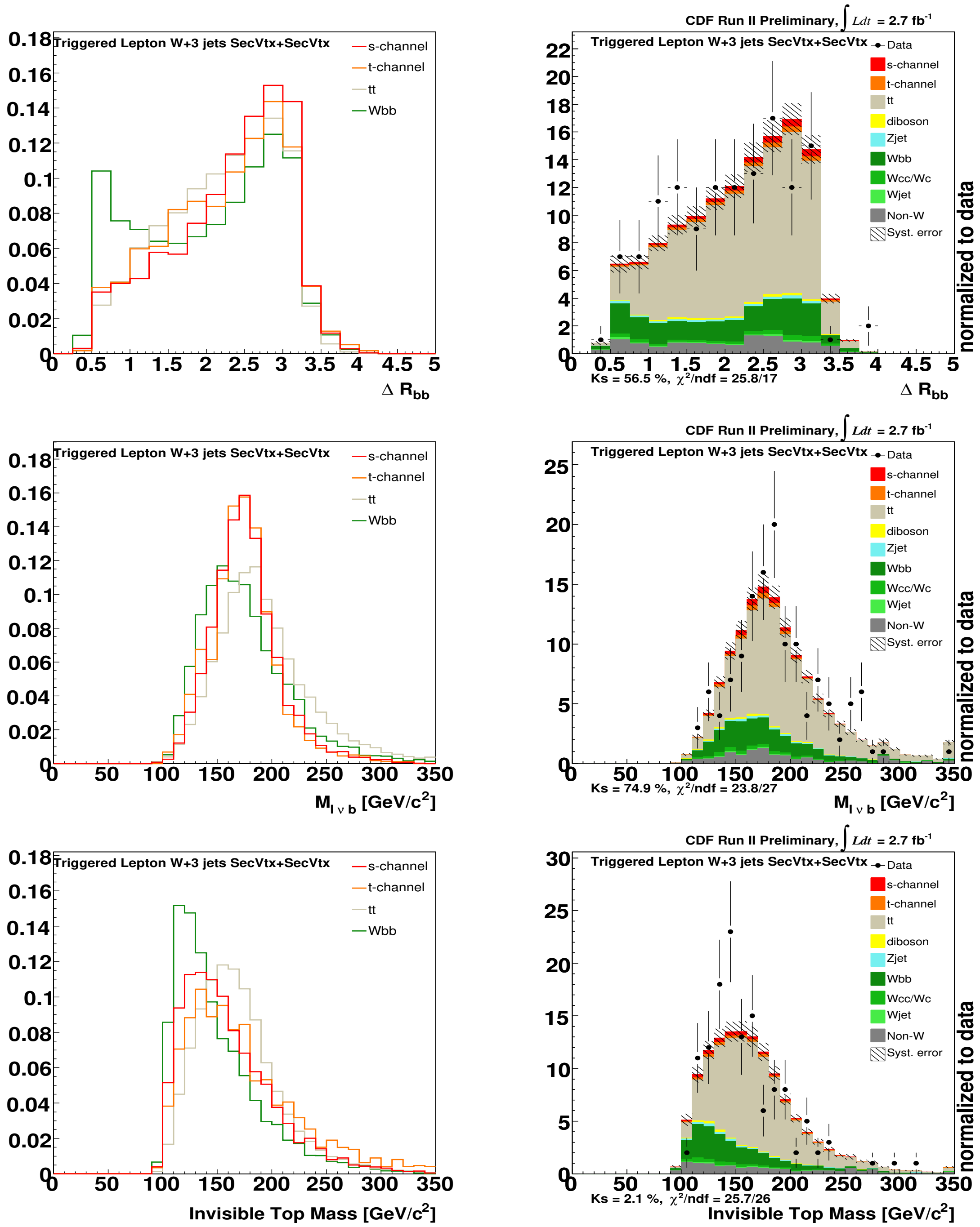

Figure 7.11: Kinematic variables shapes comparison between signal and main background(Wbb, $t\bar{t}$ and t-channel) are shown in left, and Kinematic variables shapes comparison between expected and CDF RunII data are shown in right. The variables are ΔR_{bb}, $M_{l\nu b}$ and M_{invbjj} from the top.

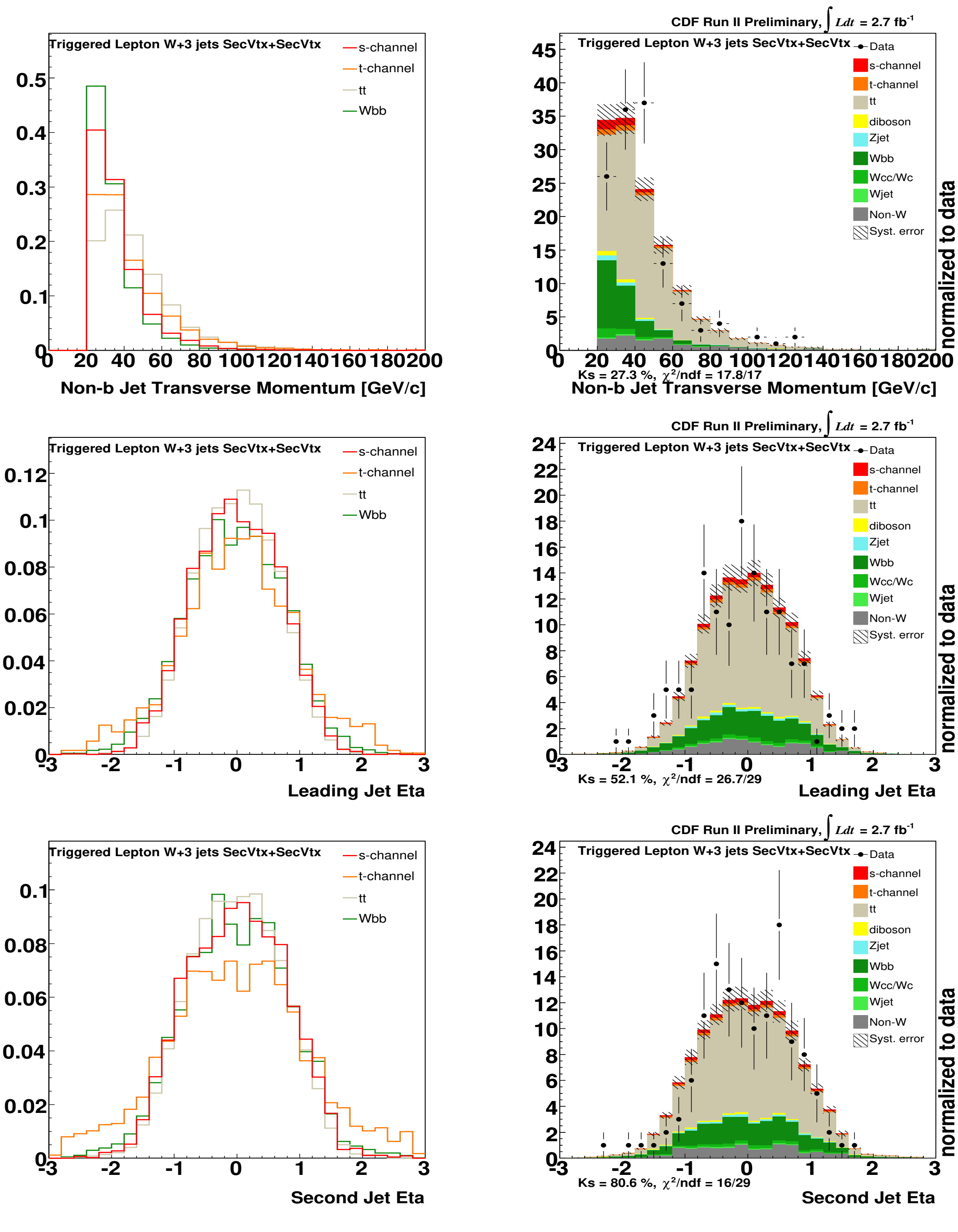

Figure 7.12: Kinematic variables shapes comparison between signal and main background(Wbb, $t\bar{t}$ and t-channel) are shown in left, and Kinematic variables shapes comparison between expected and CDF RunII data are shown in right. The variables are p_T(non-b), η(j1) and η(j2) from the top.

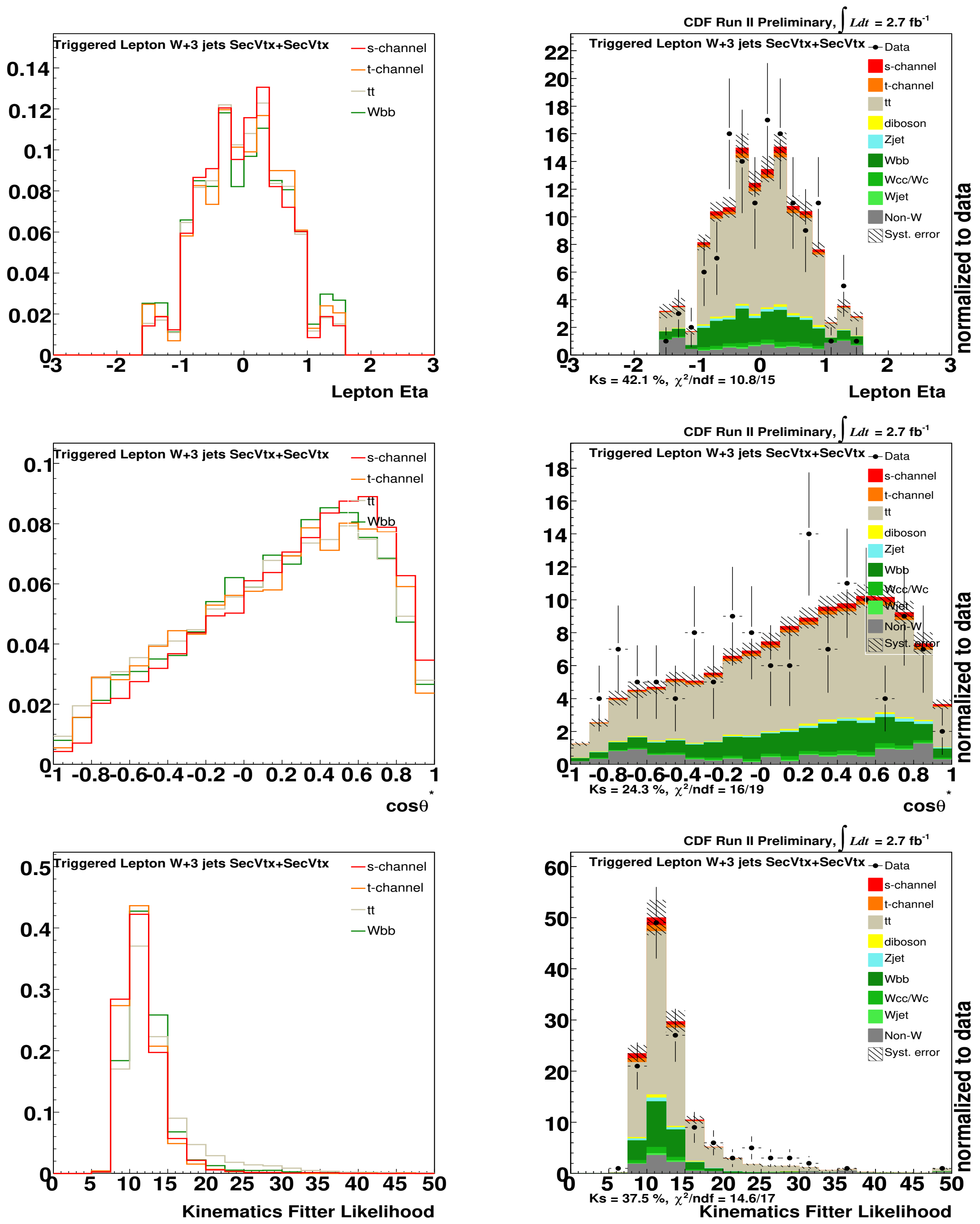

Figure 7.13: Kinematic variables shapes comparison between signal and main background(Wbb, $t\bar{t}$ and t-channel) are shown in left, and Kinematic variables shapes comparison between expected and CDF RunII data are shown in right. The variables are $\eta(\text{lep})$, $\cos\theta^*$ and $\mathcal{L}_{\nu\text{sol}} \times \mathcal{L}_{bb\text{sol}}$ from the top.

Untriggered muon W+2jets SecVtx+SecVtx category:

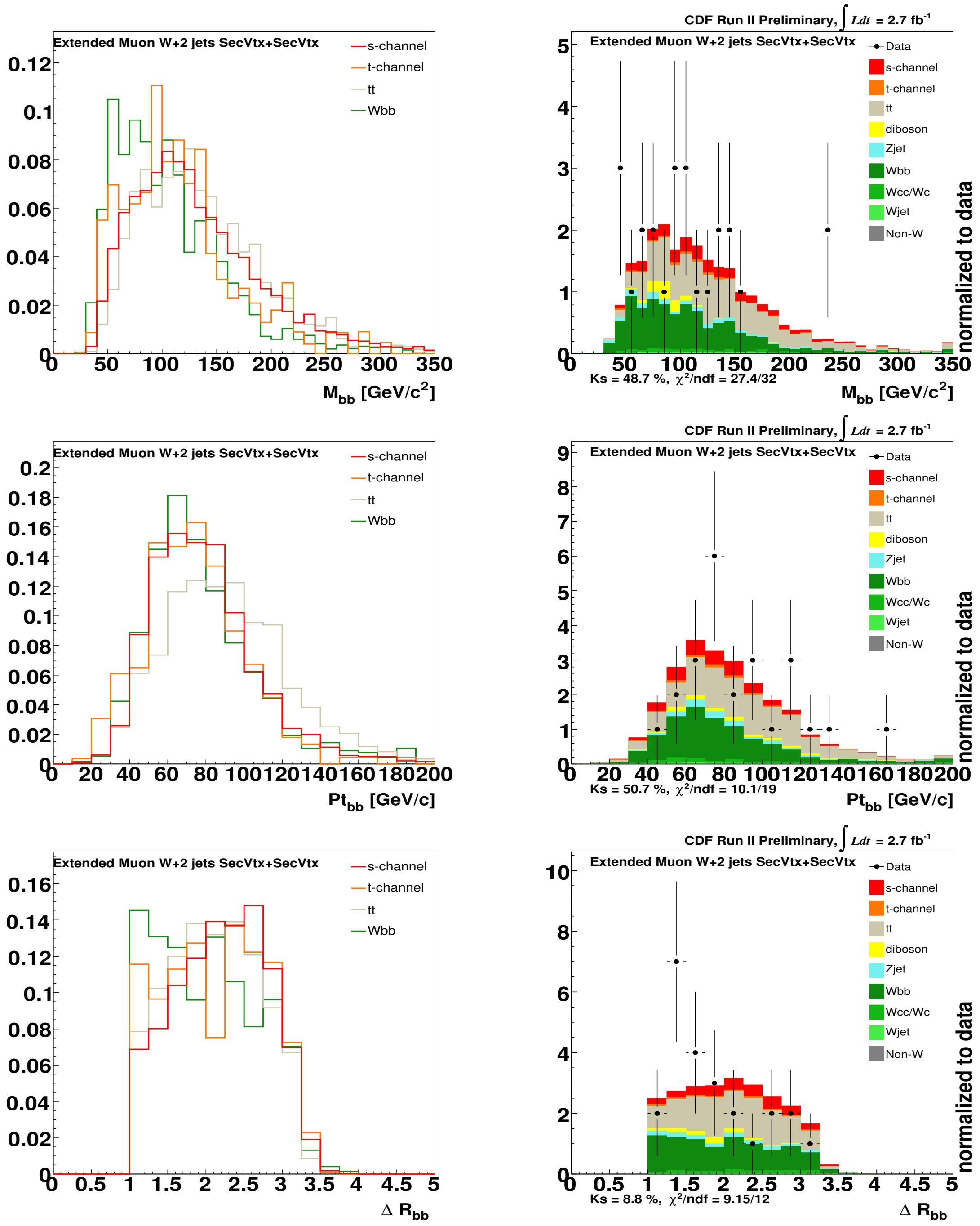

Figure 7.14: Kinematic variables shapes comparison between signal and main background(Wbb, $t\bar{t}$ and t-channel) are shown in left, and Kinematic variables shapes comparison between expected and CDF RunII data are shown in right. The variables are M_{bb}, p_{Tbb} and ΔR_{bb} from the top.

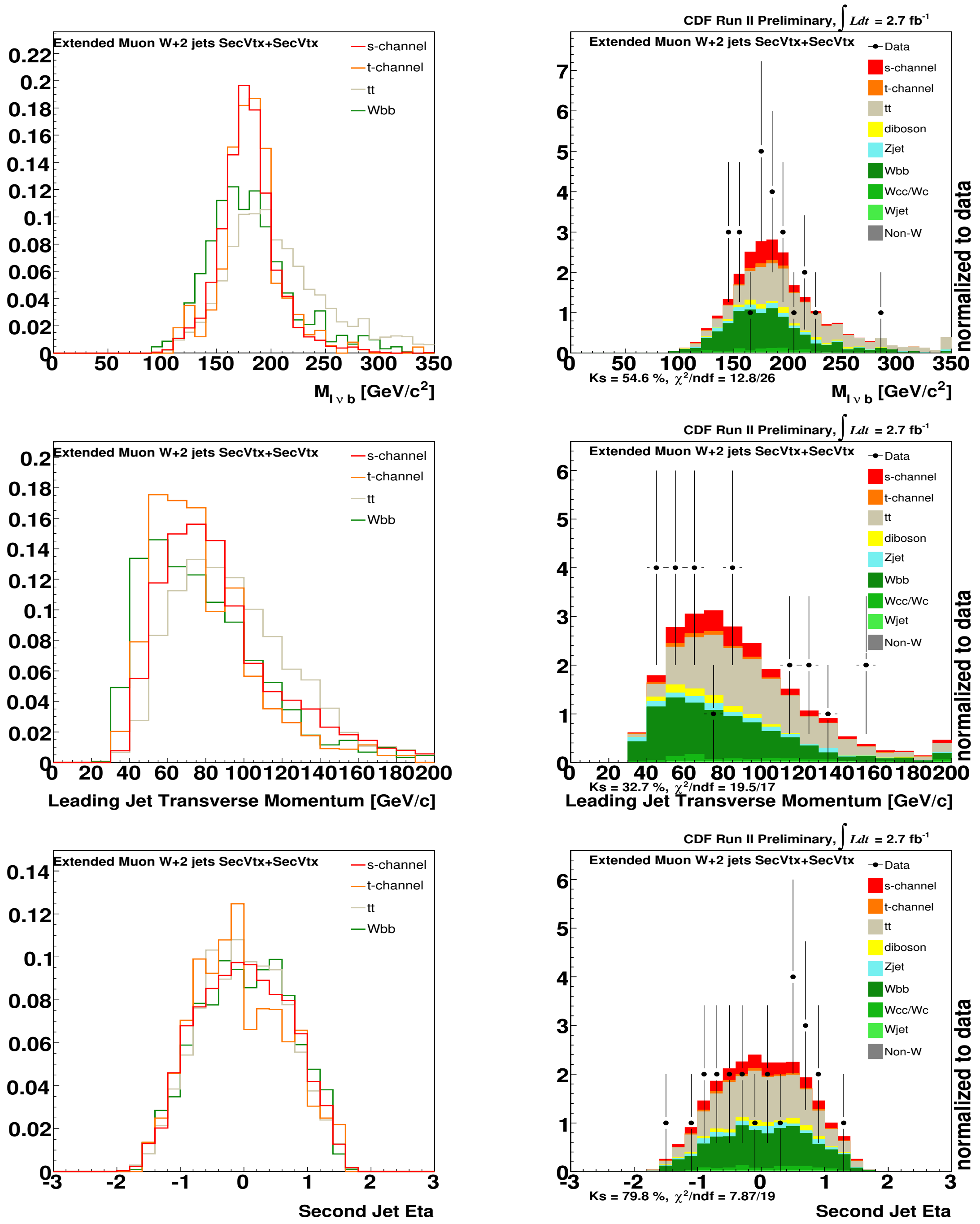

Figure 7.15: Kinematic variables shapes comparison between signal and main background(Wbb, $t\bar{t}$ and t-channel) are shown in left, and Kinematic variables shapes comparison between expected and CDF RunII data are shown in right. The variables are $M_{l\nu b}$, p_T(j1) and η(j2) from the top.

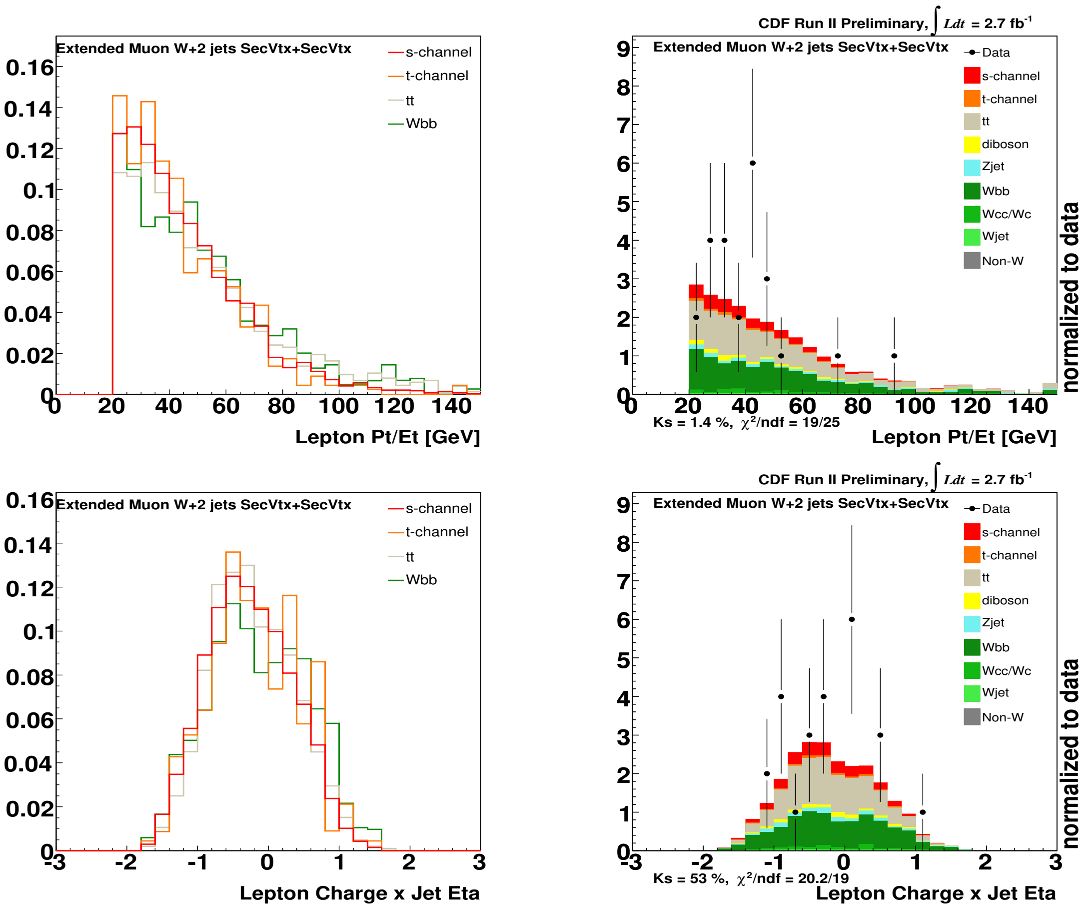

Figure 7.16: Kinematic variables shapes comparison between signal and main background(Wbb, $t\bar{t}$ and t-channel) are shown in left, and Kinematic variables shapes comparison between expected and CDF RunII data are shown in right. The variables are p_T(lep) and $Q \times \eta$ from the top.

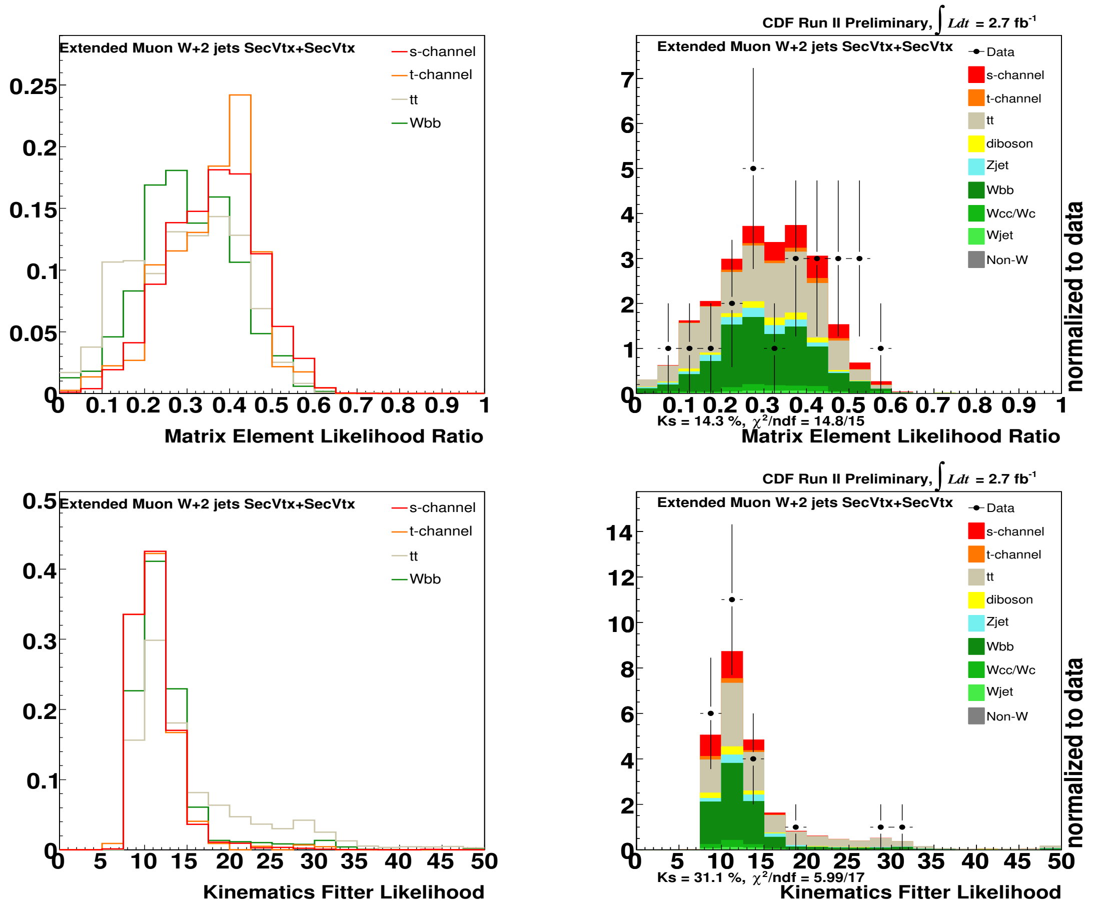

Figure 7.17: Kinematic variables shapes comparison between signal and main background(Wbb, $t\bar{t}$ and t-channel) are shown in left, and Kinematic variables shapes comparison between expected and CDF RunII data are shown in right. The variables are $\mathcal{M}_{\mathrm{LLR}}$ and $\mathcal{L}_{\nu\mathrm{sol}} \times \mathcal{L}_{bb\mathrm{sol}}$ from the top.

Untriggered muon W+3jets SecVtx+SecVtx category:

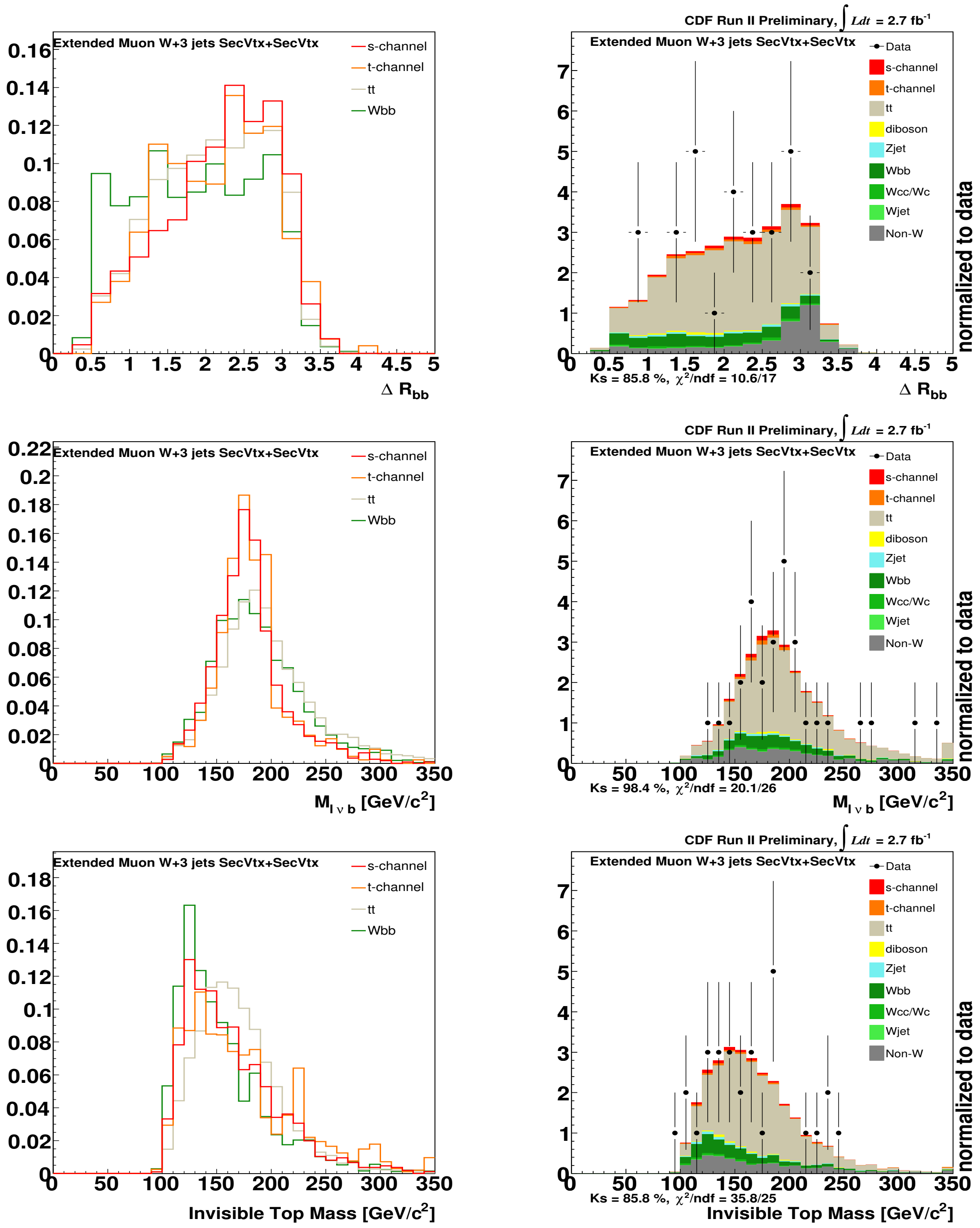

Figure 7.18: Kinematic variables shapes comparison between signal and main background(Wbb, $t\bar{t}$ and t-channel) are shown in left, and Kinematic variables shapes comparison between expected and CDF RunII data are shown in right. The variables are ΔR_{bb}, $M_{l\nu b}$ and M_{invbjj} from the top.

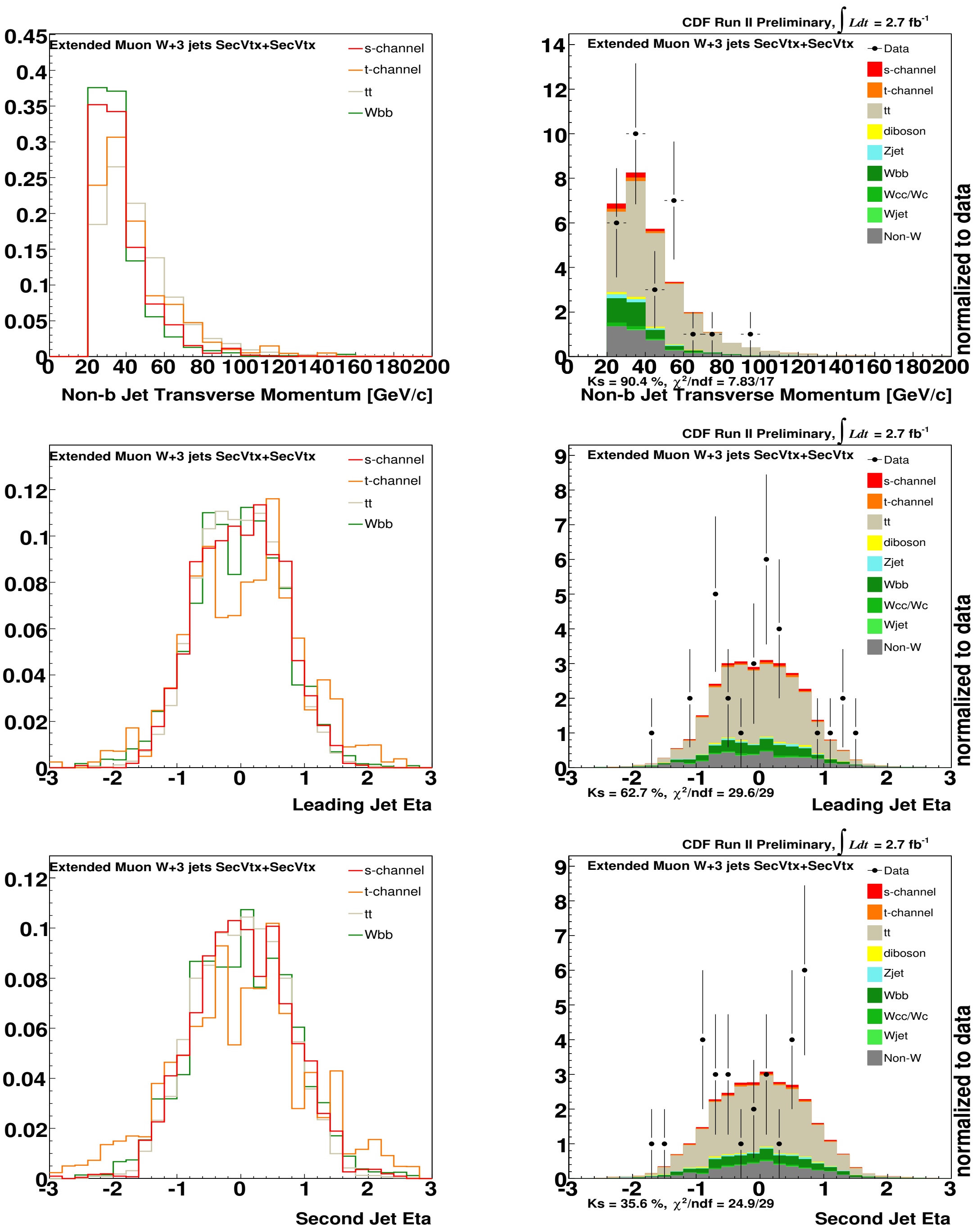

Figure 7.19: Kinematic variables shapes comparison between signal and main background(Wbb, $t\bar{t}$ and t-channel) are shown in left, and Kinematic variables shapes comparison between expected and CDF RunII data are shown in right. The variables are p_T(non-b), η(j1) and η(j2) from the top.

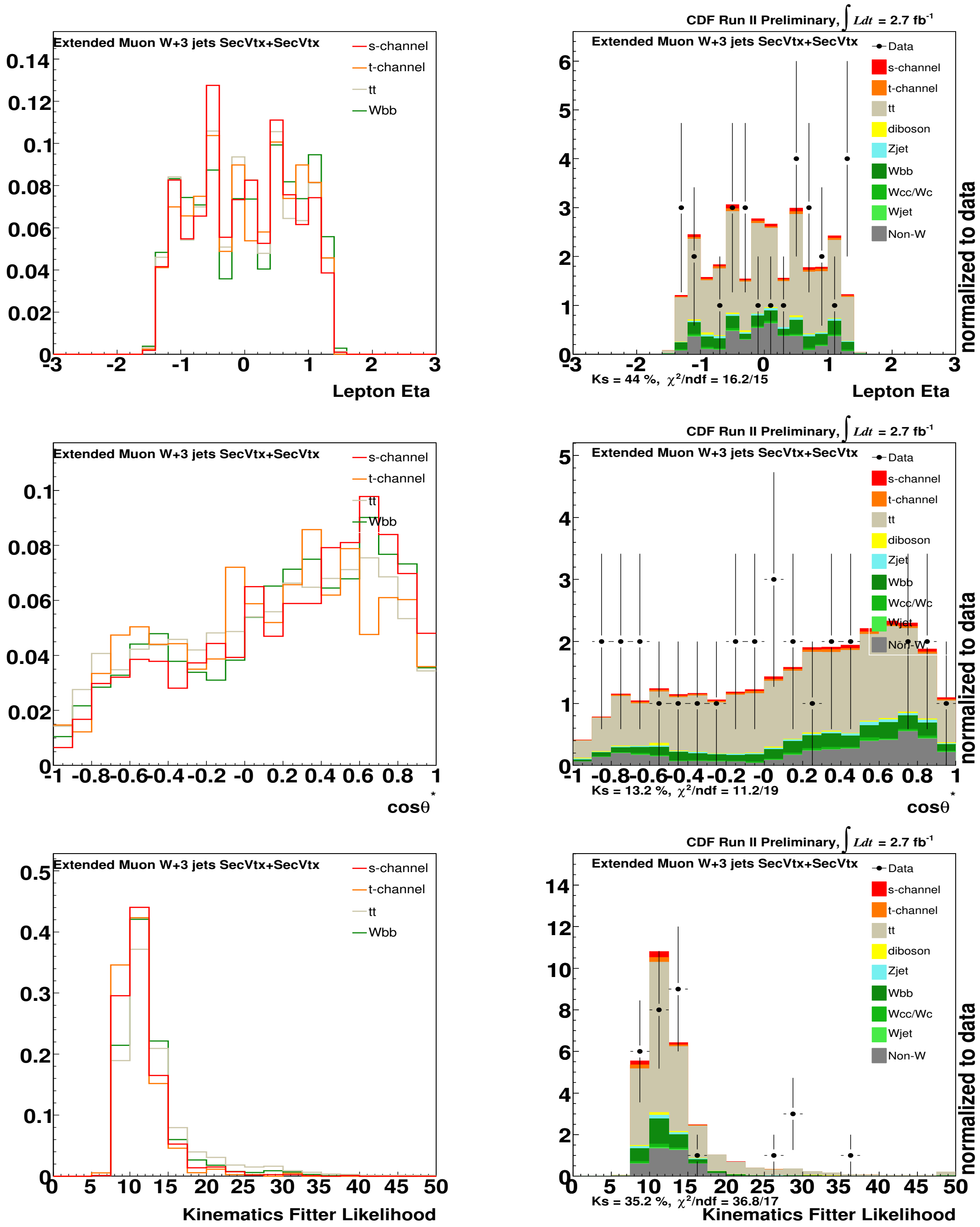

Figure 7.20: Kinematic variables shapes comparison between signal and main background(Wbb, $t\bar{t}$ and t-channel) are shown in left, and Kinematic variables shapes comparison between expected and CDF RunII data are shown in right. The variables are η(lep), $\cos\theta^*$ and $\mathcal{L}_{\nu\mathrm{sol}} \times \mathcal{L}_{bb\mathrm{sol}}$ from the top.

Triggered lepton W+2jets SecVtx+JetProb category:

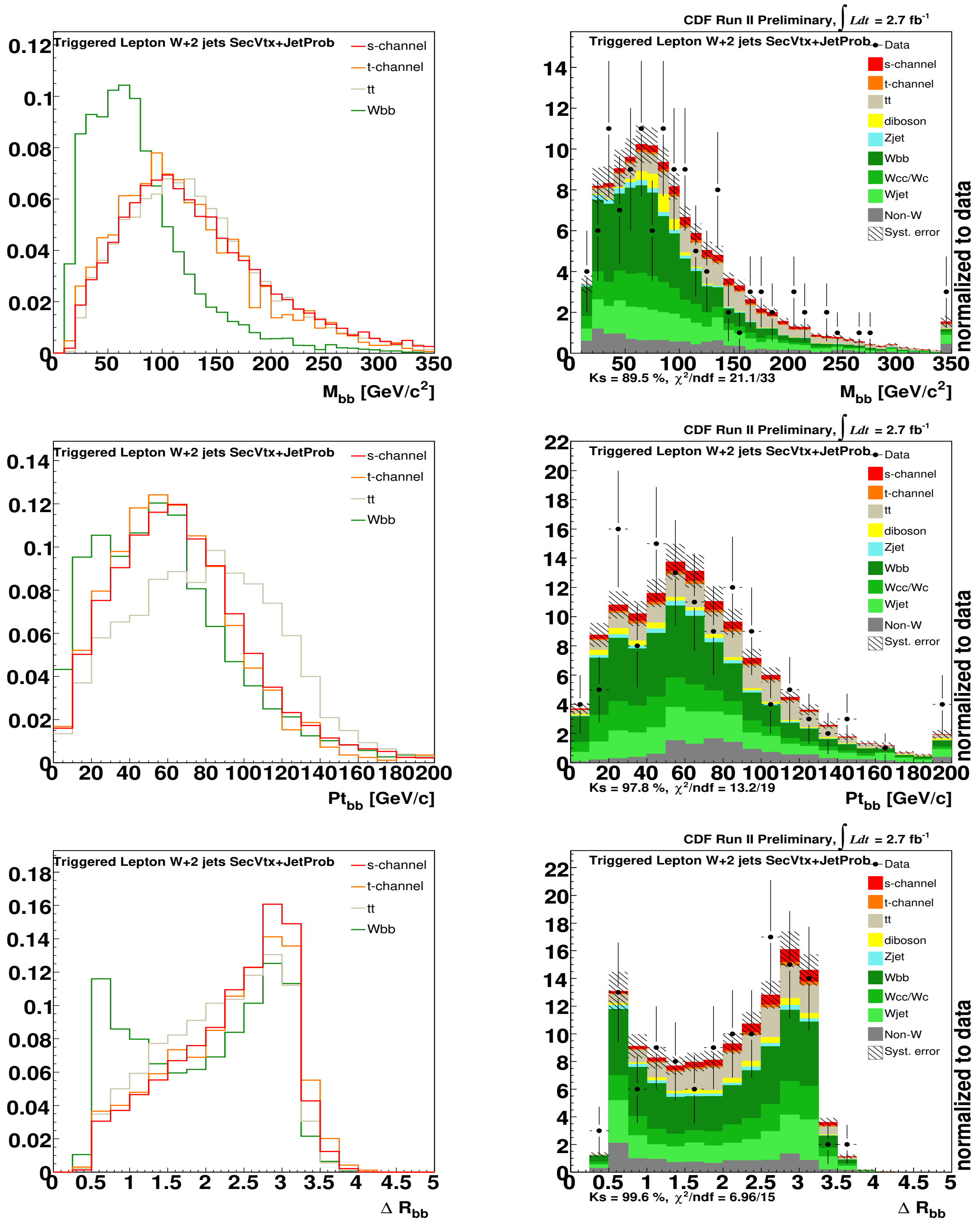

Figure 7.21: Kinematic variables shapes comparison between signal and main background(Wbb, $t\bar{t}$ and t-channel) are shown in left, and Kinematic variables shapes comparison between expected and CDF RunII data are shown in right. The variables are M_{bb}, p_{Tbb} and ΔR_{bb} from the top.

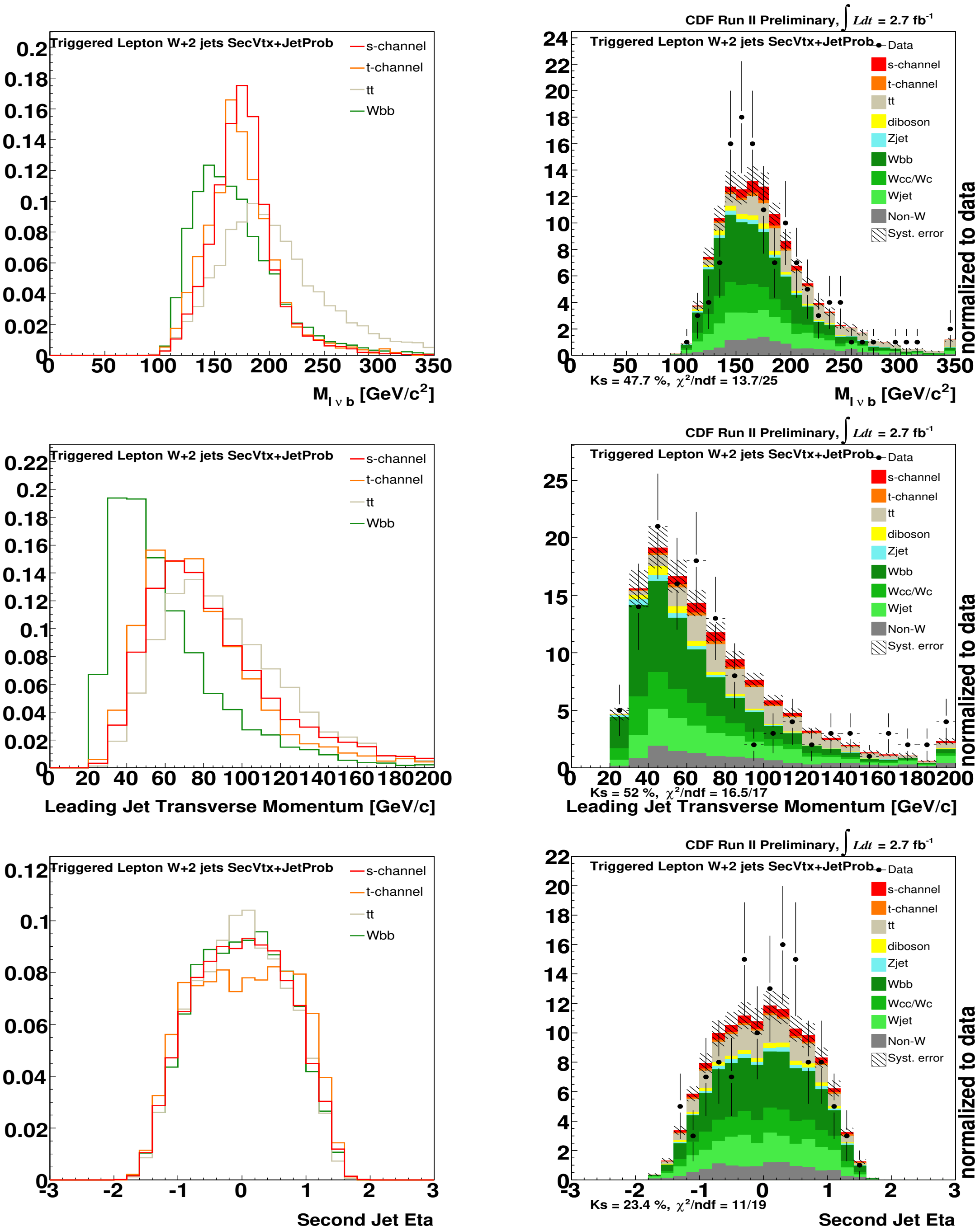

Figure 7.22: Kinematic variables shapes comparison between signal and main background(Wbb, $t\bar{t}$ and t-channel) are shown in left, and Kinematic variables shapes comparison between expected and CDF RunII data are shown in right. The variables are $M_{l\nu b}$, p_T(j1) and η(j2) from the top.

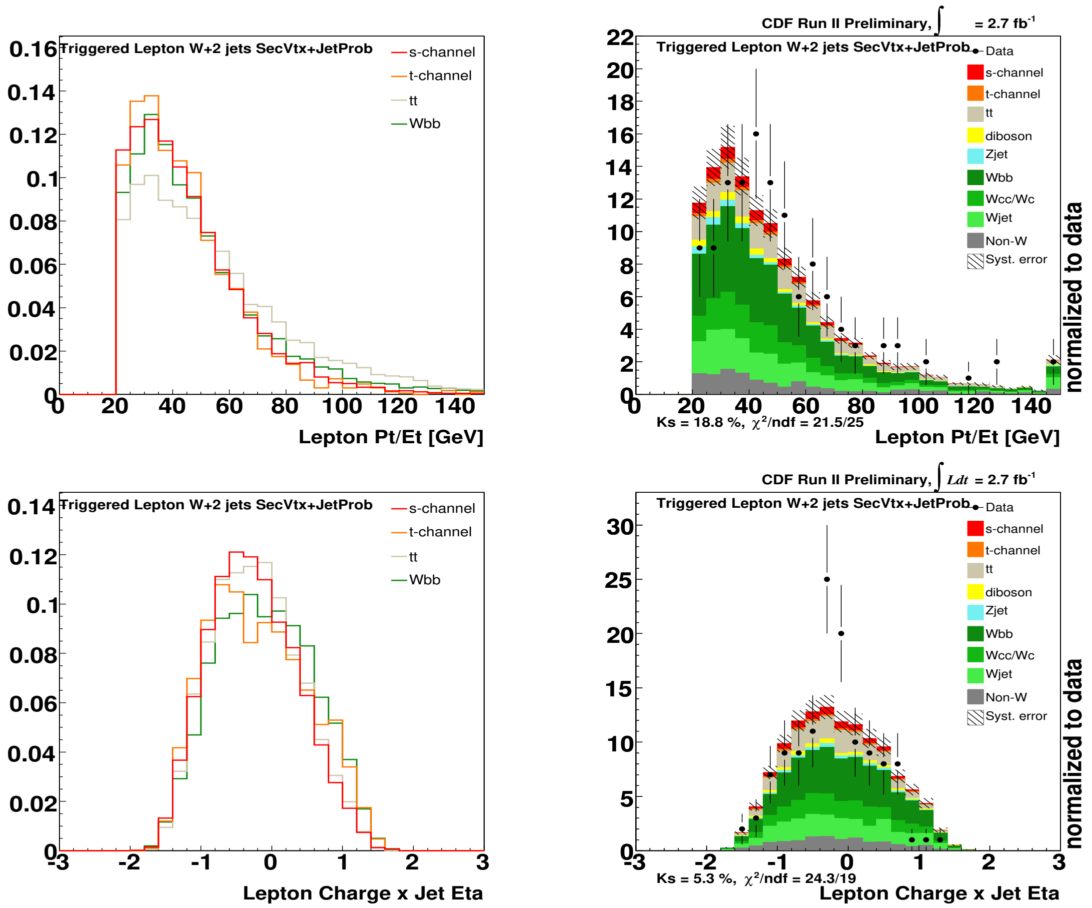

Figure 7.23: Kinematic variables shapes comparison between signal and main background(Wbb, $t\bar{t}$ and t-channel) are shown in left, and Kinematic variables shapes comparison between expected and CDF RunII data are shown in right. The variables are p_T(lep) and $Q \times \eta$ from the top.

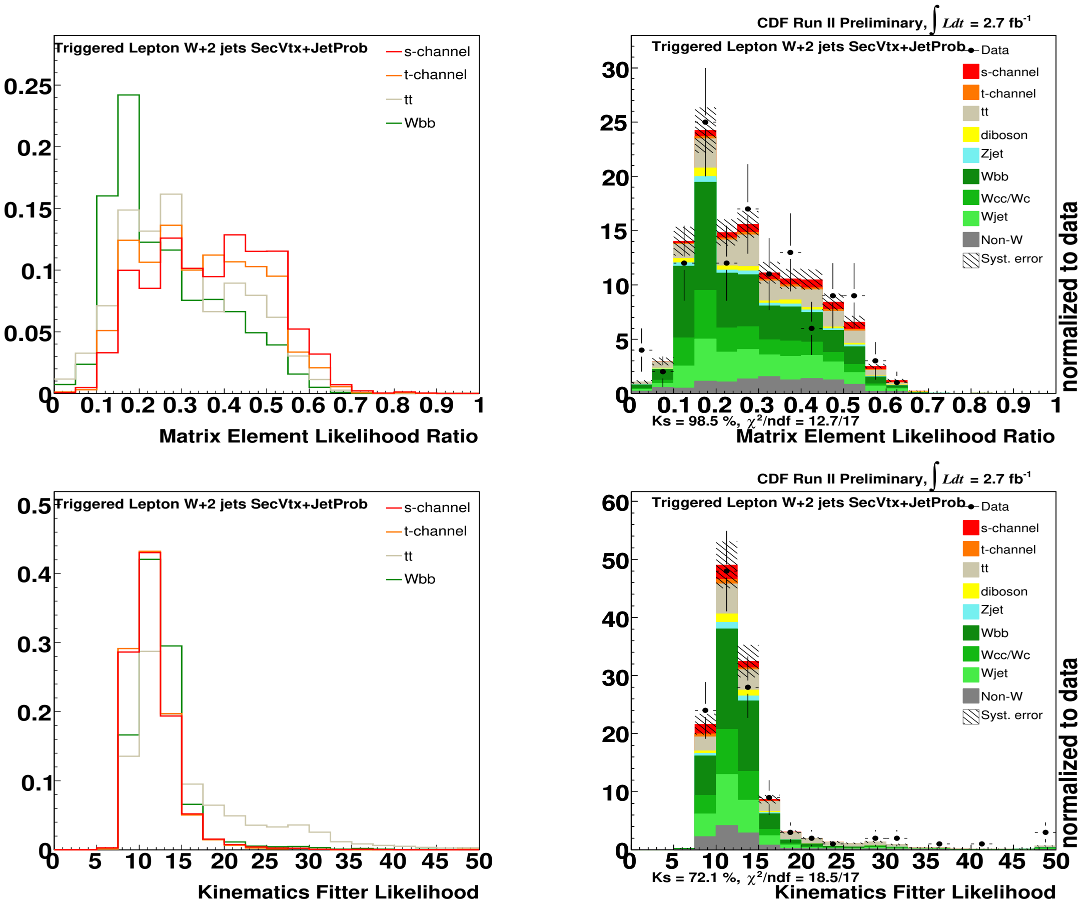

Figure 7.24: Kinematic variables shapes comparison between signal and main background(Wbb, $t\bar{t}$ and t-channel) are shown in left, and Kinematic variables shapes comparison between expected and CDF RunII data are shown in right. The variables are $\mathcal{M}_{\rm LLR}$ and $\mathcal{L}_{\nu{\rm sol}} \times \mathcal{L}_{bb{\rm sol}}$ from the top.

Triggered lepton W+3jets SecVtx+JetProb category:

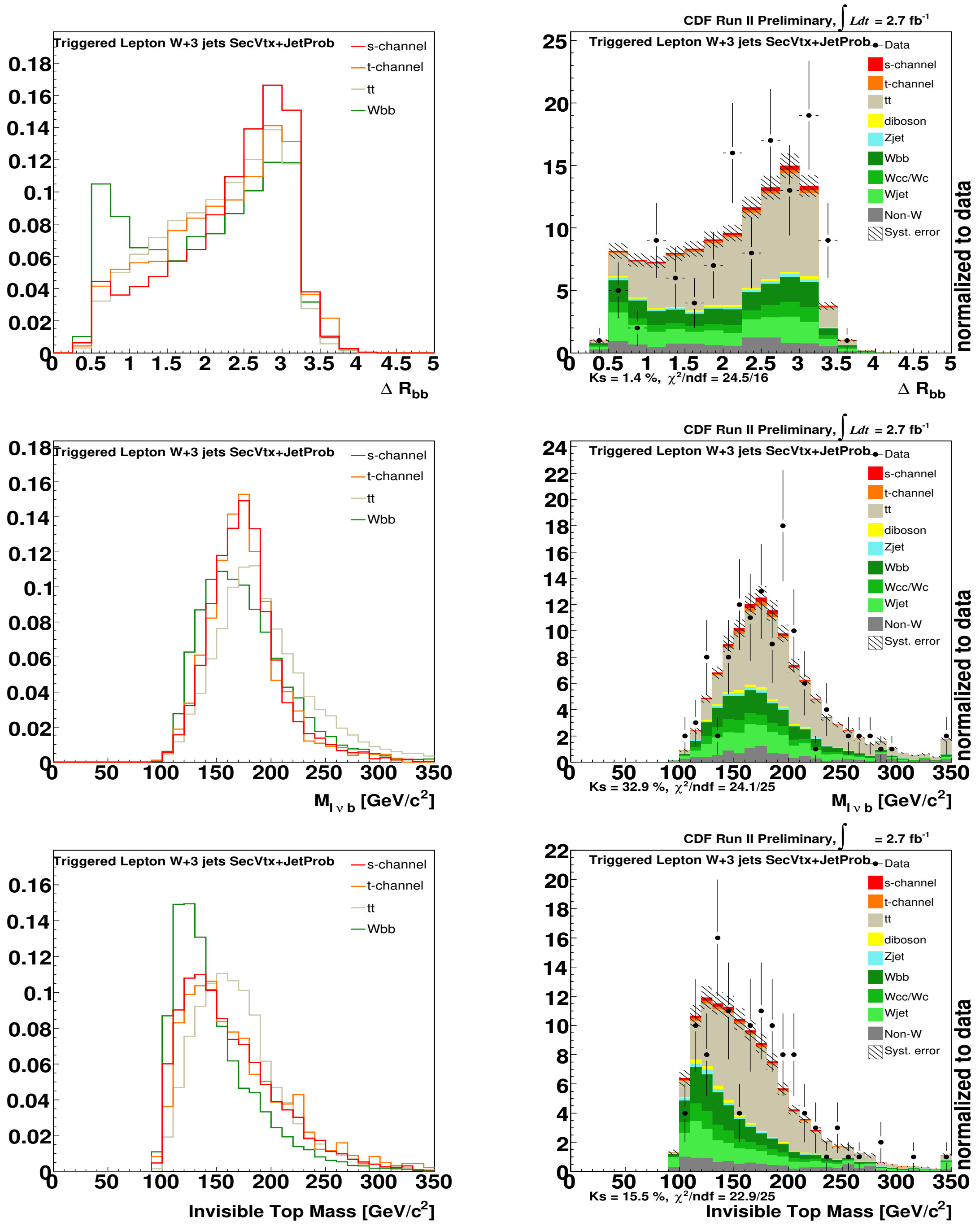

Figure 7.25: Kinematic variables shapes comparison between signal and main background(Wbb, $t\bar{t}$ and t-channel) are shown in left, and Kinematic variables shapes comparison between expected and CDF RunII data are shown in right. The variables are ΔR_{bb}, $M_{l\nu b}$ and M_{invbjj} from the top.

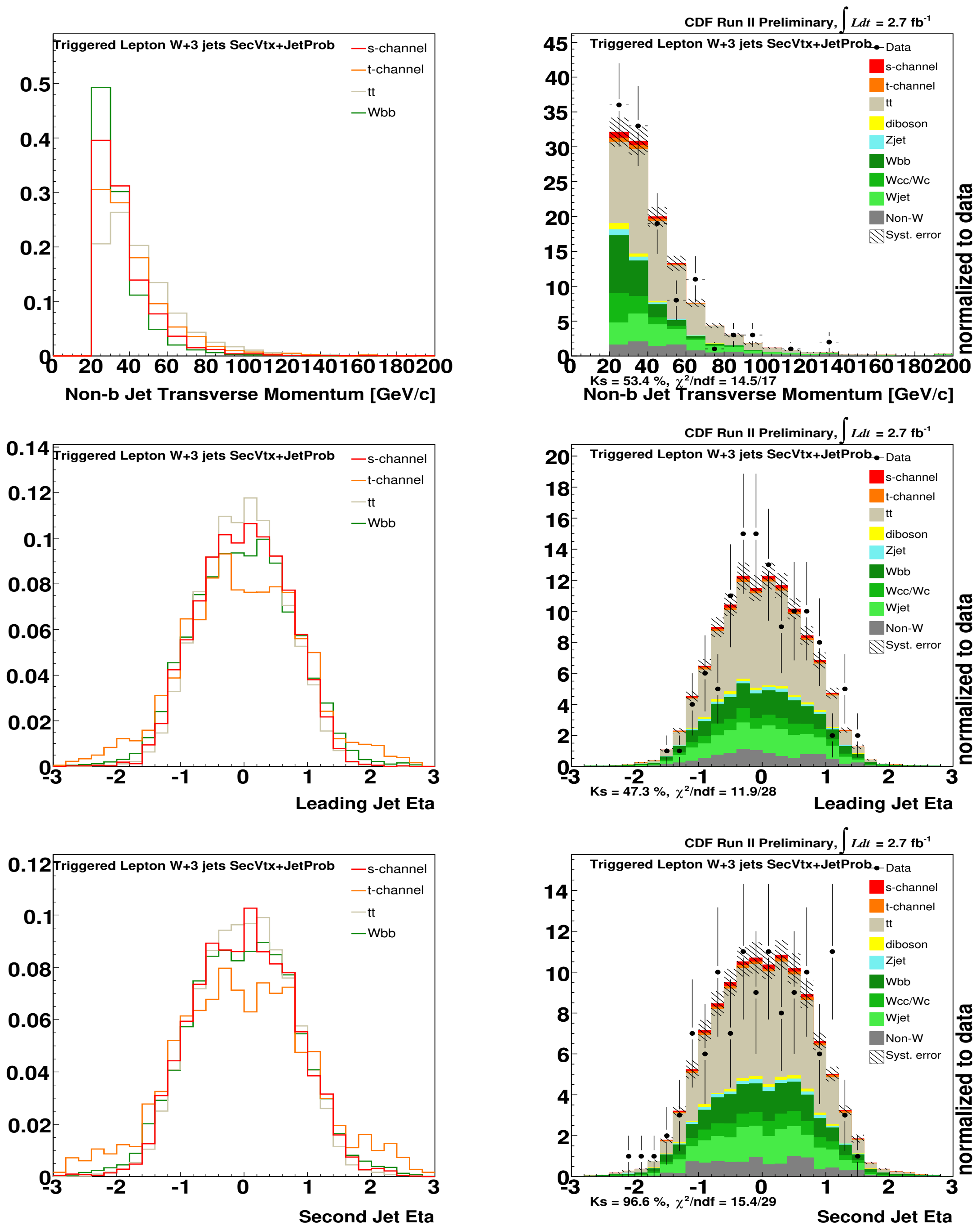

Figure 7.26: Kinematic variables shapes comparison between signal and main background(Wbb, $t\bar{t}$ and t-channel) are shown in left, and Kinematic variables shapes comparison between expected and CDF RunII data are shown in right. The variables are p_T(non-b), η(j1) and η(j2) from the top.

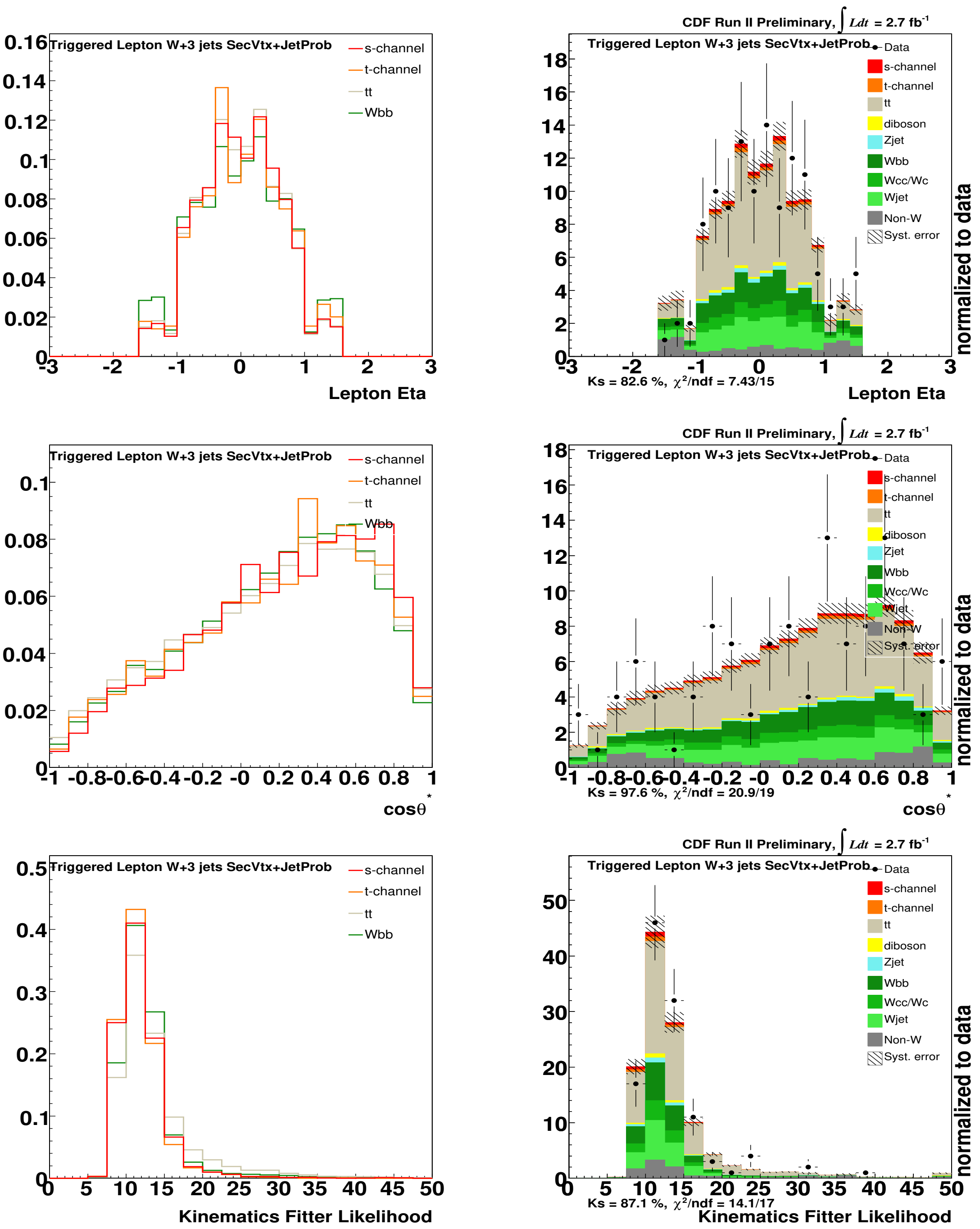

Figure 7.27: Kinematic variables shapes comparison between signal and main background(Wbb, $t\bar{t}$ and t-channel) are shown in left, and Kinematic variables shapes comparison between expected and CDF RunII data are shown in right. The variables are η(lep), $\cos\theta^*$ and $\mathcal{L}_{\nu\text{sol}} \times \mathcal{L}_{bb\text{sol}}$ from the top.

Untriggered muon W+2jets SecVtx+JetProb category:

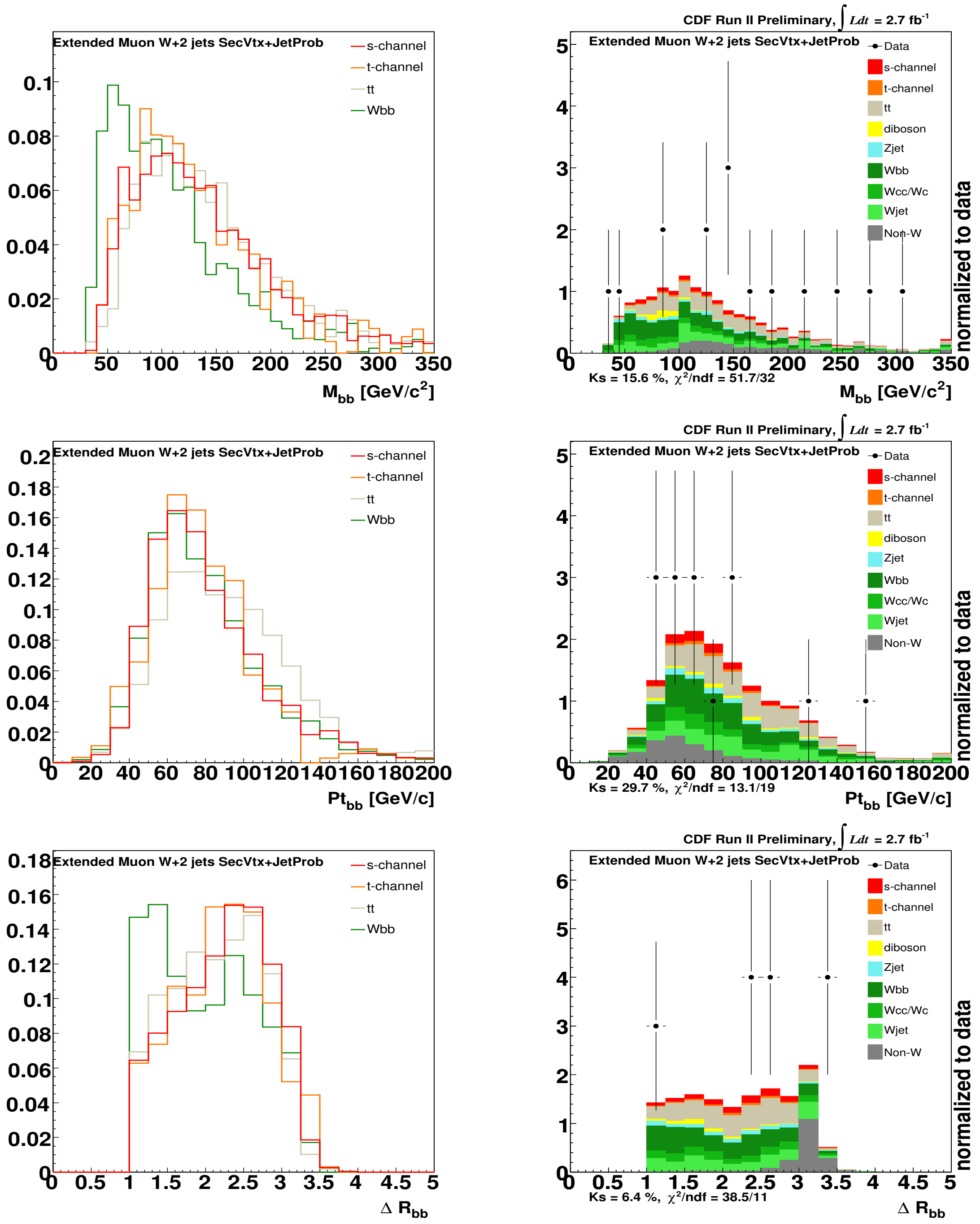

Figure 7.28: Kinematic variables shapes comparison between signal and main background(Wbb, $t\bar{t}$ and t-channel) are shown in left, and Kinematic variables shapes comparison between expected and CDF RunII data are shown in right. The variables are M_{bb}, p_{Tbb} and ΔR_{bb} from the top.

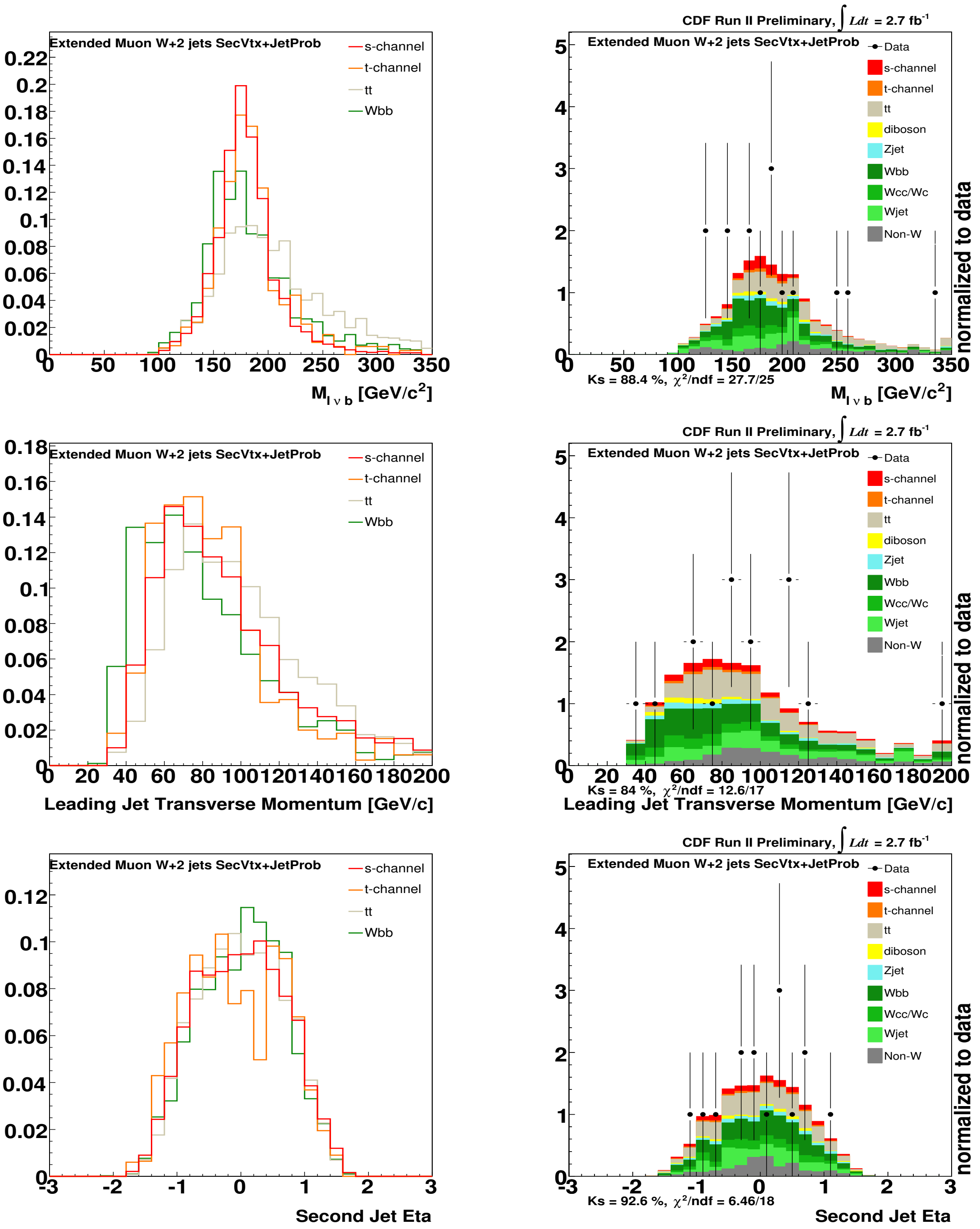

Figure 7.29: Kinematic variables shapes comparison between signal and main background(Wbb, $t\bar{t}$ and t-channel) are shown in left, and Kinematic variables shapes comparison between expected and CDF RunII data are shown in right. The variables are $M_{l\nu b}$, p_T(j1) and η(j2) from the top.

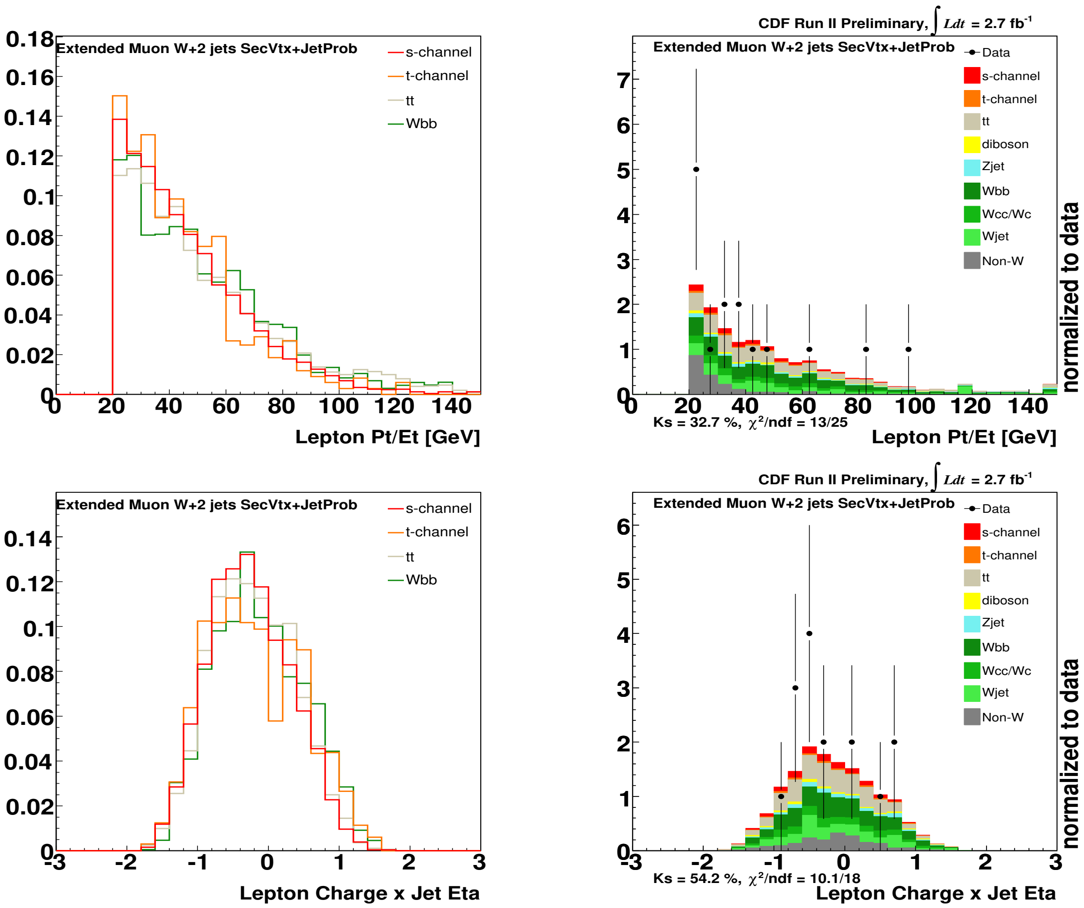

Figure 7.30: Kinematic variables shapes comparison between signal and main background(Wbb, $t\bar{t}$ and t-channel) are shown in left, and Kinematic variables shapes comparison between expected and CDF RunII data are shown in right. The variables are p_T(lep) and $Q \times \eta$ from the top.

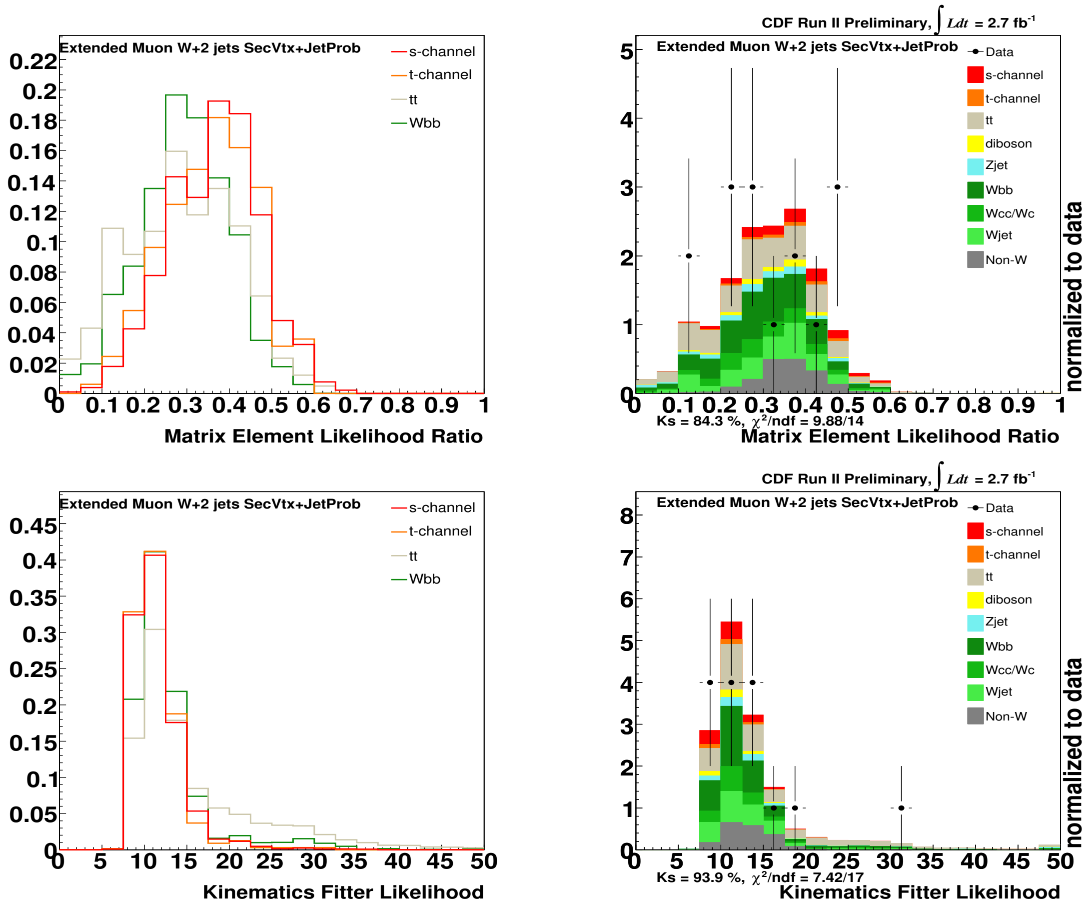

Figure 7.31: Kinematic variables shapes comparison between signal and main background(Wbb, $t\bar{t}$ and t-channel) are shown in left, and Kinematic variables shapes comparison between expected and CDF RunII data are shown in right. The variables are $\mathcal{M}_{\rm LLR}$ and $\mathcal{L}_{\nu\rm sol} \times \mathcal{L}_{bb\rm sol}$ from the top.

Untriggered muon W+3jets SecVtx+JetProb category:

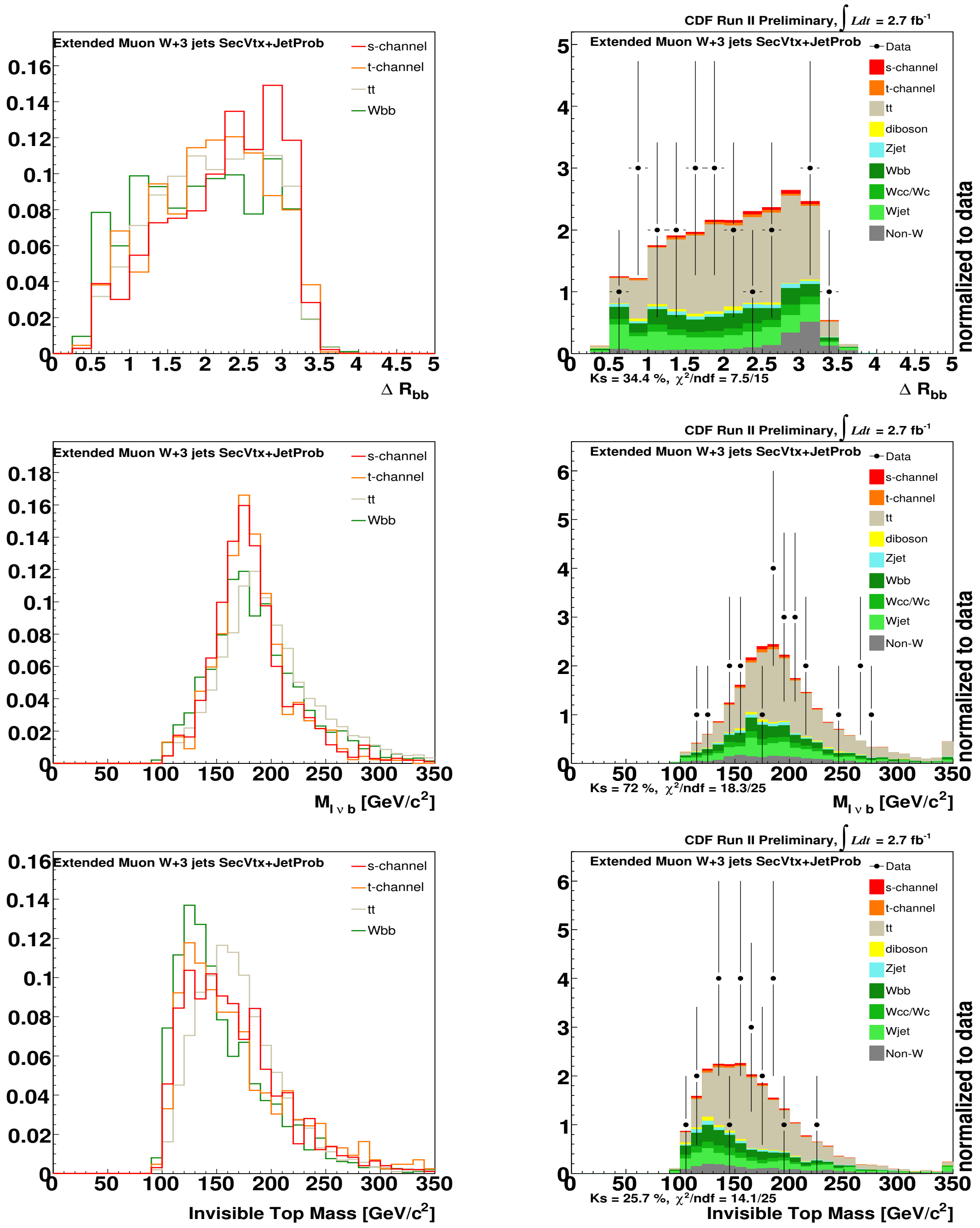

Figure 7.32: Kinematic variables shapes comparison between signal and main background(Wbb, $t\bar{t}$ and t-channel) are shown in left, and Kinematic variables shapes comparison between expected and CDF RunII data are shown in right. The variables are ΔR_{bb}, $M_{l\nu b}$ and M_{invbjj} from the top.

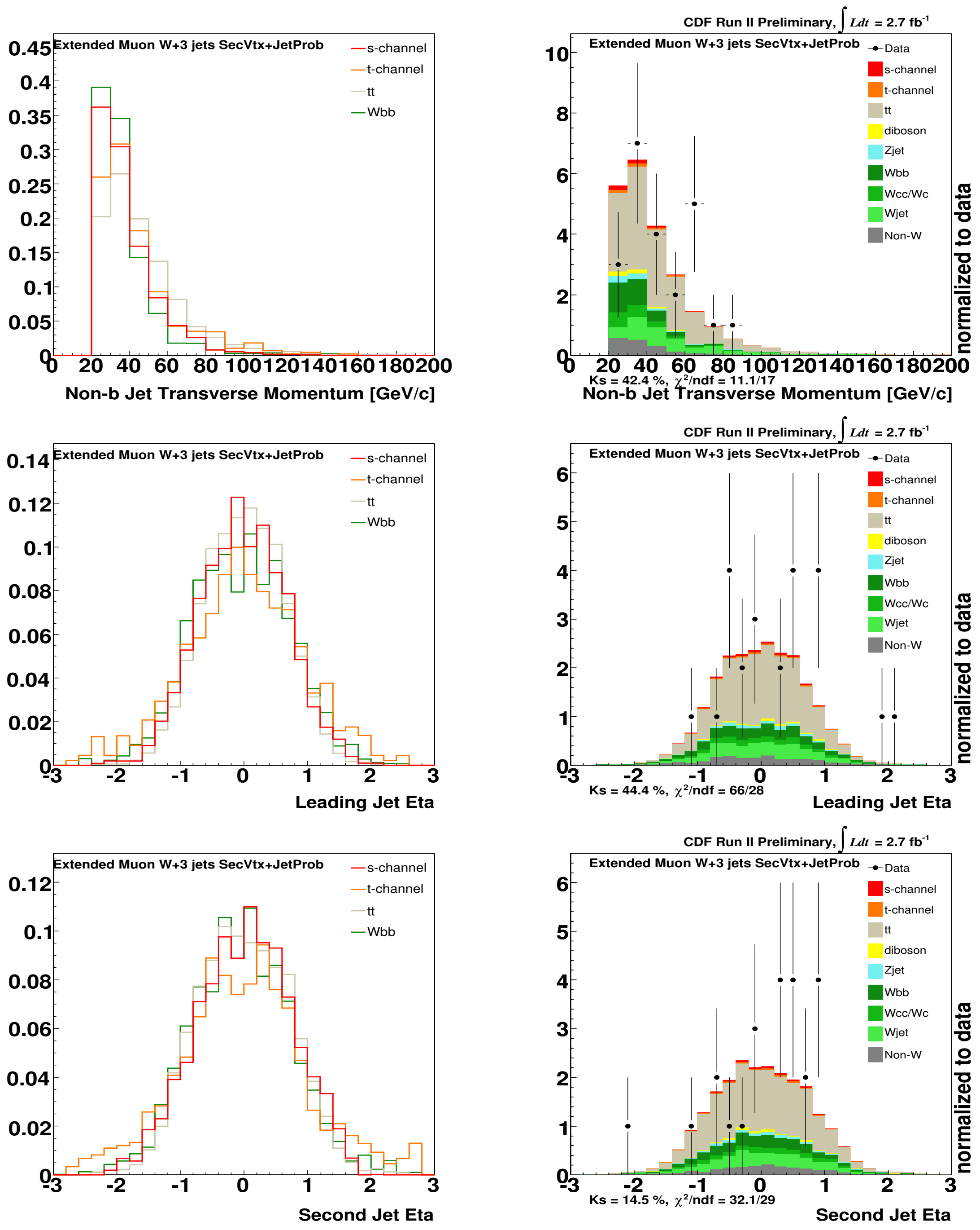

Figure 7.33: Kinematic variables shapes comparison between signal and main background(Wbb, $t\bar{t}$ and t-channel) are shown in left, and Kinematic variables shapes comparison between expected and CDF RunII data are shown in right. The variables are p_T(non-b), η(j1) and η(j2) from the top.

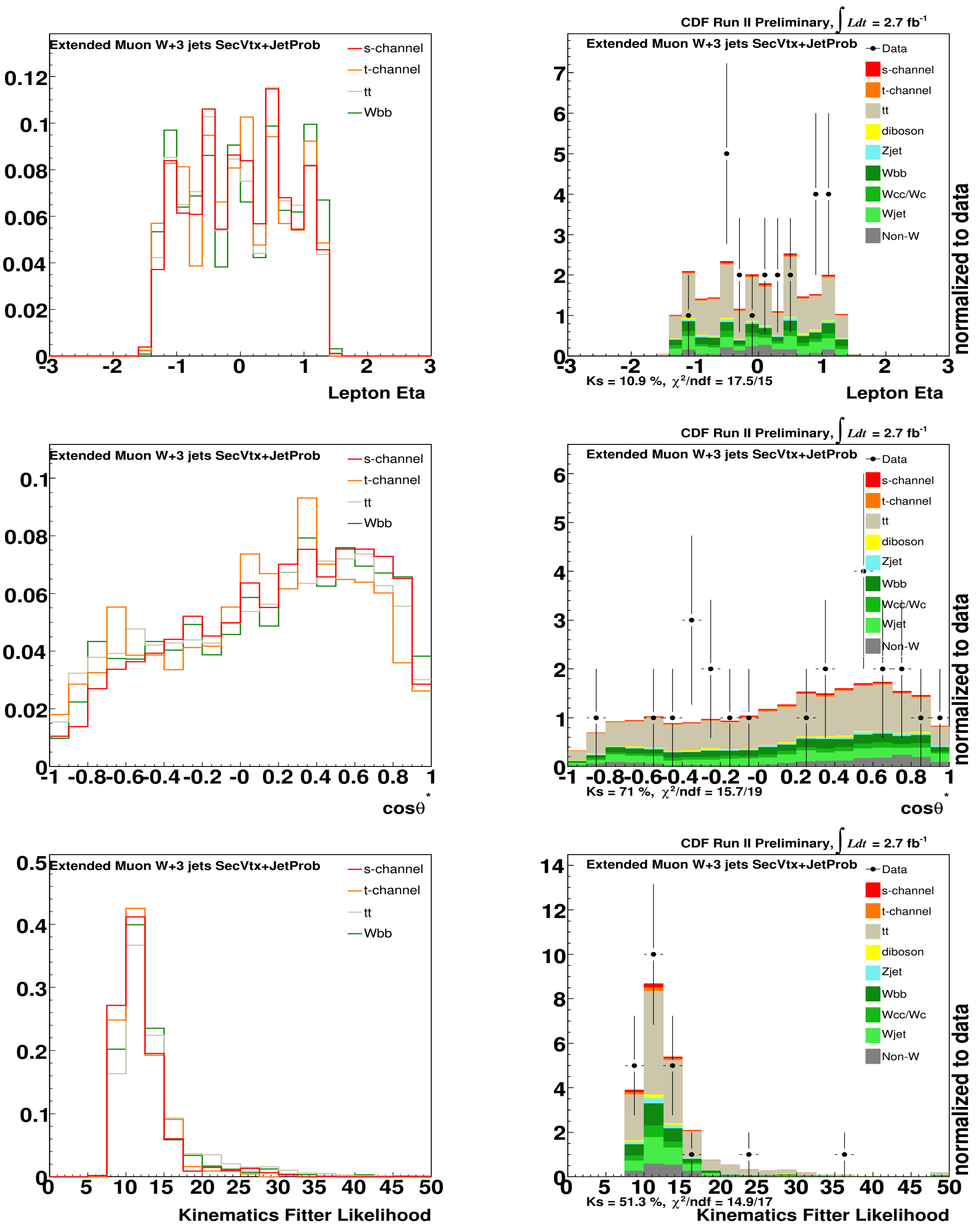

Figure 7.34: Kinematic variables shapes comparison between signal and main background(Wbb, $t\bar{t}$ and t-channel) are shown in left, and Kinematic variables shapes comparison between expected and CDF RunII data are shown in right. The variables are η(lep), $\cos\theta^*$ and $\mathcal{L}_{\nu\text{sol}} \times \mathcal{L}_{bb\text{sol}}$ from the top.

7.4 Systematic Uncertainties

The predictions of the signal and background process rates have uncertainties from the method by which they are evaluated. We address systematic uncertainty from several different sources: (1)jet energy scale, (2) initial state radiation (ISR), (3) final state radiation (FSR), (4) parton distribution function, (5) event generator, (6) uncertainty on the event detection efficiency, (7) uncertainty on the integrated luminosity, (8) ALPGEN Monte Carlo Factorization/Renormalization scale uncertainty, (9) uncertainty on the Monte Carlo Modeling. (10) uncertainty on the mistag model, Systematic uncertainties can influence on both, the expected event yield(normalization) and the shape of the discriminant distribution.

Normalization uncertainties are estimated by calculating the variation in expected event yield due to a systematic effect. The range of systematic rate and shape variation across signal and background processes are shown in Table 7.1. The prediction of the template shape are also uncertain, due to deficiencies in the Monte Carlo samples, and the imperfection in the assumptions of using control sample distributions of data which are extrapolated to predict background in the signal sample. Since the entire histogroms of the data in the selected signal region are used to extract cross section ansd significances, the shape uncertainties affect the resulting uncertainties of the results strongly.

The background rates are constrained by the low signal-to-background portions of the discriminant histograms, and if the shapes are well known, these rates are easily converted into predictions in the high-score bins. But this is an extrapolation and shape uncertainties reduce our confidence in the predictions of the backgrounds in the high-score regions even though they are well known and modeled in the low score regions.

Some of the Monte Carlo based shape uncertainties can be estimated from prior guidelines for variation of the parameter of the prediction, such as ISR, FSR, M_T, PDF and Q^2 uncertainties, while others arise from the observation of mismodeling of specific variables in the data. Since the observed ΔR_{bb}, Pt_{bb}, ηlep and M_{WT} shapes for our control sample, which have no b-tagged jet, have a small excess, we also included the shape systematics for them. The shape variation uncertainty from nonW mismodeling is estimated using jet-electron sample described in Section 4.6.

Figure B.1- B.9 shows the shape systematic uncertainty for tight lepton 2jet double SecVtx category in appendix. The bin-by-bin relative variations are used as shape systematics in the likelihood function. The letter "$\surd$" in Table 7.1 indicates that a shape systematic uncertainty has been evaluated for the particular nuisance parameter and included in the likelihood function. For all backgrounds the normalization uncertainties are represented by the uncertainty on the predicted number of background events and are incorporated in the analysis as Gaussian contributes $G(\beta|1,\Delta_j)$ in the likelihood function [49] :

$$\mathcal{L}(\beta_1,...,\beta_5;\delta_1,...,\delta_{10}) = \prod_{k=1}^{B} \frac{e^{-\mu_k}\cdot\mu_k^{n_k}}{n_k!} \cdot \prod_{j=2}^{5} G(\beta_j|1,\Delta_j)\cdot\prod_{j=1}^{10} G(\delta_j,0,1) \tag{7.6}$$

where,

$$\mu_k = \sum_{j=1}^{5}\beta_j \cdot \left\{\prod_{j=1}^{12}(1+|\delta_i|\cdot(\epsilon_{ji+}H(\delta_i)+\epsilon_{ji-}H(-\delta_i)))\right\} \tag{7.7}$$

$$\cdot \;\; \alpha_{jk}\cdot\left\{\prod_{i=1}^{12}(1+|\delta_i|\cdot(\kappa_{jik+}H(\delta_i)+\kappa_{jik-}H(-\delta_i)))\right\} \tag{7.8}$$

The systematic normalization and shape uncertainties are incorporated into the likelihood as nuisance parameters, conforming with a fully Bayesian treatment [48]. We take the correlation between normalization and shape uncertainties for a given source into account. The relative strength of a systematic effect due to the source i is parameterized by the nuisance parameter δ_i in the likelihood function, constrained to a unit-width Gausian(last term in Equation 7.6). The $\pm1\sigma$ changes in the normalization of process j due to the i^{th} source of systematic uncertainty are denoted by ϵ_{ji+} and ϵ_{ji-} (see Equation part 7.7). The $\pm1\sigma$ changes in bin κ of discriminant templates for process j due to the i^{th} source of systematic uncertainty are quantified by κ_{jik+} and κ_{jik-} (see Equation part 7.8). H(δ_i) represents the Heaviside function, defined as H(δ_i)=1 for δ_i >0 and H(δ_i)=0 for δ_i <0. The Heaviside function is used to separate positive and negative systematic shifts (for which we have different normalization and shape uncertainties). The variable δ_i appears in both the term for the normalization (Equation 7.7) and the shape uncertinaty (Equation 7.8), which is how correlations between both effects are taken into account. We reduce the likelihood function to the parameter of interest (single top cross-section) by the standard Bayesian marginalizing procedure [1]

7.5 Expected Sensitivity and Hypothesis Test

We interpret the result using CLs/CLb method developed at LEP [47]. We compare our data against two models, one asserting that the data is due to background processes only (b) and one which includes StandardModel single top production in addition to the background processes (s+b). We propagate all systematic uncertainties in our statistical method. Using the test statistic $Q = \frac{\mathcal{L}(data|s+b)}{\mathcal{L}(data|b)}$ we compute the probability (p-value) that the background only model (b) fluctuated equal or up to the observed value Q_{obs} in the data (observed p value) and to the median Q value of signal+background (s+b) pseudo-experiment (expected p-value). Figure 7.35 shows the distribution of the test statistics for pseudo-experiments performed for (b) and (s+b). Top 8 figures show the null and test statistics distribution for each categories listed below.

Table 7.1: Systematic uncertainties for the total prediction normalization estimated across all different processes and analysis input channels. the $\surd$ indicates that a template shape uncertainty has been evaluated for that particular nuisance parameter and has been included in the likelihood function.

CDF RUN II Preliminary, L=2.7 fb^{-1}

Source	Rate Uncertainties for expected events	shape variation
Jet Energy Scale	4.7 %	$\surd$
Initial State Radiation	1.7 %	$\surd$
Final State Radiation	1.3 %	$\surd$
Parton Distribution Fanction	0.5 %	$\surd$
MC generator	0.5 %	
Event Selection Acceptance	1.5 %	
Integrated Luminosity	6.0 %	
Theoritical Cross Section	3.1 %	
Top Quark Mass	2.3 %	$\surd$
Data Based Background Estimation	23 %	
Mistag Modeling	n/a	$\surd$
QCD Modeling	n/a	$\surd$
Q^2 scale in Alpgen MC	n/a	$\surd$
MC Mismodeling	n/a	$\surd$

- Triggered lepton, W+2jet-bin, SecVtx + SecVtx tagged
- Triggered lepton, W+2jet-bin, SecVtx + JetProb tagged
- Triggered lepton, W+3jet-bin, SecVtx + SecVtx tagged
- Triggered lepton, W+3jet-bin, SecVtx + JetProb tagged
- Untriggered muon, W+2jet-bin, SecVtx + SecVtx tagged
- Untriggered muon, W+2jet-bin, SecVtx + JetProb tagged
- Untriggered muon, W+3jet-bin, SecVtx + SecVtx tagged
- Untriggered muon, W+3jet-bin, SecVtx + JetProb tagged

We estimated significance for each of categories, and then combined them. Finally, we obtained the expected p-value of $\sim 0.14^{+0.34}_{-0.12}$corresponding to a Gaussian significance of $1.10^{+1.06}_{-1.03}$ σ standard deviations.

We also obtained the expected 95 % C.L. upper limit for the single top s-channel cross section. The expected 95 % C.L. upper limit is $\sim$ 1.61 pb. The distribution is shown in Figure 7.36. This expected upper limit of the cross section is 1.9 times Standerd Model theoretical expectation.

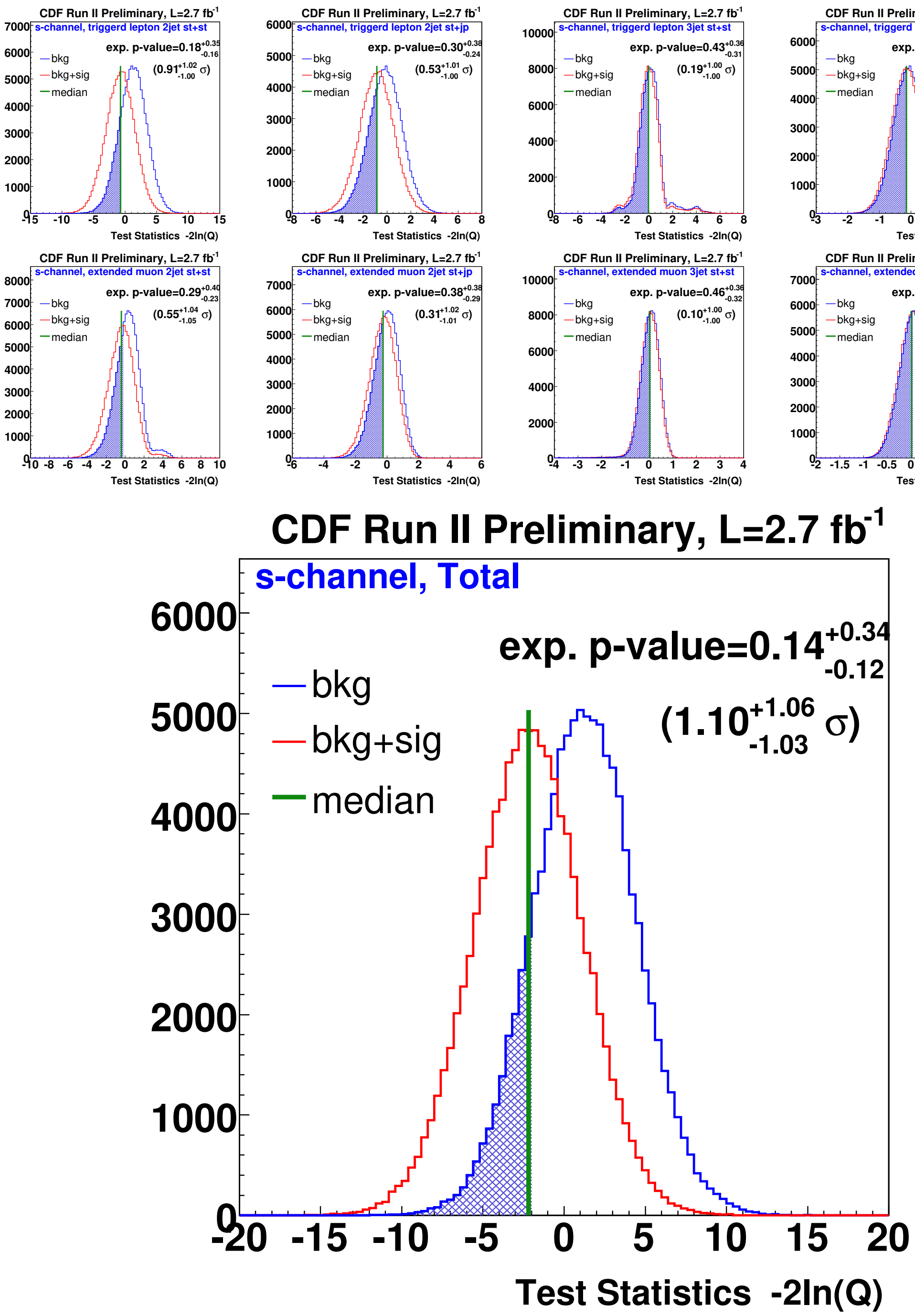

Figure 7.35: Distribution of the test statistics $Q = \frac{\mathcal{L}(data|s+b)}{\mathcal{L}(data|b)}$ for the singletop+background hyposhesis and the background only hypothesis in 10000 pseudo-experiments. Top 8 histgram show sensitivities for the each category. Bottom histgram shows combined result. The grean line shows the median of the sig+bkg hypothesis which is used to determine the expected p-value.

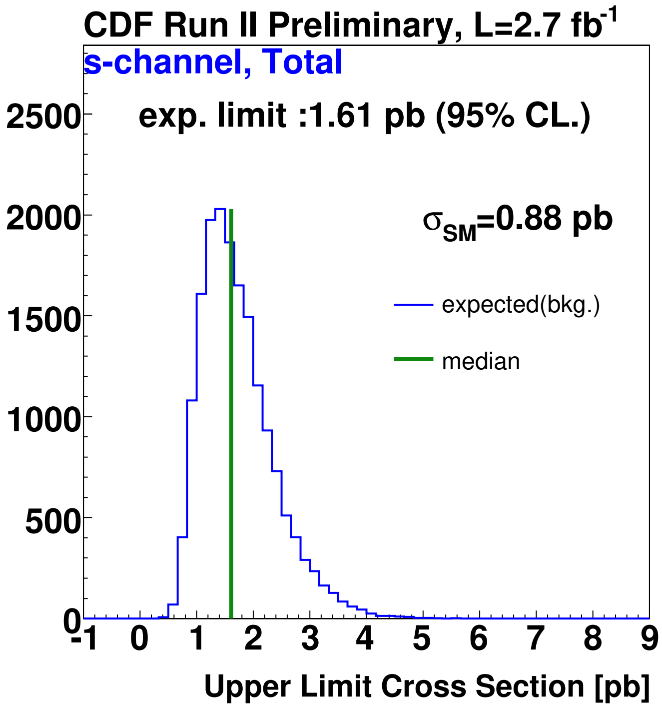

Figure 7.36: 95% C.L. upper limit for the s-channel single top quark production cross section in 10000 pseudo-experiments.

Chapter 8

Results and Discussions

8.1 Results in s-channel analysis

We analyzed to 2.7 fb^{-1} of CDF Run II Data. We predicted 26 events of single top s-channel signal over the 570 background events. The distributions of likelihood discriminant, which was described in Chapter 7 Eq. 7.4, are shown in Figure 8.1.

Cross Section Measurement

Figure 8.2(left) shows the likelihood distribution in the data with 68% region marked to show the uncertainty. The single top quark s-channel production cross section was measured to be $2.38^{+1.01}_{-0.84}$ pb. Figure 8.2(right) is the break down of each category, described in Section 7.5. This analysis is performed under the assumption that the top quark mass is 175 GeV/c^2 .

Measurement of $|V_{tb}|$ and Limit

The CKM matrix element $|V_{tb}|$ can be calculated very simply. Because the cross section is proportional to the square of V_{tb}, $|V_{tb}|$ is just the square root of the measured cross section divided by the expected cross section from the Standard Model, shown in Eq. 1.3. Since t-channel cross section is proportional to the $|V_{tb}|^2$ as well as s-channel, $|V_{tb}|$ is calculated from s- plus t-channel cross section from two b-tagged events, which include s-channel fraction more than 70%. This gives a result of $|V_{tb}|$=$1.43^{+0.38}_{-0.26}$(experimental) $\pm$ 0.11(theory). Because this measurement relies on the theoretical cross section of single top production, it must include the uncertainty on the cross section calculation, which is quoted here as the theoretical uncertainty.

It is also possible to set a lower limit on $|V_{tb}|$. A flat prior is assumed in $|V_{tb}|^2$, which is proportional to the measured cross section, and it is required to lie between zero and one inclusive. The likelihood must now be modified to include the systematic uncertainties on the

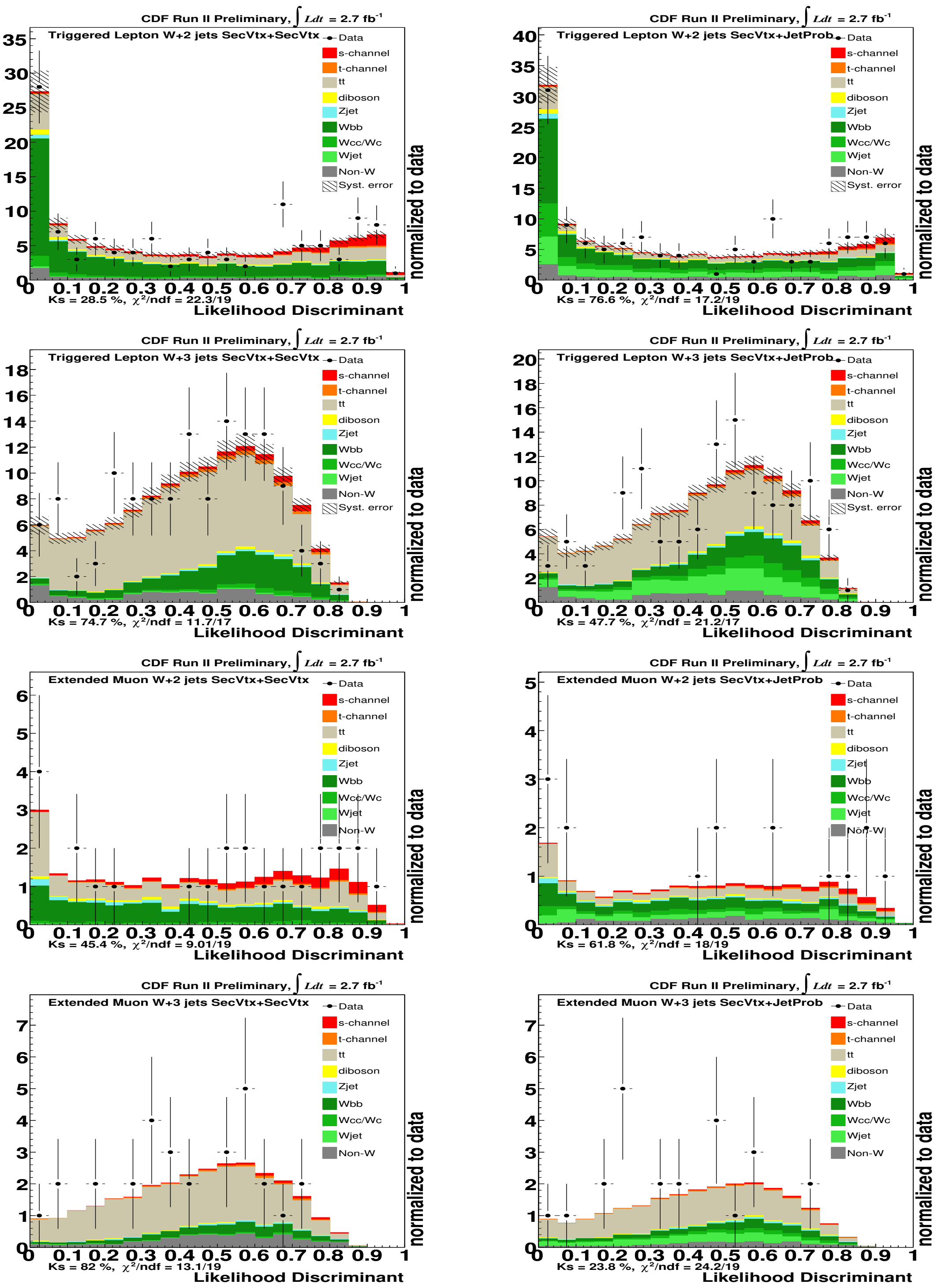

Figure 8.1: Distribution of the discriminant for data and Monte Carlo. Left figure is double SecVtx category and right figure shows SecVtx and JetProb b-tag category. The insert shows a zoom in the signal region, Discriminant> 0.3.

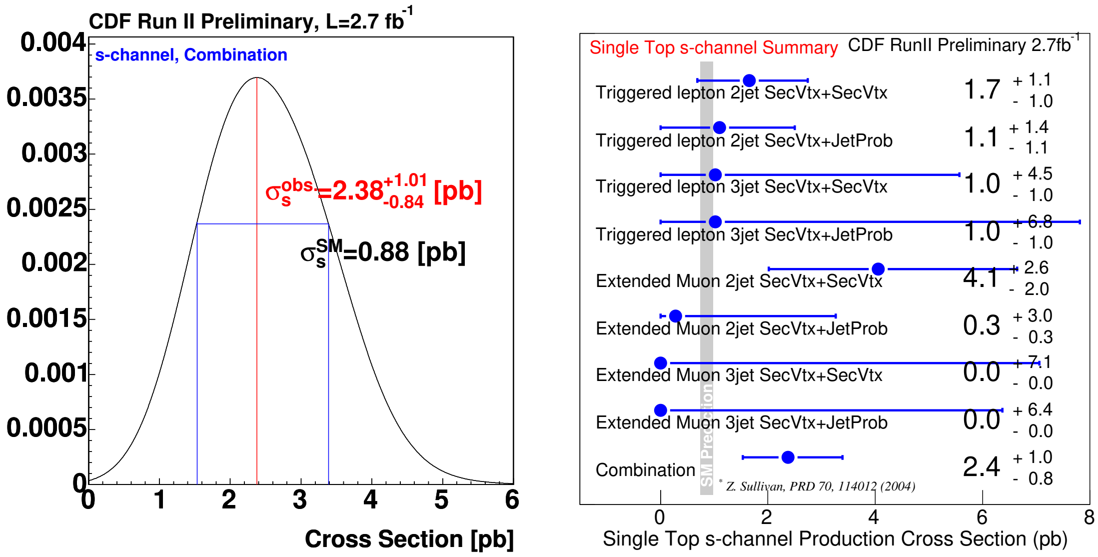

Figure 8.2: Left: Cross section result using 2.7 fb$^{-}1$ of CDF II data. The error band shows the 68% uncertainty (all systematics included) on the measurement. Right: The break down of each category.

single top production cross section and the top quark mass. This likelihood curve, shown in Figure 8.3, is then integrated from one, the maximum allowed value, until the area covered includes the desired percentage of the total area under the likelihood curve. Conventionally, limit are quoted at 95% C.L., so the curve is integrated until 95% of the area is included. This sets a lower limit on $|V_{tb}|$ of 0.53. Checks with pseudo-experiments show that this limit gives proper frequentist coverage.

Significance and Cross Section Upper Limit

The p-value of this measurement is obtained from the distribution of $-2\ln Q$, plotted in Figure 8.4. This measurement gives a p-value of 0.003. It is customary to interpret this probability as a number of standard deviation from the mean of a Gaussian distribution, integrated from the center of distribution. In this case, the measured significance corresponds to 2.7 standard deviations in Gaussian statistics.

The 95 % C.L. upper limit for the s-channel production cross section is set to $\sigma_s = 4.15$ pb assuming null signal, as shown in Figure 8.5.

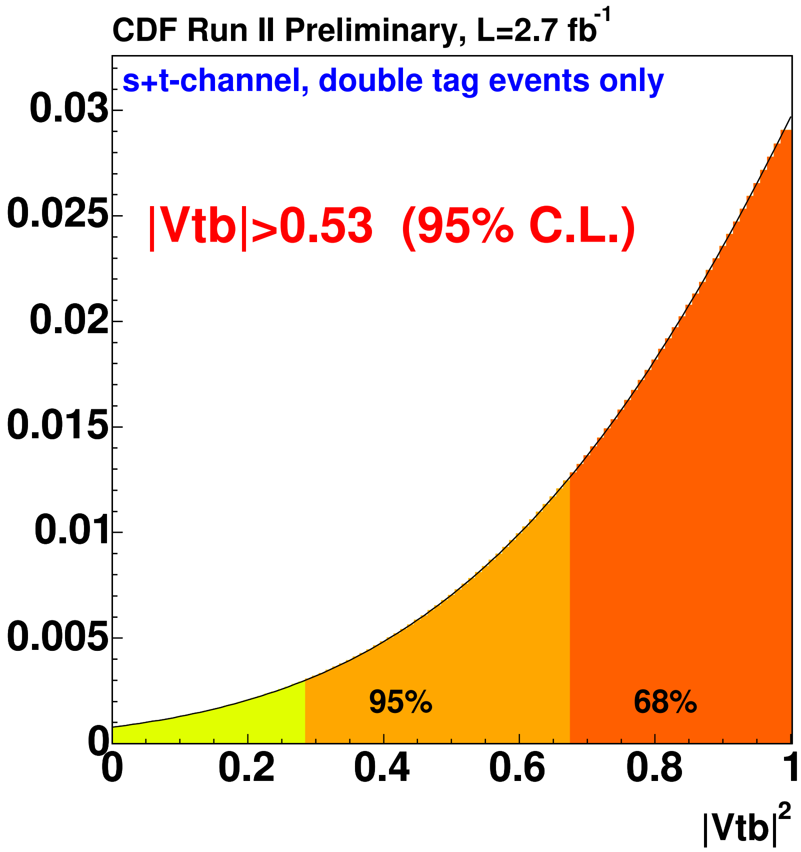

Figure 8.3: The likelihood in $|V_{tb}|^2$ used to set a 95% lower limit on the value of $|V_{tb}|$.

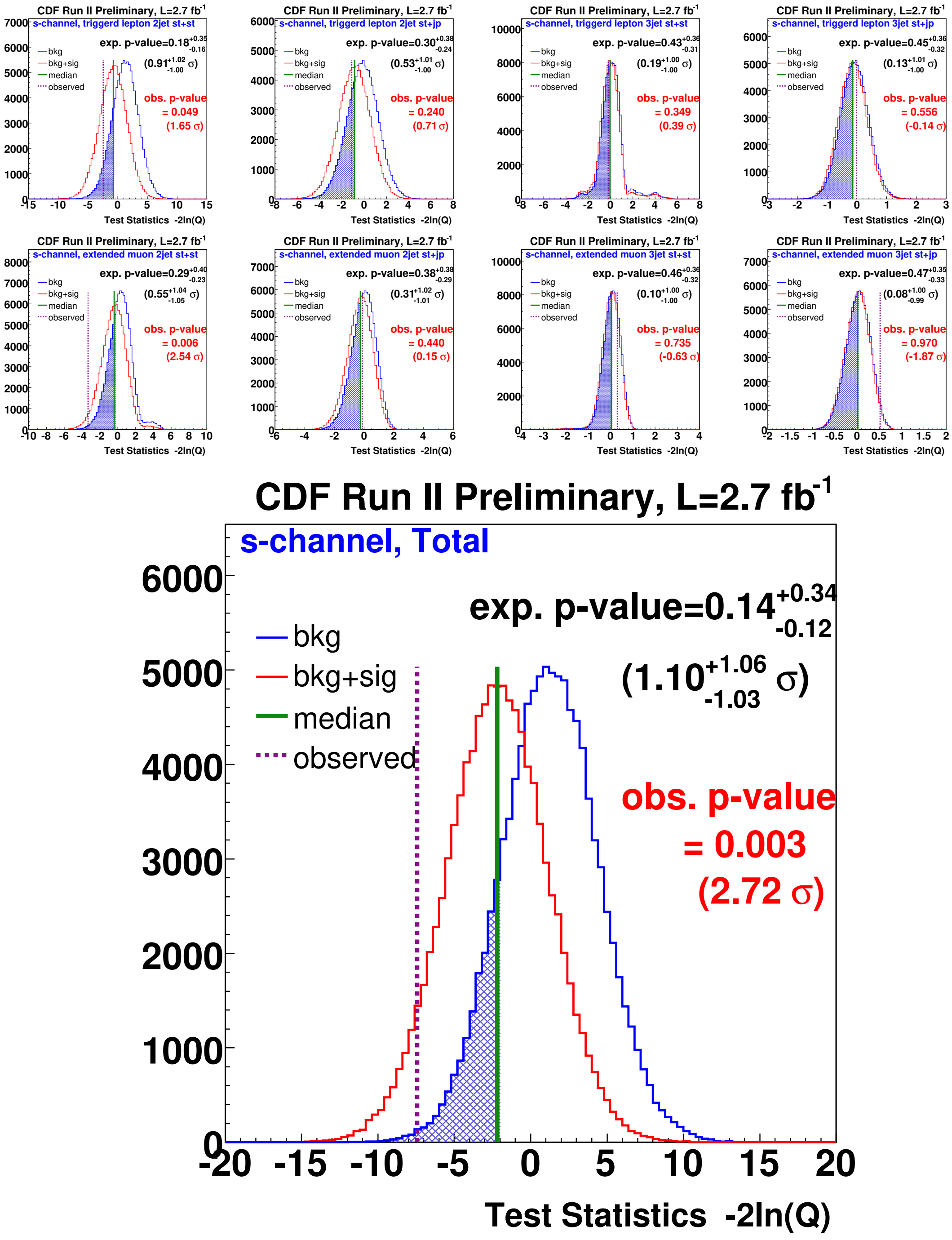

Figure 8.4: Distribution of the test statistics $Q = \frac{\mathcal{L}(data|s+b)}{\mathcal{L}(data|b)}$ for the singletop+background hyposhesis and the background only hypothesis in 10000 pseudo-experiments. The grean line shows the median of the sig+bkg hypothesis which is used to determine the expected p-value.

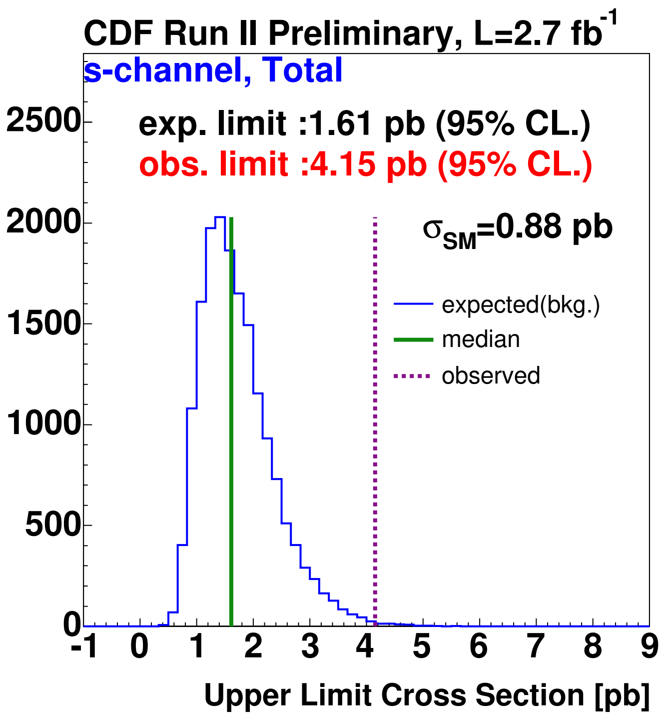

Figure 8.5: 95% CL. upper limit for the s-channel single top quark production cross section.

8.2 Results in s- and t-channel analysis

We also perform t-channel optimization search with similar likelihood method discriminant, L_t, method analysis described in [17]. As described in section 1.4, the final state of the single top quark t-channel production has only one b-quark typically, since b-quark jet produced by gluon splitting may be contained inside the beam pipe. On the other hand the final state of the single top quark s-channel production has two b-quark typically.

We perform s- and t-channel cross section fit simultaneously to evaluate s- and t-channel cross section separately. We used L_t discriminant described in [17] [50] for one SecVtx b-tagged category and L_s discriminant described in section 7.3 for double b-tagged category as following,

- triggered lepton, W+2jet, one SecVtx b-tagged sample... L_t
- triggered lepton, W+3jet, one SecVtx b-tagged sample... L_t
- triggered lepton, W+2jet, two SecVtx b-tagged sample... L_s
- triggered lepton, W+3jet, two SecVtx b-tagged sample... L_s
- extended muon, W+2jet, two SecVtx b-tagged sample ... L_s
- extended muon, W+3jet, two SecVtx b-tagged sample ... L_s
- extended muon, W+2jet, one SecVtx and one JetProb b-tagged sample ... L_s
- extended muon, W+3jet, one SecVtx and one JetProb b-tagged sample ... L_s

As a result, we obtained the likelihood fit estimate for the simultaneous s- and t-channel production cross section measurement shown in Figure 8.6. The cross section values are $\sigma_s = 1.9^{+0.9}_{-1.0}$ pb and $\sigma_t = 1.2^{+0.8}_{-0.7}$ pb with 1σ(green) and 2σ(yellow) uncertainty. The uncertainty of each production cross sections are calculated by projecting to the each axis. The theoretical prediction with beyond the Standard Model is also illustrated in Figure. 8.6(blue point). The points for the top-quark-flavor model as the $\times$, the FCNC Z-t-c vertex as the open circle, a model with a charged top-quark pion as the cross, and a four quark generation scenario as the asterisk are indicated. t-channel cross sections for these points are linearly extraporated to the NLO calculated cross section.

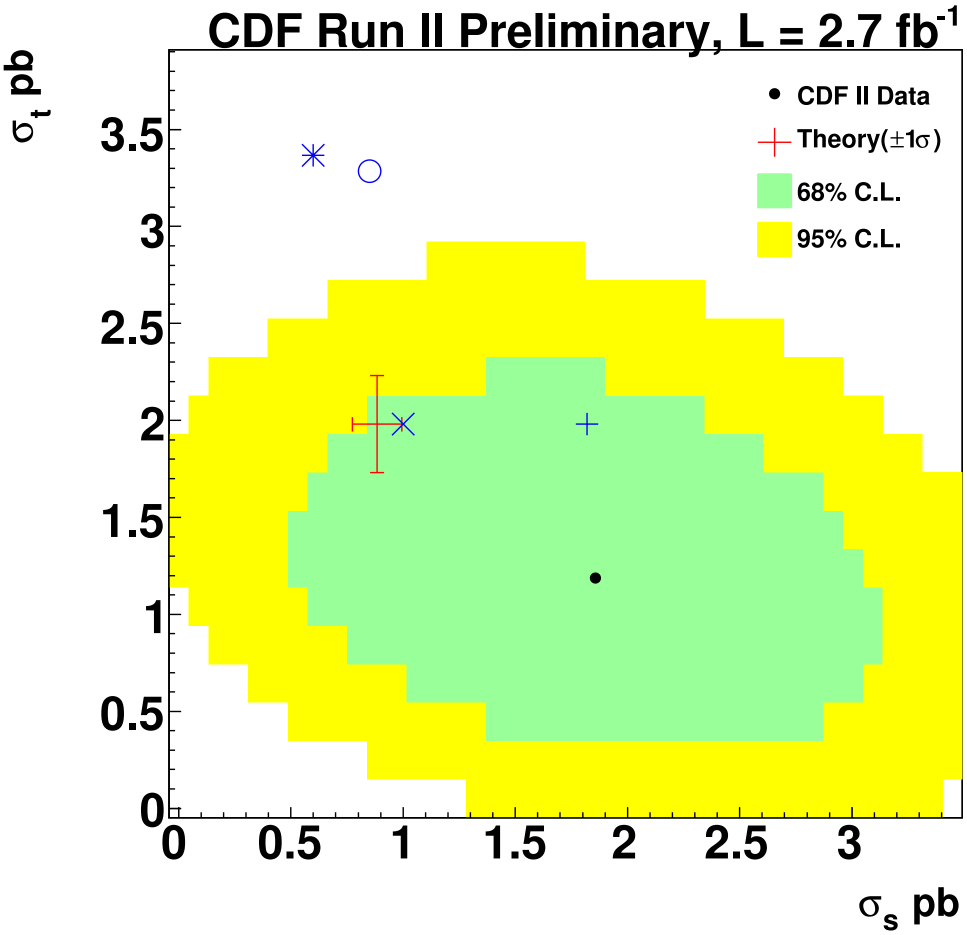

Figure 8.6: The single top quark production cross section in the σ_s and σ_t plane. The best fit cross section(black dot) and it's 1σ(green) and 2σ(yellow) uncertainty. Red mark shows theoretical cross section with uncertainty. Blue points shows the cross section point with beyond the Standard Model processes shown in Figure. . The points for the top-quark-flavor model as the $\times$, the FCNC Z-t-c vertex as the open circle, a model with a charged top-quark pion as the cross, and a four quark generation scenario as the asterisk. t-channel cross sections for these points are linearly extraporated to the NLO calculated cross section. All models assumes typical parameter points described in [18].

Chapter 9

Conclusion

The measurement of the cross section of single top quark production at CDF is a challenging task, requiring a good understanding of the detector, careful simulation, detailed studies of background processes, sophisticated techniques for separating the signal from the background, and a rigorous statistical treatment. We have searched for s-channel single top quark production using double b-tag method together with likelihood based signal background separator technique. We have analyzed 2.7 fb^{-1} of CDF Run II data. The result of this analysis is the world's most sensitive measurement of single top s-channel cross section. We measured a cross section to be

$$\sigma_s = 2.38^{+1.01}_{-0.84} \text{ pb},$$

which correspondts to the CKM matrix element value of

$$|V_{tb}| = 1.43^{+0.38}_{-0.26}(\text{experimental}) \pm 0.11(\text{theory}).$$

The probability that this result comes from a fluctuation from the background-only hypothesis (p-value) is 0.003, which corresponds to 2.7 standard deviations in Gaussian statistics. The expected p-value calculated in pseudo-experiments including single top quark production signal for this analysis is $0.14^{+0.34}_{-0.12}$, which corresponds to $1.10^{+1.06}_{-1.03}$ standard deviation in Gaussian statistics. The upper limit at 95% C.L. for the single top s-channel production cross section is 4.15 pb. The expected upper limit at 95% C.L. for the single top s-channel production cross section assuming null singal is 1.61 pb.

We have also measureded the s- and t-channel production cross sections simultaneously. The simultaneous fit of s- and t-channel production cross section yield $\sigma_s = 1.9^{+0.9}_{-1.0}$ pb and $\sigma_t = 1.2^{+0.8}_{-0.7}$ pb. The uncertainty on each production cross sections are calculated by projecting to each axis.

The single top s-channel cross section has now been measured with the smallest uncertainty in the world. This result will be combined together with other measuerment at CDF [50], soon. The precision will be improved with more data: the Tevatron has delivered more than 5.8 fb^{-1} of integrated luminosity by now, of which nearly 4 fb^{-1} are available for analysis by each of CDF

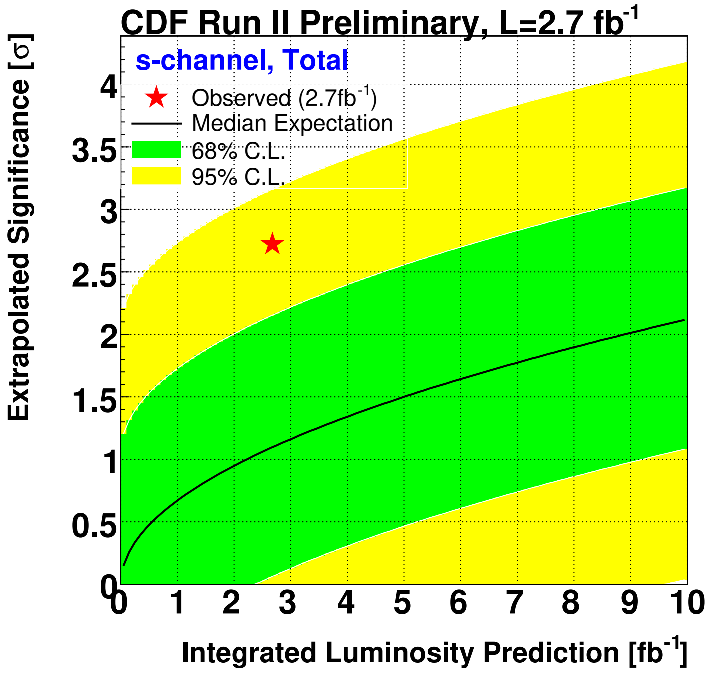

Figure 9.1: Extraporated significance as a function of CDF Luminosity. Solid line shows extraporated significance. Green and yellow region is 1 σ and 2 σ band respectively.

and DØ . The extraporation in the future for this analysis is shown in Figure 9.1 as a function of CDF Luminosity.

Future analyses will focus on reducing systematic uncertainties, some of which are currently conservative. In addition, the sample is becoming large enough to measure polarization of the top quarks produced in this channel (predicted by the Standard Model to be nearly 100%).

Appendix A

Shape Comparison for the Control Sample

To confirm the methodology for this analysis, we checked all input valiables for the control sample, whose events have only one SecVtx b-tagged jet. In this chapter, we show the kinematic shapes of the input valiables compared between signal and main backgrounds for the control sample. Also shown are expected and CDF RunII data shapes. The plots are shown separately for event the different categories as listed in Section 7.3.

Triggered lepton W+2jets one SecVtx tag category:

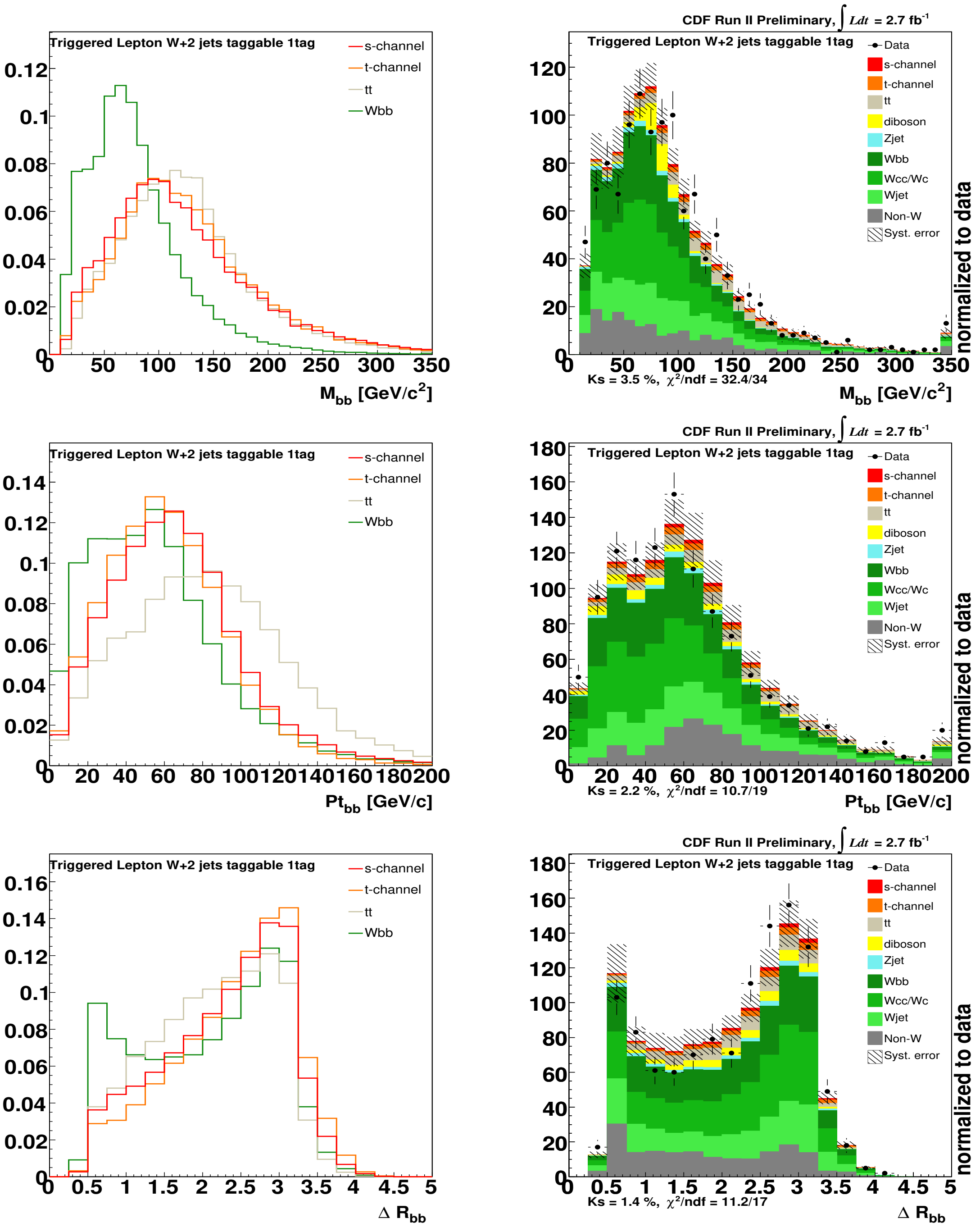

Figure A.1: Kinematic variables shapes comparison between signal and main background(Wbb, $t\bar{t}$ and t-channel) are shown in left, and Kinematic variables shapes comparison between expected and CDF RunII data are shown in right. The variables are M_{bb}, p_{Tbb} and ΔR_{bb} from the top.

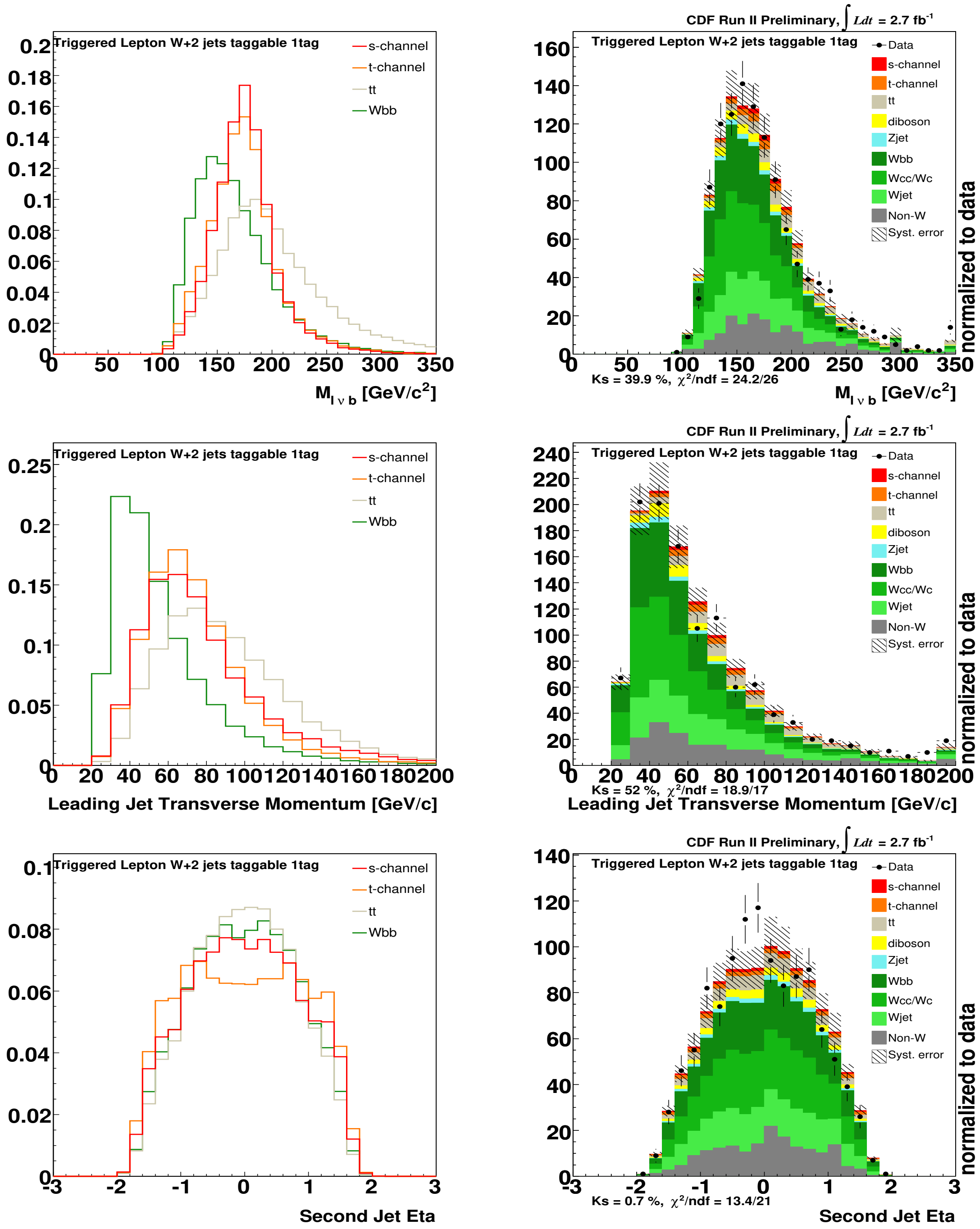

Figure A.2: Kinematic variables shapes comparison between signal and main background(Wbb, $t\bar{t}$ and t-channel) are shown in left, and Kinematic variables shapes comparison between expected and CDF RunII data are shown in right. The variables are $M_{l\nu b}$, p_T(j1) and η(j2) from the top.

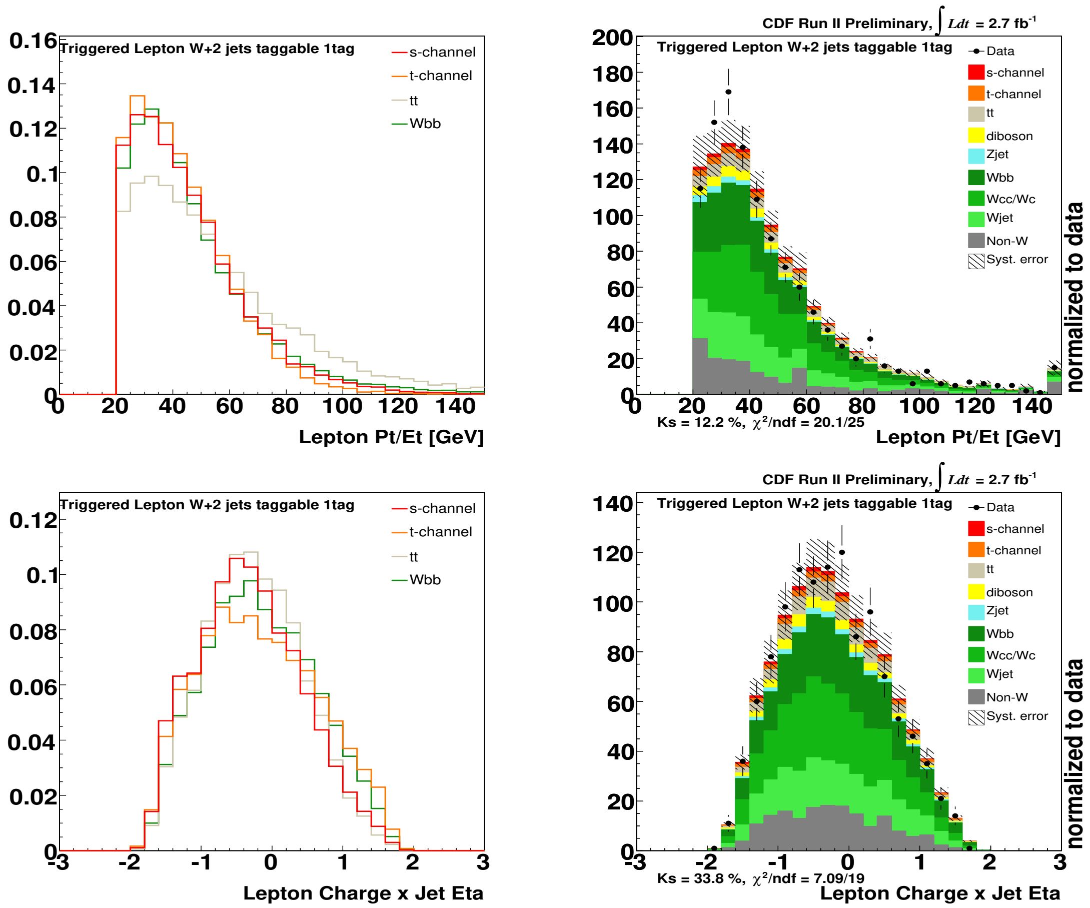

Figure A.3: Kinematic variables shapes comparison between signal and main background(Wbb, $t\bar{t}$ and t-channel) are shown in left, and Kinematic variables shapes comparison between expected and CDF RunII data are shown in right. The variables are p_T(lep) and $Q \times \eta$ from the top.

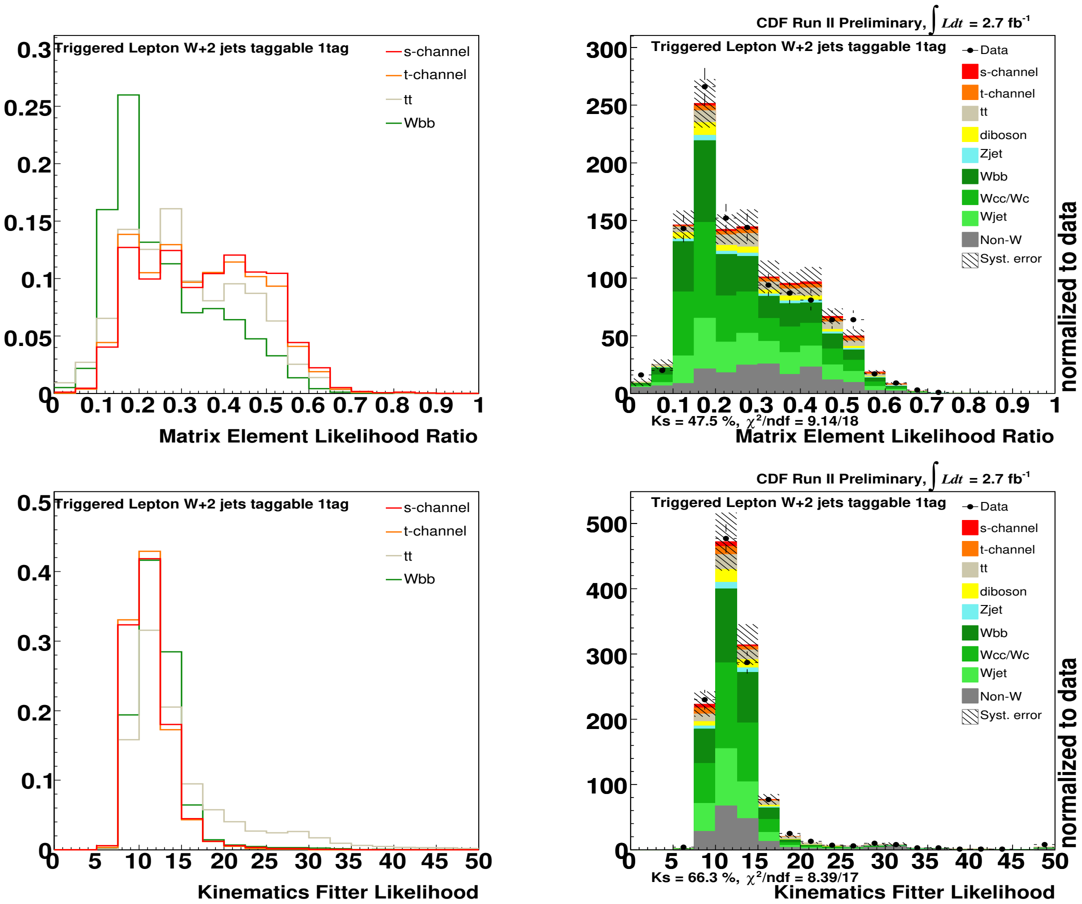

Figure A.4: Kinematic variables shapes comparison between signal and main background(Wbb, $t\bar{t}$ and t-channel) are shown in left, and Kinematic variables shapes comparison between expected and CDF RunII data are shown in right. The variables are $\mathcal{M}_{\rm LLR}$ and $\mathcal{L}_{\nu \rm sol} \times \mathcal{L}_{bb \rm sol}$ from the top.

Triggered lepton W+3jets one SecVtx tag category:

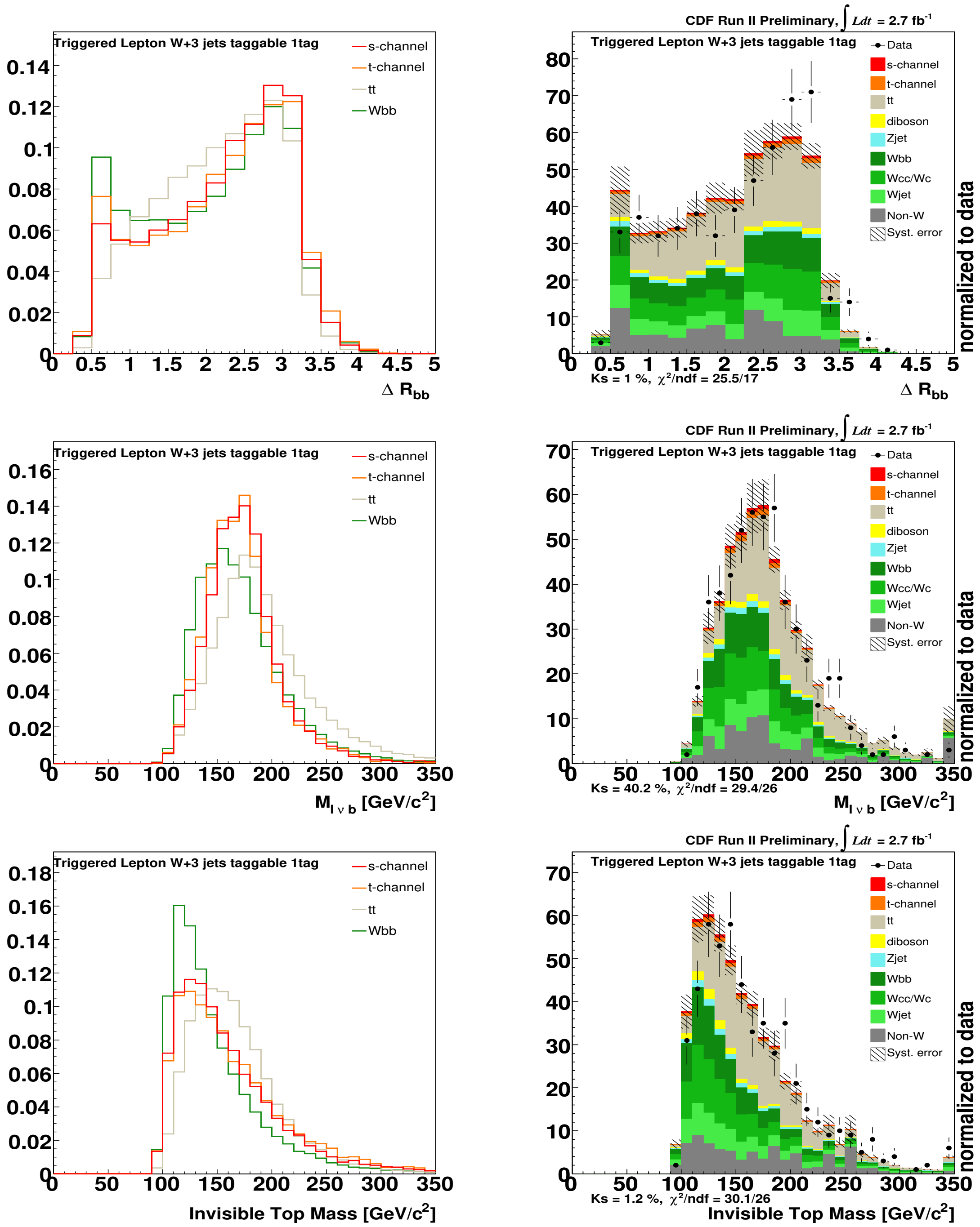

Figure A.5: Kinematic variables shapes comparison between signal and main background(Wbb, $t\bar{t}$ and t-channel) are shown in left, and Kinematic variables shapes comparison between expected and CDF RunII data are shown in right. The variables are ΔR_{bb}, $M_{l\nu b}$ and $M_{\rm invbjj}$ from the top.

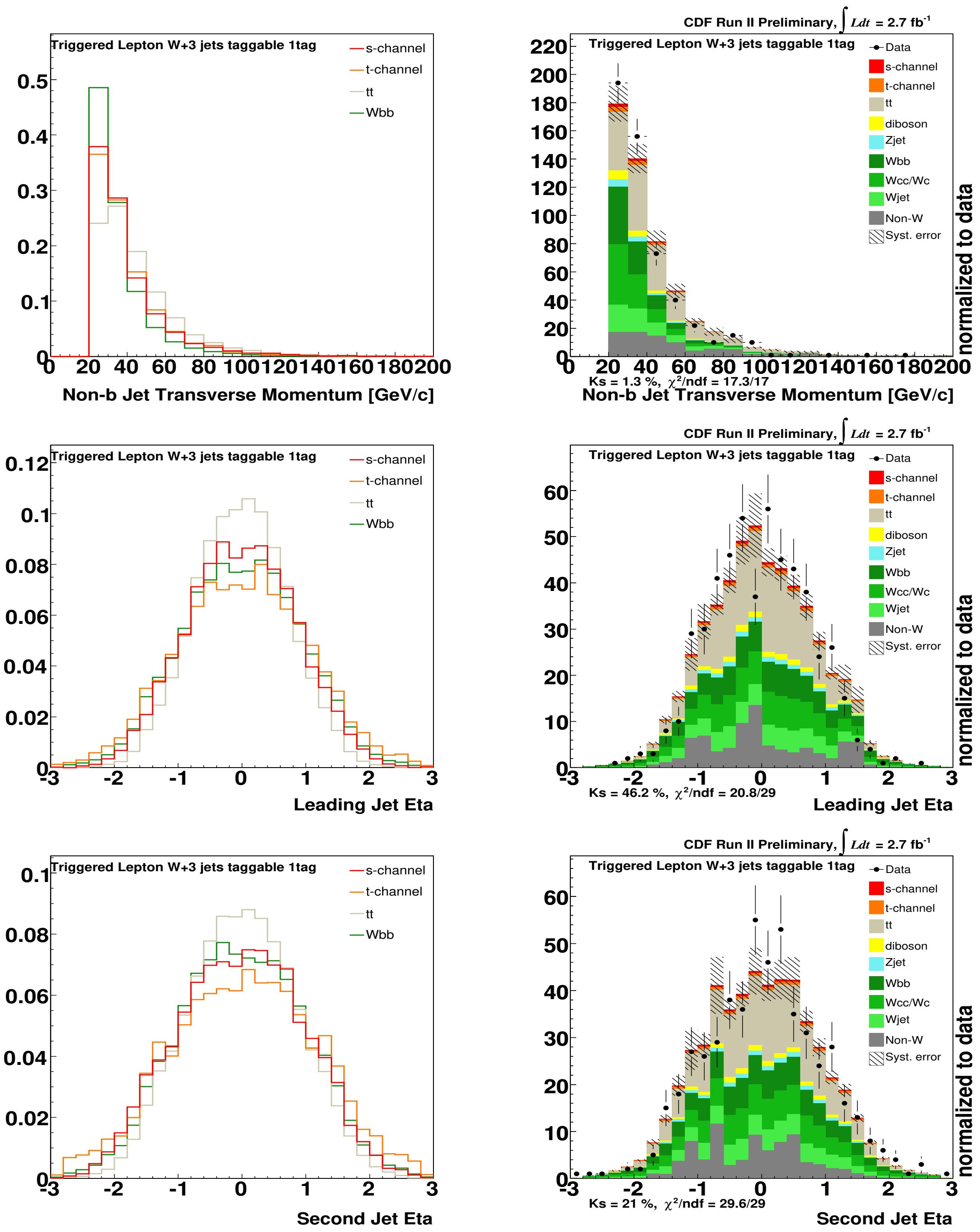

Figure A.6: Kinematic variables shapes comparison between signal and main background(Wbb, $t\bar{t}$ and t-channel) are shown in left, and Kinematic variables shapes comparison between expected and CDF RunII data are shown in right. The variables are p_T(non-b), η(j1) and η(j2) from the top.

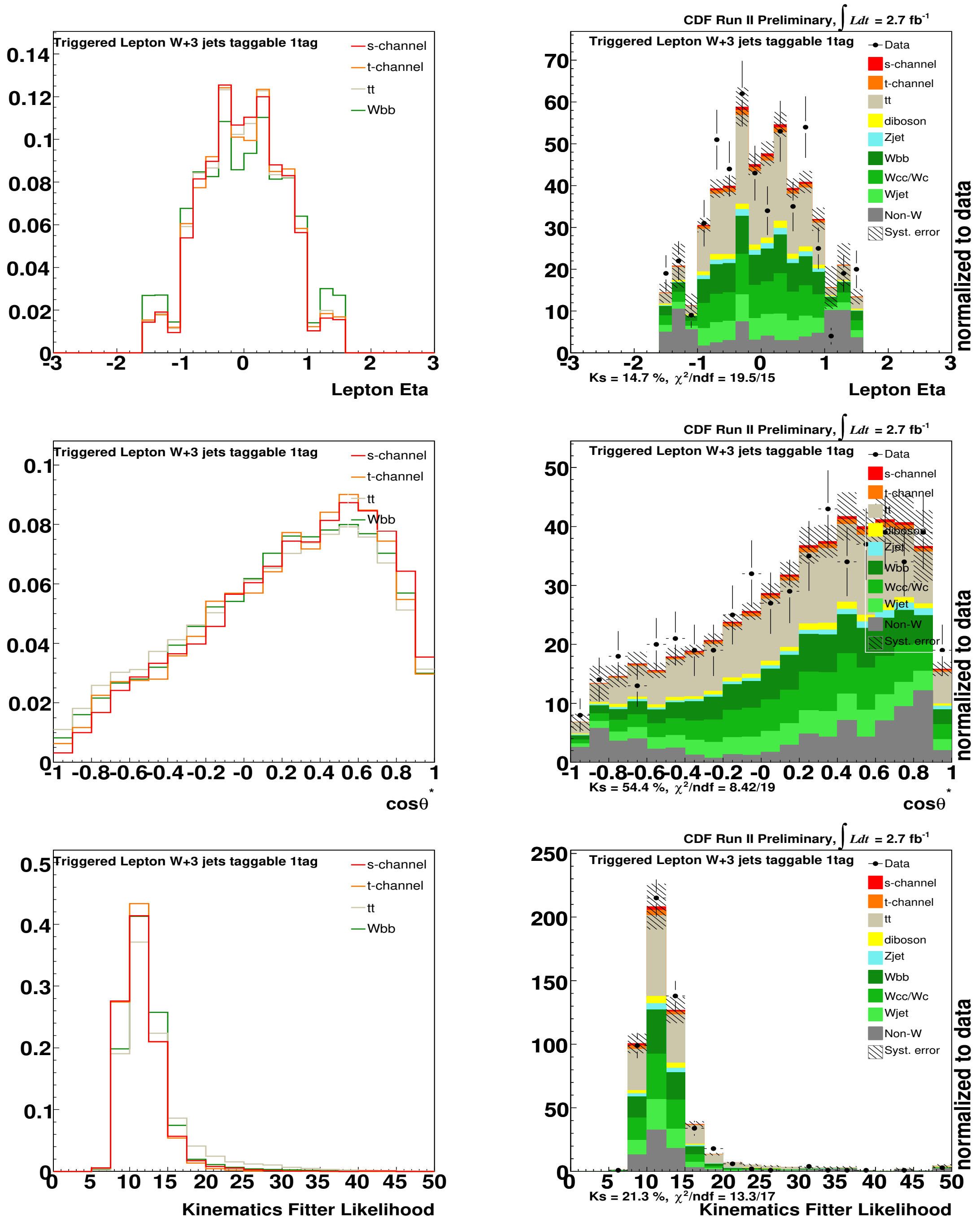

Figure A.7: Kinematic variables shapes comparison between signal and main background(Wbb, $t\bar{t}$ and t-channel) are shown in left, and Kinematic variables shapes comparison between expected and CDF RunII data are shown in right. The variables are η(lep), $\cos\theta^*$ and $\mathcal{L}_{\nu\mathrm{sol}} \times \mathcal{L}_{bb\mathrm{sol}}$ from the top.

Untriggered muon W+2jets one SecVtx tag category:

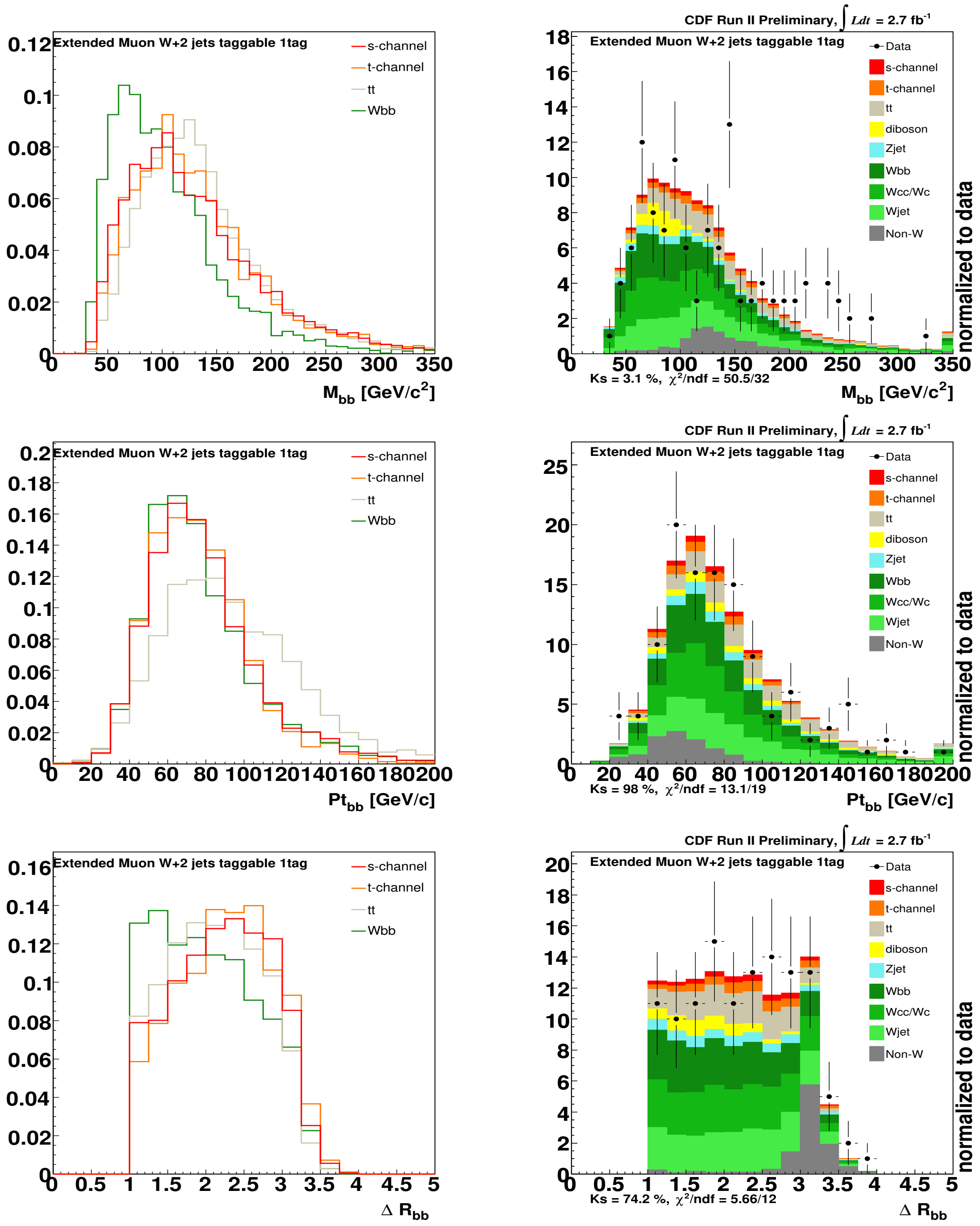

Figure A.8: Kinematic variables shapes comparison between signal and main background(Wbb, $t\bar{t}$ and t-channel) are shown in left, and Kinematic variables shapes comparison between expected and CDF RunII data are shown in right. The variables are M_{bb}, p_{Tbb} and ΔR_{bb} from the top.

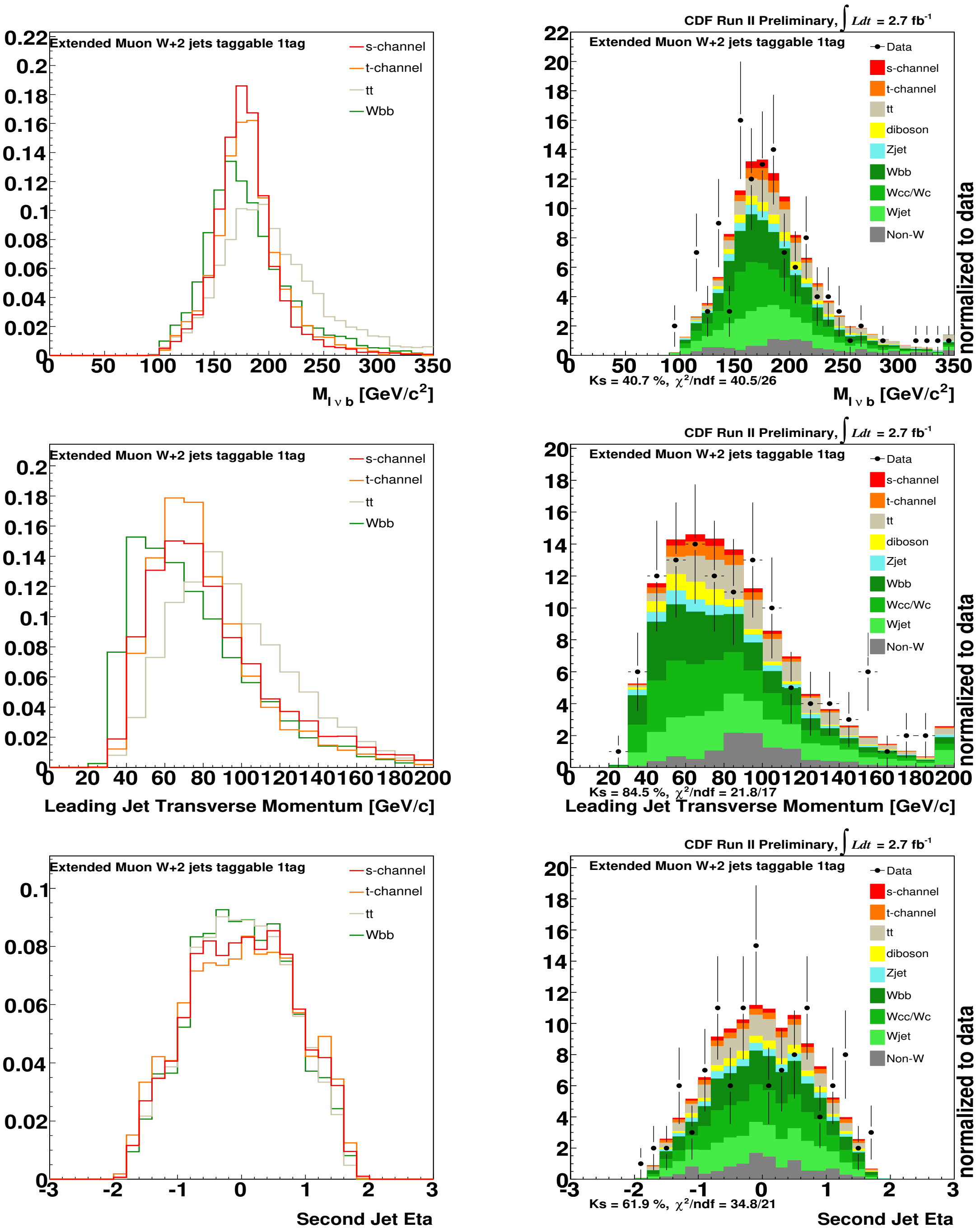

Figure A.9: Kinematic variables shapes comparison between signal and main background(Wbb, $t\bar{t}$ and t-channel) are shown in left, and Kinematic variables shapes comparison between expected and CDF RunII data are shown in right. The variables are $M_{l\nu b}$, p_T(j1) and η(j2) from the top.

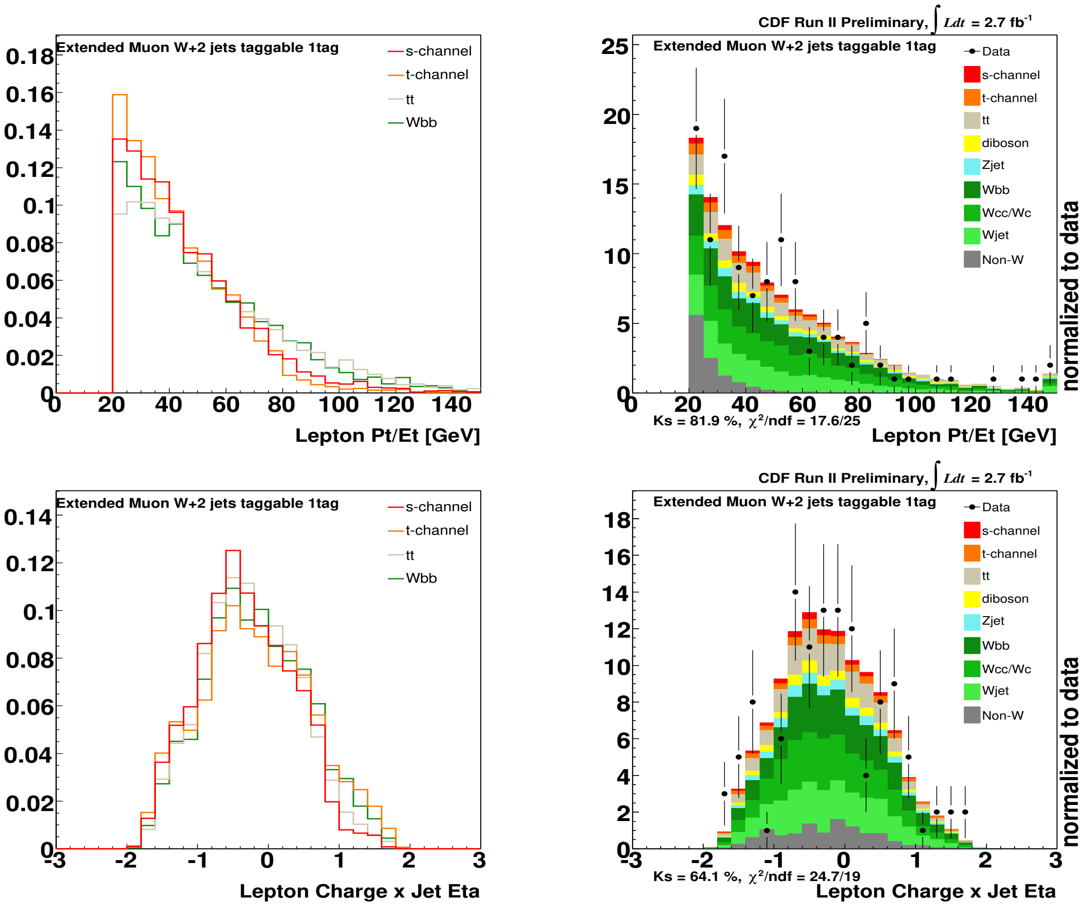

Figure A.10: Kinematic variables shapes comparison between signal and main background(Wbb, $t\bar{t}$ and t-channel) are shown in left, and Kinematic variables shapes comparison between expected and CDF RunII data are shown in right. The variables are p_T(lep) and $Q \times \eta$ from the top.

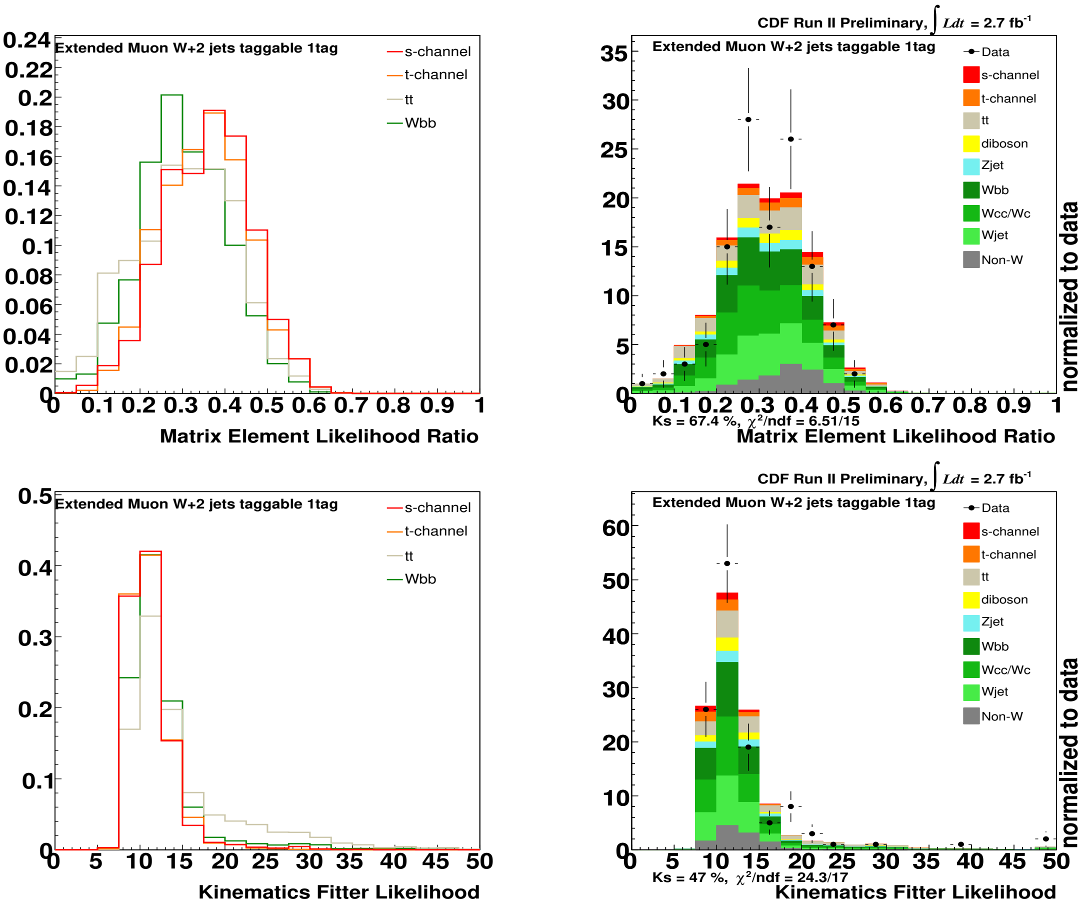

Figure A.11: Kinematic variables shapes comparison between signal and main background(Wbb, $t\bar{t}$ and t-channel) are shown in left, and Kinematic variables shapes comparison between expected and CDF RunII data are shown in right. The variables are $\mathcal{M}_{\mathrm{LLR}}$ and $\mathcal{L}_{\nu\mathrm{sol}} \times \mathcal{L}_{bb\mathrm{sol}}$ from the top.

Untriggered muon W+3jets one SecVtx tag category:

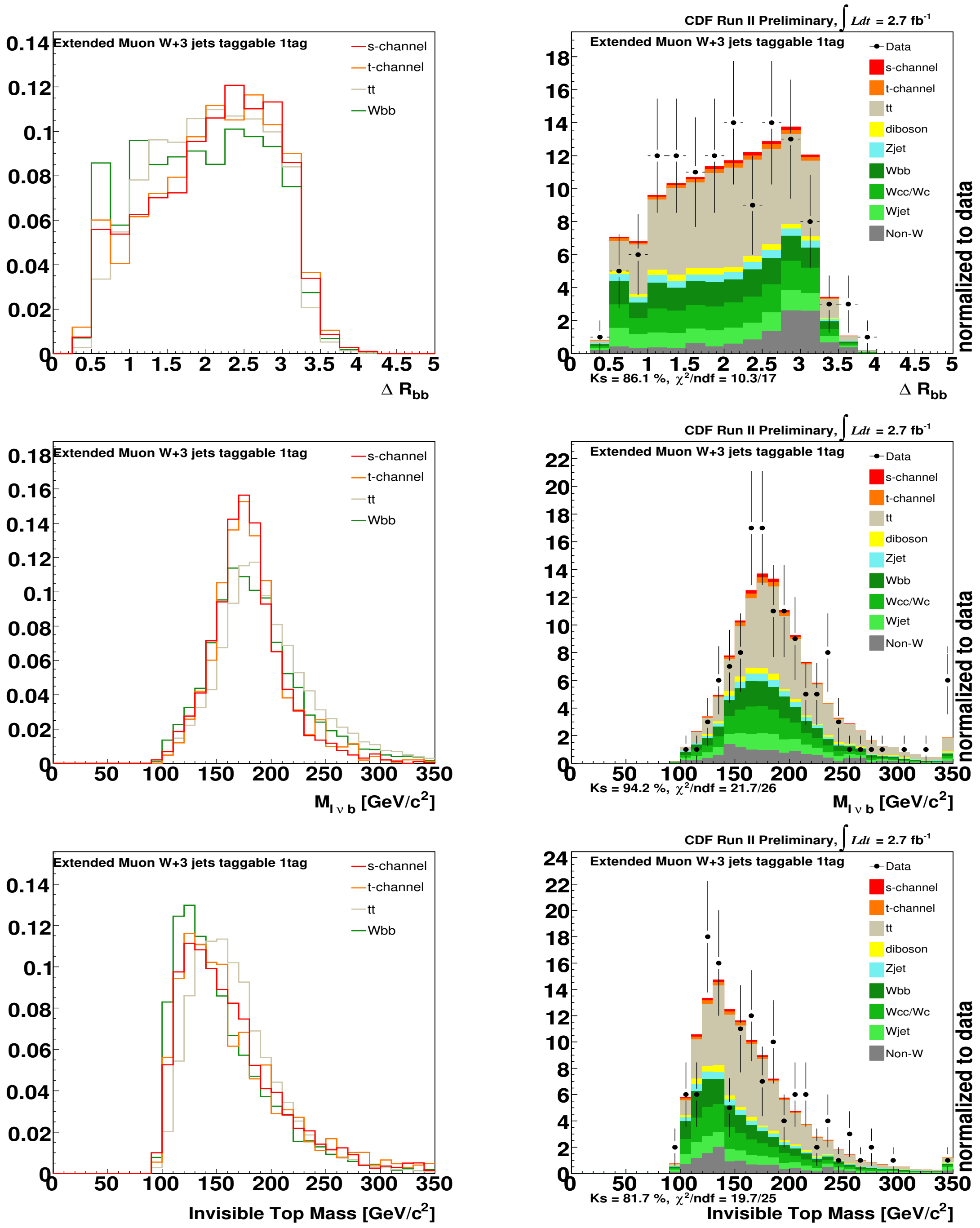

Figure A.12: Kinematic variables shapes comparison between signal and main background(Wbb, $t\bar{t}$ and t-channel) are shown in left, and Kinematic variables shapes comparison between expected and CDF RunII data are shown in right. The variables are ΔR_{bb}, $M_{l\nu b}$ and M_{invbjj} from the top.

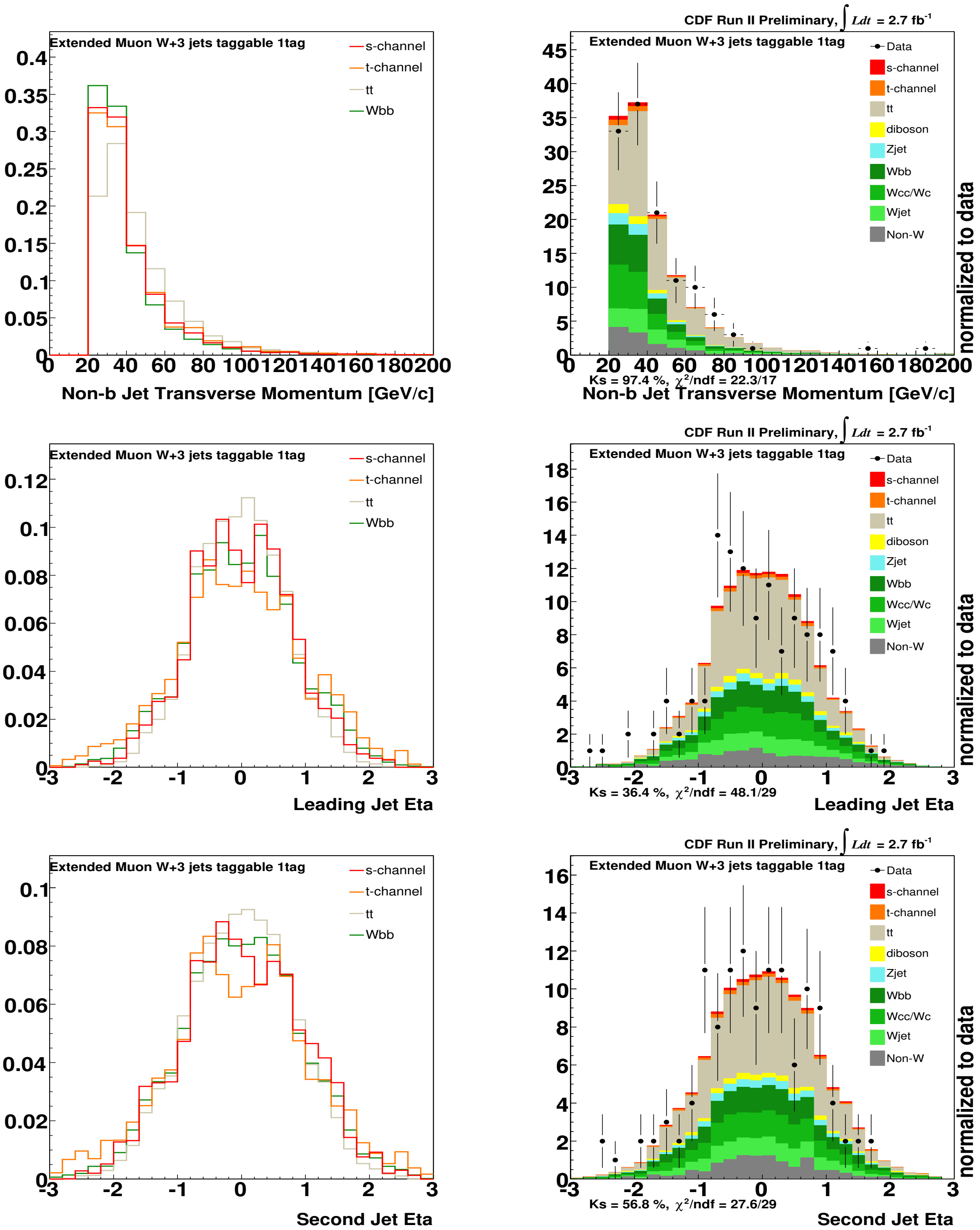

Figure A.13: Kinematic variables shapes comparison between signal and main background(Wbb, $t\bar{t}$ and t-channel) are shown in left, and Kinematic variables shapes comparison between expected and CDF RunII data are shown in right. The variables are p_T(non-b), η(j1) and η(j2) from the top.

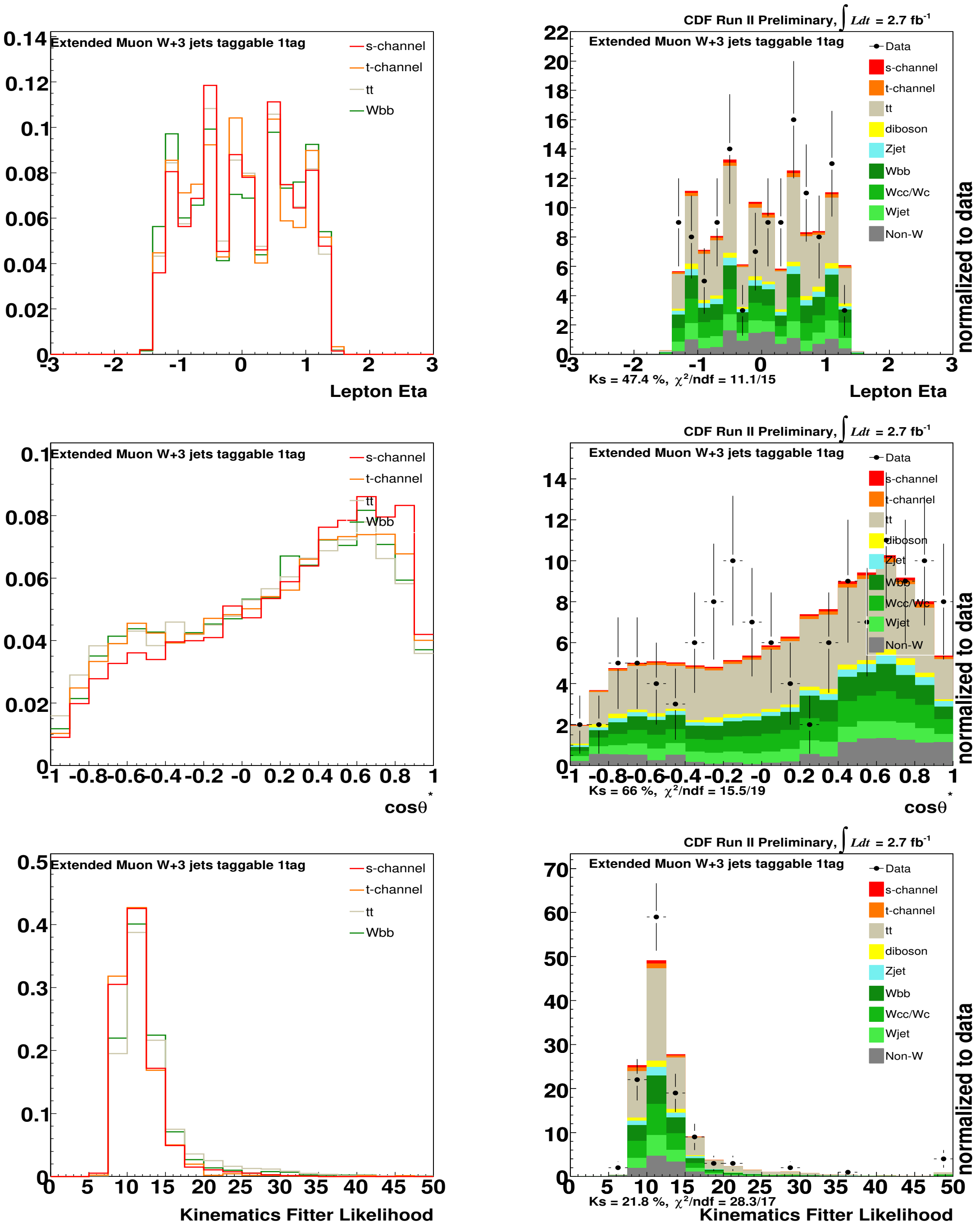

Figure A.14: Kinematic variables shapes comparison between signal and main background(Wbb, $t\bar{t}$ and t-channel) are shown in left, and Kinematic variables shapes comparison between expected and CDF RunII data are shown in right. The variables are η(lep), $\cos\theta^*$ and $\mathcal{L}_{\nu\mathrm{sol}} \times \mathcal{L}_{bb\mathrm{sol}}$ from the top.

Appendix B

Shape Systematic Uncertainties

This chapter includes the shape systematic uncertainty for the discriminant distribution of tight lepton plus double SecVtx b-tagged category. The figure B.1-B.9 show ISR, FSR, M_T, ALPGEN Q^2, JES, Non-W modeling, lepton η weight and p_{Tbb} weight systematic uncertainty, respectively.

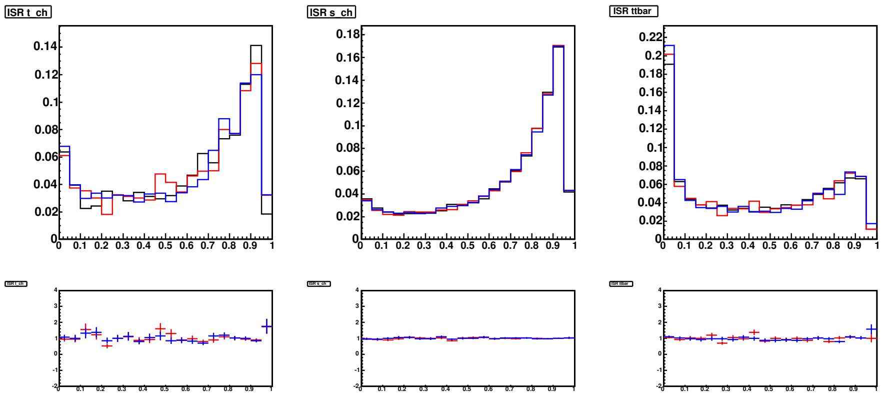

Figure B.1: ISR shape uncertainty for t-channel(left), s-channel(middle) and $t\bar{t}$(right). Black histgrams show the prediction without systematic uncertainty shift. Red and blue histograms shows distributions that amount of systematic uncertainty was shifted to plus and minus, respectively. Bottom histograms show the ratio of blue/black(blue) and red/black(red).

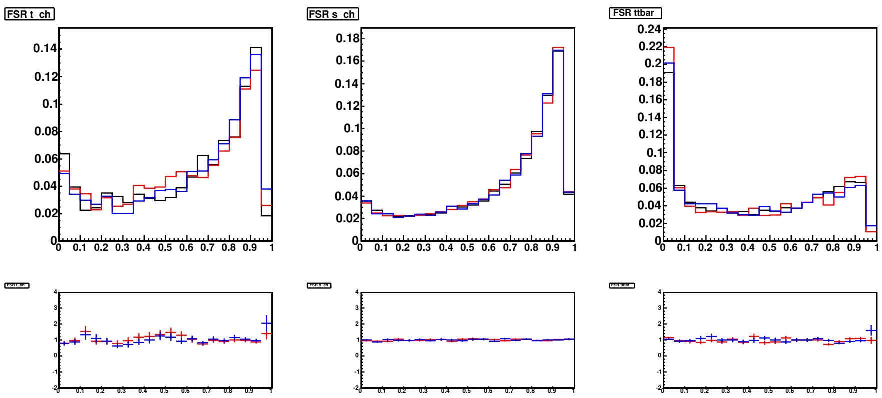

Figure B.2: FSR shape uncertainty for t-channel(left), s-channel(middle) and $t\bar{t}$(right). Black histgrams show the prediction without systematic uncertainty shift. Red and blue histograms shows distributions that amount of systematic uncertainty was shifted to plus and minus, respectively. Bottom histograms show the ratio of blue/black(blue) and red/black(red).

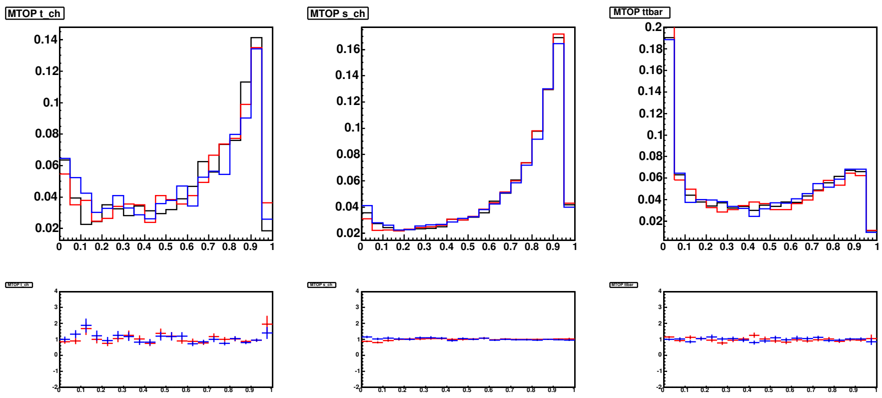

Figure B.3: M_T shape uncertainty for t-channel(left), s-channel(middle) and $t\bar{t}$(right). Black histgrams show the prediction without systematic uncertainty shift. Red and blue histograms shows distributions that amount of systematic uncertainty was shifted to plus and minus, respectively. Bottom histograms show the ratio of blue/black(blue) and red/black(red).

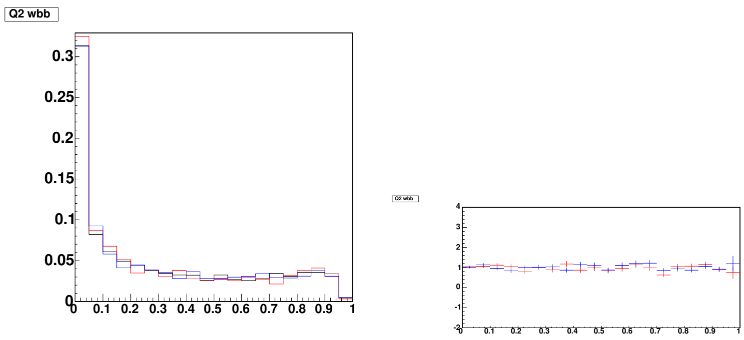

Figure B.4: $AlpgenQ^2$ shape uncertainty for Wbb sample. Black histgrams show the prediction without systematic uncertainty shift. Red and blue histograms shows distributions that amount of systematic uncertainty was shifted to plus and minus, respectively. Bottom histograms show the ratio of blue/black(blue) and red/black(red).

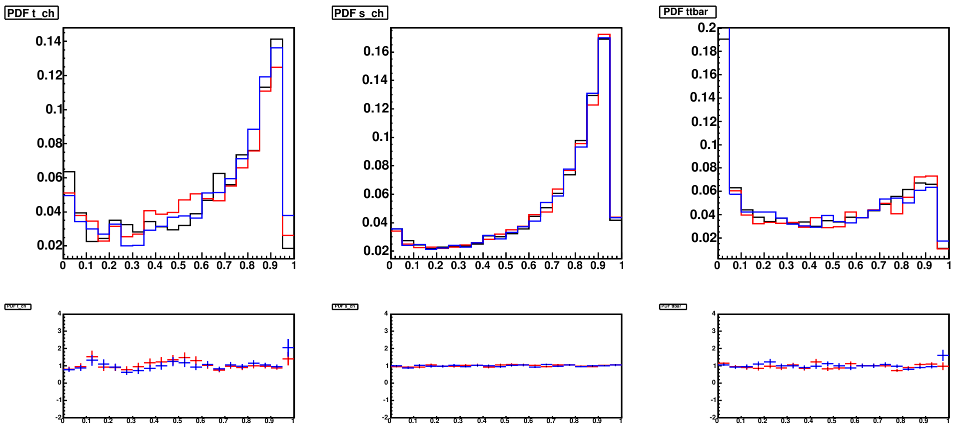

Figure B.5: PDF shape uncertainty for t-channel(left), s-channel(middle) and $t\bar{t}$(right). Black histgrams show the prediction without systematic uncertainty shift. Red and blue histograms shows distributions that amount of systematic uncertainty was shifted to plus and minus, respectively. Bottom histograms show the ratio of blue/black(blue) and red/black(red).

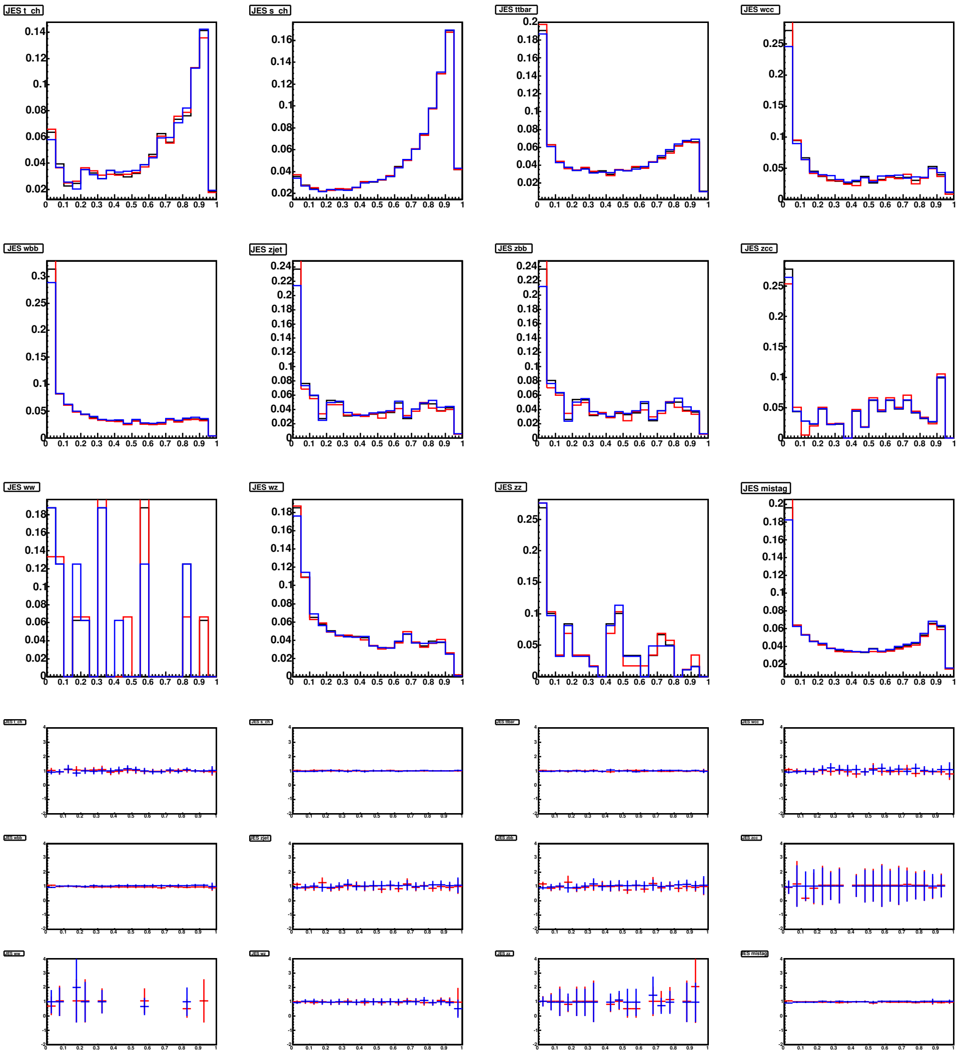

Figure B.6: JES shape uncertainty for (first line: from left to right) t-channel, s-channel, $t\bar{t}$, Wcc, (second line: from left to right) Wbb, $Zjets$, Zbb, Zcc, (third line: from left to right) WW, WZ, ZZ and $Wjets$. Black histgrams show the prediction without systematic uncertainty shift. Red and blue histograms shows distributions that amount of systematic uncertainty was shifted to plus and minus, respectively. Bottom 12 histograms show the ratio of blue/black(blue) and red/black(red).

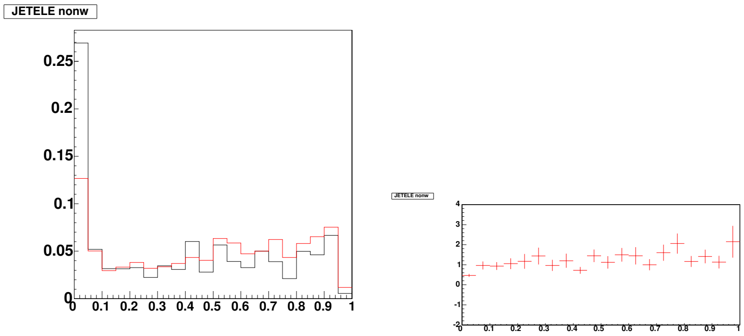

Figure B.7: left plot shows distribution of discriminat of Non-W modeling shape uncertainty. Black histgram show the prediction without systematic uncertainty shift. Red histograms shows systematic sample distributions modeled by jet-electron. Right histogram show the ratio of red/black of the left histgrams.

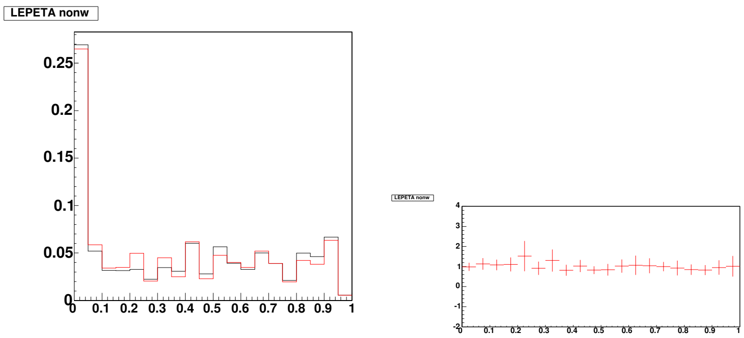

Figure B.8: left plot shows distribution of discriminat of lepton η weight uncertainty. Black histgram show the prediction without systematic uncertainty shift. Red histograms shows systematic sample distributions weighted by pre-tag ratio between prediction and data. Right histogram show the ratio of red/black of the left histgrams.

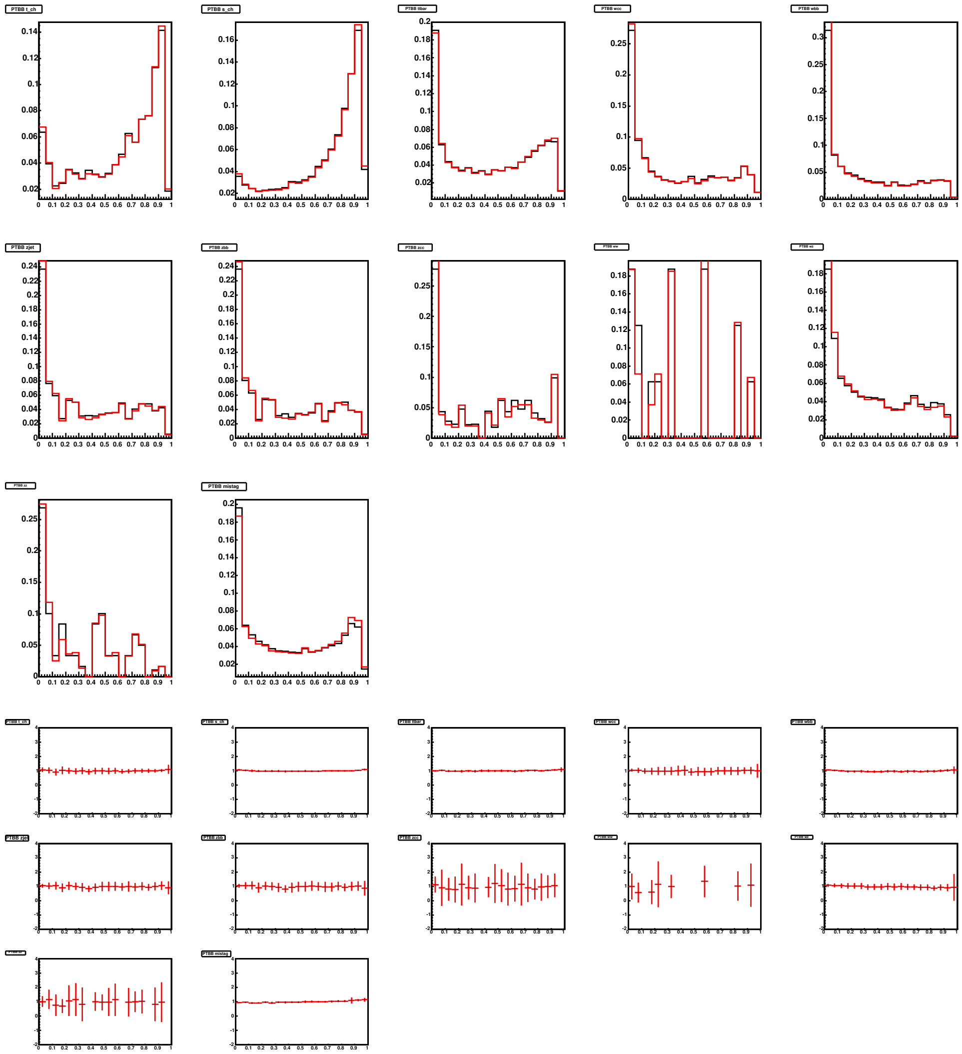

Figure B.9: p_{Tbb} weight uncertainty for (first line: from left to right) t-channel, s-channel, $t\bar{t}$, Wcc, Wbb (second line: from left to right) $Zjets$, Zbb, Zcc, WW, WZ, (third line: from left to right) ZZ and $Wjets$. Black histgram show the prediction without systematic uncertainty shift. Red histograms shows systematic sample distributions weighted by pre-tag ratio between prediction and data. Bottom 12 histograms show the ratio of red/black of the upper histgrams.

Bibliography

[1] Particle Data Group, Phys. Lett. B **667**, Issues 1-5, 18 (2008).

[2] Physics Letters B, **565**, 61 (2003).

[3] Tevatron Higgs Working Group, arXiv.org:hep-ex/0808.0534.

[4] F. Abe *et al.*, Phys. Rev. Lett. **73**, 225 (1994); F. Abe *et al.*, Phys. Rev. D **50**, 2966 (1994).

[5] F. Abe *et al.*, Phys. Rev. Lett. **74**, 2626 (1995)

[6] Tevatron Electroweak Working Group, arXiv.org:hep-ex/0808.1089.

[7] V. M. Abazov *et al.*, Phys. Rev. Lett. 100, 192003 (2008).

[8] The LEP Electroweak Working Group, *http://lepewwg.web.cern.ch/LEPEWWG/*.

[9] CTEQ Collaboration, *http://www.phys.psu.edu/∼cteq/*.

[10] H. L. Lai *et al.*, arXiv.org:hep-ph/9903282v3.

[11] G. Mahlon, Phys. Rev. D **55**, 7249 (1997).

[12] Hong-Jian He and C.-P. Yuan, Phys. Rev. Lett. **83**, 28 (1999).

[13] R. Peccei and X. Zhang, Phys. Lett. B **398**, 347 (1997).

[14] C. T. Hill, Phys. Lett. B **345**, 483 (1995);
B. A. Dobrescu and C. T. Hill, Phys. Rev. Lett. **81**, 2634 (1998).

[15] H. J. He *et al.*, Phys. Rev. D **62**, 011702 (2000).

[16] V. M. Abazov *et al.*, Phys. Rev. Lett. **98**, 181802 (2007);
V. M. Abazov *et al.*, Phys. Rev. D **78**, 012005 (2008);

[17] T. Aaltonen *et al.*, Phys. Rev. Lett. **101**, 252001 (2008).

[18] T. M. P. Tait and C.-P. Yuan, Phys. Rev. D **63**, 014018.

[19] J. Alwall *et al.*, arXiv.org:hep-ph/0607115v1.

[20] B. W. Harris *et al.*, Phys. Rev. D **66**, 054024 (2002);
Z. Sullivan, Phys. Rev. D **70**, 114012 (2004).

[21] http://www-cdf.fnal.gov/upgrades/tdr.html;
F. Abe *et al.*, Nucl. Instrum. Methods Phys. Res., Sect A **271**, 387 (1988).

[22] T. Affolder *et al.*, Nucl. Instrum. Methods Phys. Res., Sect A **526**, 249 (2004).

[23] J. Antos *et al.*, Nucl. Instrum. Methods Phys. Res., Sect A **383**, 13 (1996).

[24] H. Minemura *et al.*, Nucl. Instrum. Methods Phys. Res., Sect A **238**, 18 (1985).

[25] L. Balka *et al.*, Nucl. Instrum. Methods Phys. Res., Sect A **267**, 280 (1988);
S. Bertolucci *et al.*, Nucl. Instrum. Methods Phys. Res., Sect A **267**, 301 (1988).

[26] R. Oichi *et al.*, Nucl. Instrum. Methods Phys. Res., Sect A **453**, 227 (2000).

[27] G. Ascoli *et al.*, Nucl. Instrum. Methods Phys. Res., Sect A **268**, 41 (1988);
T. Dorigo *et al.*, Nucl. Instrum. Methods Phys. Res., Sect A **461**, 560 (2001).

[28] R. Oichi *et al.*, Nucl. Instrum. Methods Phys. Res., Sect A **461**, 540 (2001).

[29] D. Amidei *et al.*, Nucl. Instrum. Methods Phys. Res., Sect A **265**, 326 (1988).

[30] A. Abulencia *et al.*, Nucl. Instrum. Methods Phys. Res., Sect A **581**, 482 (2007).

[31] J. Adelman *et al.*, Nucl. Instrum. Methods Phys. Res., Sect A **572**, 361 (2007).

[32] M. Shimojima *et al.*, FERMILAB-CONF-07-102-E, RT2007-PSC008 (2007).

[33] W. Wagner *et al.*, PRHEP-hep **273**, (2001), FERMILAB-CONF-02-269-E.

[34] R. Brun, F. Rademakers *et al.*, Nucl. Instrum. Methods Phys. Res., Sect A **389**, 81 (1997);
R. Brun, F. Rademakers *et al.*, *http://root.cern.ch*.

[35] D. Acosta *et al.*, Phys. Rev. D **71**, 052003 (2005).

[36] S. Agostinelli *et al.*, Nucl. Instrum. Methods Phys. Res., Sect A **506**, 250 (2003).

[37] D. Buskulic *et al.*, Phys. Lett. B **313**, 535 (1993);
D. Abe *et al.*, Phys. Rev. D **53**, 1051 (1996);
A. Affolder *et al.*, Phys. Rev. D **64**, 032002 (2001), Phys. Rev. D **67**, 119901 (2003).

[38] F. Abe *et al.*, Phys. Rev. D **50**, 5550 (1994).

[39] F. Maltoni *et al.*, arXiv.org:hep-ph/0208156.

[40] B. W. Harris *et al.*, Phys. Rev. D **66**, 054024 (2002);
Zack Sullivan, Phys. Rev. D 70, 114012 (2004).

[41] T. Sjöstand *et al.*, Computer Phys. Commun. **135**, 238 (2001)

[42] F. Caravaglios *et al.*, Nucl. Phys. B **539**, 215 (1999);
M. L. Mangano *et al.*, Nucl. Phys. B **632**, 343 (2002);
M. L. Mangano *et al.*, J. High En. Phys. **0301**, 001 (2003).

[43] J. Campbell, R. Ellis, Phys. Rev. D **60**, 113006 (1999).

[44] T. Aaltonen *et al.*, Phys. Rev. Lett. **100**, 102001 (2008)

[45] H. Murayama, I. Watanabe, and K. Hagiwara, KEK Report **91**, 11 (1992).

[46] F. James and M. Roos, Comput. Phys. Commun. **10**, 343 (1975)

[47] L. Read, J.Phys G **28**, 2693 (2002);
T. Junk, Nucl. Instrum. Methods Phys. Res., Sect A **434** (1999);
P. Bock *et al.*, CERN-EP-98-046(1998) and CERN-EP-2000-055(2000).

[48] L. Demortier, Proceeding of Advanced Statistical Techniques in Particle Physics, Grey College, Durham, 18-22 March 2002

[49] R. Cousins, PhysStat05: Statistical Problems in Particle Physics, Astrophysics and Cosmology (2005).

[50] CDF Collaboration, Preliminary Result for Summer 2008 Conferences, CDF public note 9445;
CDF Collaboration, Preliminary Result for Summer 2008 Conferences, CDF public note 9451;
CDF Collaboration, Preliminary Result for Summer 2008 Conferences, CDF public note 9464;
CDF Collaboration, Preliminary Result for Summer 2008 Conferences, CDF public note 9479.